Abstract

PORTER, NATHAN WAYNE. Development of a Novel Residual Formulation of CTF and Application of Parameter Estimation Techniques. (Under the direction of Maria Avramova).

In modern science, computational modeling and simulation are often used in place of physical experiments. This is especially true in the nuclear power industry, where experiments are prohibitively expensive—or impossible—due to their extreme scales, high temperatures, high pressures, and radiation. Though the advent of the contemporary computer has enabled the design, testing, and construction of hundreds of nuclear reactors throughout the world, most simulation codes currently used in the industry were developed in the 1980's.

One such code, COolant Boiling in Rod Arrays–Three Field (COBRA-TF), was developed in the 1980's to model the thermal hydraulic response of water in nuclear reactor cores. The code used in this work, CTF, is a version of COBRA-TF which is currently developed at North Carolina State University. CTF and other "legacy codes" were designed to utilize very limited computational resources, and therefore required many simplifications. Today's computers have vastly improved memory and speed, and as such, these simplifications are no longer necessary. Though various versions of COBRA-TF have been used extensively throughout academia and industry, its original simplifications are still present in CTF.

A novel residual-based version of CTF, which enables the removal of these simplifications, is developed in this work. The code, called CTF-Residual (CTF-R), allows flexibility in the implicitness, discretization, solution algorithm, physical modeling choices, and numerical solver used to solve the fluid conservation equations. This is an improvement over the current version of CTF, which allows very little flexibility in any of these areas. In addition, CTF-R is designed with modern coding practices—software quality assurance, verification, and validation—in mind.

Currently, CTF-R is capable of modeling single phase flow with wall friction, heat transfer, lateral transfer, and nuclear fuel rods. Verification tests are used to prove that the first order numerical scheme is implemented correctly. Each model in the code is provided with a series of defect tests to ensure that it is accurate and error-free. Some models also include validation tests which compare predicted results to experimental data. Finally, regression tests are incorporated into the code repository to ensure that future changes do not break current capabilities. CTF-R includes four empirical models: wall friction, heat transfer from the nuclear fuel rods to the fluid, thermal conductivity of uranium dioxide, and thermal conductivity of zirconium. A particular correlation is chosen for each of these models, and its origin, assumptions, and an extensive set of experimental data are discussed. Each of the four correlations is calibrated to the experimental data and the resulting parameter uncertainties are included with the code distribution.

CTF-R is modern code that, with further development, will have diverse future applications.

The flexibility in the residual equations will allow a more implicit solution algorithm, which enables the use of larger time steps for a particular problem. CTF-R could be used to find a solution to the steady state conservation equations. Not only will CTF-R be capable of modeling light water reactors like CTF, but its governing equations, empirical models, and geometry could be adjusted to model next generation reactors. Given these important applications, the CTF-R framework established in this work will be an important contribution to CTF modeling.

Development of a Novel Residual Formulation of CTF and Application of Parameter Estimation Techniques

by
Nathan Wayne Porter

A dissertation submitted to the Graduate Faculty of
North Carolina State University
in partial fulfillment of the
requirements for the Degree of
Doctor of Philosophy

Nuclear Engineering

Raleigh, North Carolina

2018

APPROVED BY:

Vincent Mousseau External Member	Ralph Smith
Kostadin Ivanov	Jia (Jason) Hou

Maria Avramova
Chair of Advisory Committee

Biography

Nathan graduated *summa cumme laude* from Oregon State University in 2013 with a Bachelor of Science in nuclear engineering and a music minor. He recieved his master's degree, also in nuclear engineering, in 2015 from Pennsylvania State University with a minor in computational science. His professional work has focused on development, verification, validation, calibration, and uncertainty quantification of computational tools with emphasis on thermal hydraulic codes for nuclear applications. He currently has five published works in peer-reviewed journals.

- N. W. Porter, V. A. Mousseau, and M. N. Avramova. Quantified validation with uncertainty analysis for turbulent single phase friction models. *Nuclear Technology*, 2018. Under review.
- K. Maupin, N. W. Porter, and L. Swiler. Validation metrics for deterministic and probabilistic data. *ASME Journal of Verification, Validation and Uncertainty Quantification*, 2018. Accepted for publication.
- N. W. Porter and M. N. Avramova. Validation of CTF pressure drop and void predictions for the NUPEC BWR database. *Nuclear Engineering and Design*, 337:291–299, July 2018. `https://doi.org/10.1016/j.nucengdes.2018.07.018`.
- A. Toptan, N. W. Porter, R. Salko, and M. N. Avramova. Implementation and assessment of wall friction models for LWR core analysis. *Annals of Nuclear Engineering*, 115(2018):565–572, February 2018. `https://doi.org/10.1016/j.anucene.2018.02.022`.
- N. W. Porter, M. N. Avramova, and V. A. Mousseau. Uncertainty quantification study of CTF for the OECD/NEA Uncertainty Analysis in Modeling Benchmark. *Nuclear Science and Engineering*, 160(3):271–286, January 2018. `https://doi.org/10.1080/00295639.2018.1435135`.

Acknowledgements

I would like to express my gratitude to Professor Maria Avramova for her continuous support and guidance throughout my studies. In addition, to my mentor at Sandia National Laboratories, Vince Mousseau, for his commitment to my educational development and his willingness to share his insights with me. Also thanks to Ralph Smith and his ex-student, Katie Schmidt, for their help with Bayesian Calibration. I would also like to thank some of my fellow Graduate Students, without their collaboration I would have certainly been lost: Taylor Blyth, Alexander Bennet, and especially Aysenur Toptan. Finally, I would like to thank my friend, Arielle Schoblom, for her proofreading services for this thesis and countless other works.

This research was partially supported by the Consortium for Advanced Simulation of Light Water Reactors (www.casl.gov), an Energy Innovation Hub (www.energy.gov/hubs) for Modeling and Simulation of Nuclear Reactors under the U.S. Department of Energy. This work was also funded partially by the Graduate Fellowship in Nuclear Engineering (GFINE), which is awarded by North Carolina State University and funded by the U.S. Nuclear Regulatory Commission.

Table of Contents

List of Tables

List of Figures

List of Symbols

Greek Letters

α	Void fraction	$[\ \ ]$
$\dot{\Gamma}'''$	Inter-phase mass transfer	$[kg/m^3 \cdot s]$
δ	Film thickness	$[ft]$
ϵ	Absolute roughness	$[m]$
ε	Observational error	
η	Fraction of evaporation apportioned to the droplet field	$[\ \ ]$
$\boldsymbol{\theta}$	Parameter vector	$[\ \ ]$
μ	Dynamic viscosity	$[Pa \cdot s]$
ν	Kinematic viscosity	$[m^2/s]$
π	Posterior parameter density	$[\ \ ]$
π_o	Prior parameter density	$[\ \ ]$
ρ	Density	$[kg/m^3]$
σ	Surface tension	$[lbf/ft]$
τ	Shear stress	$[Pa]$
$\dot{\Upsilon}'''$	Inter-field mass transfer	$[kg/m^3 \cdot s]$

Nondimensional Numbers

f	Darcy Friction Factor $= 8\tau_w/\rho u^2$
Gr	Grashof $= g\beta\Delta T D^3/\nu^2$
Ja	Jakob $= \rho(h_l - h_f)/\rho_v h_{fg}$
Nu	Nusselt $= hL/k$
Pe	Peclet $= RePr = c_p \rho v L/k$
Pr	Prandtl $= C_p \mu/k$
Re	Reynolds $= \rho v L/\mu$
We	Weber $= \rho u^2 D_p/\sigma$

Roman Letters

A	Area	$[m^2]$
c_p	Specific heat	$[kJ/K]$
D	Diameter	$[m]$
G	Mass Flux	$[lbm/ft^2 \cdot s]$
h	Enthalpy	$[kJ/kg]$
h	Thermal conductance	$[W/K]$

J	Jacobian matrix	
k	Thermal conductivity	$[W/m \cdot K]$
L	Characteristic length	$[m]$
N	Number of particles or samples	$[\ ]$
P	Pressure	$[Pa]$
Q	Power	$[btu/s]$
q''	Heat flux	$[W/m^2]$
q'''	Volumetric energy generation	$[kJ/m^3 \cdot s]$
R	Thermal resistance	$[K/W]$
r	Radius	$[m]$
$\dot{s}'''$	Volumetric source term	units vary
T	Temperature	$[K]$
t	Time	$[s]$
u	Axial velocity	$[m/s]$
$\vec{u}$	Axial velocity vector	$[m/s]$
$\forall$	Volume	$[m^3]$
w	Lateral velocity	$[m/s]$
$\vec{w}$	Lateral velocity vector	$[m/s]$
x	Axial position	$[m]$

Subscripts

ann	Annular
b	Bubble
c	Cold or cladding
c	Critical
$cond$	Conduction
$conv$	Convection
ct	Constant
d	Droplet
e	Entrained droplet
f	Fuel
fg	Relative between saturated gas and saturated liquid
g	Gas or gap
hw	Hot wall
i	Spatial index, interfacial, or inside

in Inlet

l Liquid/fluid

lb Large bubble

n Non-condensible gas

nb Nucleate boiling

o Outside

out Outlet

p Particle

s Saturated or surface

sb Small bubble

scl Subcooled liquid

scv Subcooled vapor

shl Superheated liquid

shv Superheated vapor

v Gas/vapor

ve Relative between the vapor and entrained droplets

vl Relative between the vapor and liquid

w Wall

wp Wetted perimeter

Superscripts

n Time index

CHAPTER

1

INTRODUCTION

The primary responsibility of all Nuclear Power Plant (NPP) engineers, operators, and regulators is to ensure that the public is safe during both normal operating conditions and postulated accidents. In order to do this, these entities must understand the physical phenomena which govern the response of a reactor. The most obvious way to understand reactor responses is through direct experimentation, but in the nuclear industry, this can be inherently dangerous and prohibitively expensive due to the presence of high temperatures, high pressures, and radiation. Therefore, computational tools are often used to supplement experimental data.

In order to be an acceptable supplement, computational models must be accurate representations of reality. "Legacy codes," which were written in the 1970's and 1980's, were significantly impacted by the computational limitations at the time. For example, the amount of memory available was very small, therefore large matrices couldn't be stored. This restricted most codes to explicit numerical methods, since Jacobian matrices couldn't be stored in memory. As another example, early computers were very slow, which often limited the complexity or number of models that could be included in the code. Due to these types of limitations, a large number of simplifications were applied to legacy codes that were not always applicable and could introduce a significant amount of uncertainty.

Under these constraints, it was necessary to design legacy codes to be conservative. Codes were intended to overestimate the responses relevant to the safety of the reactor; if a sufficiently reliable computational tool predicted safe operation, then the reactor could be deemed safe.

This allowed the general trend of reactor behavior to be estimated with the belief that the real reactor would be safer than the simulation. Conservative methods have been used in the nuclear industry for decades, but as computers and knowledge have improved, it has become possible to estimate reactor behavior more accurately.

In 1988, the U.S. Nuclear Regulatory Commission (NRC) changed 10 CFR §50.46, which governs the licensing of new reactors, to allow licensing decisions based on Best Estimate Plus Uncertainty (BEPU) analyses [3]. Instead of calculating conservative estimates, BEPU methods attempt to accurately predict the actual response of a system with its associated uncertainties. This eliminates much of the safety margin fundamental to traditional conservative analyses, enabling efficient operation of NPPs.

In order to apply a BEPU method, it is necessary to understand, document, and quantify all sources of uncertainty in a code. The total uncertainty can be comprised of many different parts, including coding mistakes, input or output errors, numerical discretization errors, numerical convergence errors, statistical errors, model form errors, and parameter uncertainties.

Legacy codes were never intended to utilize BEPU methods, and using them presents a variety of unique challenges. The codes often lack proper documentation and it is therefore difficult to decipher the underlying physics or numerical methods. Individual empirical relations are often chosen to be conservative, and therefore must be changed for the application of BEPU methods. Moreover, the individual empirical correlations often were not designed to have inherent uncertainty information.

The motivation of this work is to transition a legacy thermal hydraulic subchannel code, Coolant Boiling in Rod Arrays–Three Field (COBRA-TF), towards more modern BEPU methods. This goal will be achieved via two separate, albeit related, tasks. The first will be to develop a novel residual formulation of the code that will provide more flexibility and be easier to use. Through the development of a new code, the numerical assumptions and inherent conservativism of the legacy version can be avoided. The second task will be to apply modern parameter estimation techniques to achieve BEPU results that are based solely on experimental data. This will supplement the existing coded models with uncertainty information which can be applied in future BEPU analyses.

The following two chapters outline background information and methods used throughout the work. Chapter 4 details the development and implementation of the novel version of The RDFMG version of COBRA-TF (CTF), including all defect tests, verification analyses, and validation. Chapter 5 details the parameter estimation process for the empirical models in CTF-Residual (CTF-R). These parameter distributions will be included with the code distribution for use in future uncertainty quantification studies. The final chapter provides concluding remarks and an outline of future work.

CHAPTER

2

THERMAL HYDRAULIC MODELING

Thermal Hydraulic (TH) codes are generally divided into three categories: subchannel analysis, system analysis, and Computational Fluid Dynamics (CFD). There is significant overlap in the methods and theory of these categories, but they are intended for specific purposes.

System analysis software is usually used to analyze an entire plant, including pumps, heat exchangers, valves, etc. Four widely used examples of system codes are Reactor Excursion and Leak Analysis Program (RELAP5-3D©) [5], Methods for Estimation of Leakages and Consequences of Releases (MELCOR) [47], The Code for Analysis of Thermal Hydraulics during an Accident of Reactor and safety Evaluation (CATHARE) [40], and The TRAC/RELAP Advanced Computational Engine (TRACE) [4]. The core models are generally very simple and are used to determine the heat source for the balance of plant. As such, it is often necessary to provide a more detailed analysis of the in-core behavior.

To address this need for higher-fidelity in-core analysis, subchannel codes can be used. These codes use arguments about the geometry and flow in a reactor core to define reactor-specific correlations, and therefore give more accurate results when used for these conditions. Subchannel models can be coupled to—or take boundary conditions from—system analysis codes to give more detailed descriptions of in-core behavior during complicated accident scenarios. For a general overview of subchannel codes, see [110]. A few notable examples are COBRA-TF [13], Versatile Internals and Component Program for Reactors (VIPRE) [29], THERMIT-2 [81], and SUBCHANFLOW [73].

CFD codes are designed to analyze meshes that are significantly finer than those in system or subchannel codes. CFD codes use turbulence models to replace much of the empirical correlations in other TH codes, and therefore present a higher-fidelity representation of reality. CFD codes can generally only accurately predict the behavior for single-phase flows, though current research focuses on two-phase CFD modeling. Typical CFD codes used in the nuclear industry are Simulating Transport in Arbitrary Regions - Computational Continuum Mechanics (STAR-CCM) [21] and ANSYS Fluent [9]. These codes are generally used to study very specific and small problems, or when computational cost is not an issue.

This work will focus on COBRA-TF, which was initially developed in the early 1980's at Pacific Northwest National Laboratory (PNNL) to model Loss of Coolant Accidents (LOCAs) [161]. Over time, the code was transferred to many different institutions and a variety of code versions exist throughout academia and industry today. One version, re-branded as CTF, is currently developed and maintained by the Reactor Dynamics and Fuel Modeling Group (RDFMG) at North Carolina State University (NCSU) [13]. CTF was incorporated into The Consortium for Advanced Simulation of LWRs (CASL), which lead to rapid improvements in the code's capabilities, parallelization, performance, validation, and quality assurance.

First, the CTF conservation equations are introduced in Section 2.1. Then in Section 2.2, the solid energy conservation equation, which is used as a simplified fuel model, will be reviewed. Section 2.3 introduces the meshing and discretization methods. Numerical approximations and solution methods are discussed in Section 2.4.

2.1 Fluid Conservation Equations

In order to solve reactor core behavior during normal operation and safety situations, it is necessary for TH codes to solve the conservation equations for fluids in the reactor. The codes generally solve the equations using a multicomponent fluid approach. Each fluid is assigned its own set of conservation equations, and transfer between the fluids is approximated using mostly empirical models. For the simulation of Light Water Reactors (LWRs), the fluids modeled in the reactor can include liquid water, steam, water droplets, and non-condensible gases.

If conservation equations for all four fluids are modeled completely, there would be a set of twenty equations to solve simultaneously: one mass, three momentum, and one energy equation for each fluid. Since this is generally not realistic, a number of approximations are used to refine the selected equations to a smaller set that still represent reality. The following list explains the particular assumptions used in CTF.

- The first assumption—which is generally a defining feature of subchannel codes—is that the primary direction of flow is upward. Flow in this direction, counter to that of gravity,

overwhelms flows in the other directions. As such, subchannel codes generally solve two momentum equations: one for "axial flow" and one for "lateral flow." Because of this assumption, they cannot accurately model reactor designs with horizontal flow, such as Canada Deuterium Uranium (CANDU) reactors. CTF is generally run with this assumption, though a full three-dimensional implementation is also available.

- The non-condensible gas and steam are in thermal and mechanical equilibrium, and therefore share a common energy and momentum equation.
- The liquid and droplet phases are in thermal equilibrium, and therefore share an energy equation. This assumption is justified by observing that the droplets are constantly entraining from and depositing to the continuous liquid field, and therefore have little time to change temperature.

With these assumptions, the full set of conservation equations is narrowed to twelve: four mass, three axial momentum, three lateral momentum, and two energy. Further assumptions are applied to the conservation equations to introduce empirical relations and to neglect terms that will be small for LWR applications.

- All phases are characterized by a single pressure.
- The vapor and non-condensible components of the gas field obey Dalton's Law, and therefore occupy the same volume.
- The viscous terms in the momentum and energy equation are neglected since inertial forces are much larger for the problems of interest.
- Empirical correlations are incorporated to account for interfacial transfer, turbulence (frictional forces and heat transfer from the wall), pressure loss coefficients, and other phenomena.
- Axial pressure drops are relatively small, and therefore the pressure gradient term in the conservation of energy equation is neglected (see Section A.1).
- The droplet field does not contact the wall, and therefore there are no frictional forces on that phase.
- The only body force is that of gravity.
- Axial flow effects are much larger than conduction in the fluid, and it is therefore neglected.
- Energy deposited directly in the fluid is assumed to be a percentage of the total energy generated in the reactor. Most of this energy deposition is from interactions of gamma rays with the fluid in the reactor, so it is called gamma heating.

These assumptions are applied to all of the following equations, and their use will be noted after each set of equations is introduced. The notation in this section is adapted from the thesis of Dr. Lloyd [91], since it is more understandable and straightforward than in the CTF Theory

Manual [13]. The liquid, vapor, entrained droplet, and non-condensible gas mass conservation equations are given in Equations 2.1-2.4, respectively.

$$\frac{\partial \alpha_l \rho_l}{\partial t} + \nabla \cdot (\alpha_l \rho_l \vec{u}_l) = -(1-\eta)\dot{\Gamma}''' - \dot{\Upsilon}''' + \dot{s}'''_{m,l} \tag{2.1}$$

$$\frac{\partial \alpha_g \rho_v}{\partial t} + \nabla \cdot (\alpha_g \rho_v \vec{u}_g) = \dot{\Gamma}''' + \dot{s}'''_{m,v} \tag{2.2}$$

$$\frac{\partial \alpha_e \rho_l}{\partial t} + \nabla \cdot (\alpha_e \rho_l \vec{u}_e) = -\eta\dot{\Gamma}''' + \dot{\Upsilon}''' + \dot{s}_{m,e} \tag{2.3}$$

$$\frac{\partial \alpha_g \rho_n}{\partial t} + \nabla \cdot (\alpha_g \rho_n \vec{u}_g) = \dot{s}'''_{m,n} \tag{2.4}$$

The liquid, vapor, entrained droplet, and non-condensible gas are indicated respectively by the subscripts l, v, e, and n. The combined vapor and non-condensible field is indicated by the subscript g. The first two terms in each mass conservation equation are the temporal and advective term in the Lagrangian derivative of mass for the given field. The mass inter-phase transfer, $\dot{\Gamma}'''$, is due to the phase change of water between liquid and vapor. It is defined positive for evaporation. The evaporation of vapor is apportioned to the droplet and liquid phases according to the factor, η, which is between zero and one ($\eta \leq 1$). The inter-field transfer, $\dot{\Upsilon}'''$, is between the continuous liquid and entrained droplet fields, which accounts for entrainment and de-entrainment of liquid drops. It is defined positive for droplet entrainment. The external source, $\dot{s}_{m,k}$, includes turbulent mixing, void drift, and lateral transfer.

Thermodynamic equilibrium between the continuous liquid and entrained droplet phases allows them to be described by a single density, ρ_l. The non-condensible gas and vapor fields share a single velocity, u_g, since the two phases are in mechanical equilibrium. The two gas components also occupy the same volume according to Dalton's law, and therefore share a single volume fraction, α_g.

The liquid and gas fields are each described by a conservation of energy equation.

$$\begin{aligned}\frac{\partial \left(\alpha_l + \alpha_e\right) \rho_l h_l}{\partial t} &+ \nabla \cdot (\alpha_l \rho_l h_l \vec{u}_l) + \nabla \cdot (\alpha_e \rho_l h_l \vec{u}_e) \\ &= -\dot{\Gamma}''' h'_l + q'''_{i,l} - q'''_{n,l} + q'''_{w,l} + (\alpha_l + \alpha_e)\frac{\partial P}{\partial t} + \dot{s}'''_{h,l}\end{aligned} \tag{2.5}$$

$$\begin{aligned}\frac{\partial \alpha_g \rho_g h_g}{\partial t} &+ \nabla \cdot (\alpha_g \rho_g h_g \vec{u}_g) \\ &= \dot{\Gamma}''' h'_v + q'''_{i,v} + q'''_{n,l} + q'''_{w,g} + \alpha_g \frac{\partial P}{\partial t} + \dot{s}'''_{h,g}\end{aligned} \tag{2.6}$$

Note that the energy conservation equation is formulated using specific enthalpy, h, rather than energy. The derivation of the enthalpy conservation equation is in Section A.1. The void fractions are related via $\alpha_l + \alpha_e + \alpha_g = 1$ and $\alpha_g = \alpha_v + \alpha_n$. The terms on the left side are the change rate and the advection of energy, respectively.

The first term on the right side is transfer due to phase change, where h'_k is the enthalpy of the fluid from which the transfer originates. The interfacial transfer rate between the k phase and the saturated interface is $q'''_{i,k}$, $q'''_{w,k}$ is the energy transfer rate between solid structures and the k phase, $q'''_{n,l}$ is the transfer rate of energy between the liquid and non-condensible gas. The pressure work done by the k phase is the term with the pressure derivative. Finally, the external energy source rate for each equation, $\dot{s}'''_{h,k}$, accounts for changes in energy due to turbulent mixing, void drift, lateral transfer, and gamma heating.

There is no viscous dissipation or internal generation in the energy equations, since these terms have been neglected. Because the liquid and droplet fields are in thermal equilibrium, they share an energy equation. The non-condensible gas and vapor share an energy equation, and have a common void fraction and velocity. A single pressure, P, is used to define the entire system. For a derivation of the enthalpy equation from the total energy conservation equation, see Section A.1).

There are also momentum equations for the continuous liquid, gas phase, and droplet field.

$$\begin{aligned}
&\frac{\partial \alpha_l \rho_l u_l}{\partial t} + \nabla \cdot (\alpha_l \rho_l u_l \vec{u}_l) \\
&\qquad = -\alpha_l \nabla P + \alpha_l \rho_l g - \tau'''_{w,l} + \tau'''_{i,gl} - (1-\eta)\dot{\Gamma}''' u' - \dot{\Upsilon}''' u' + \dot{s}'''_{v,l} \qquad (2.7) \\
&\frac{\partial \alpha_g \rho_g u_g}{\partial t} + \nabla \cdot (\alpha_g \rho_g u_g \vec{u}_g) \\
&\qquad = -\alpha_g \nabla P + \alpha_g \rho_g g - \tau'''_{w,g} - \tau'''_{i,gl} - \tau'''_{i,ge} + \dot{\Gamma}''' u' + \dot{s}'''_{v,g} \qquad (2.8) \\
&\frac{\partial \alpha_e \rho_l u_e}{\partial t} + \nabla \cdot (\alpha_e \rho_l u_e \vec{u}_e) \\
&\qquad = -\alpha_e \nabla P + \alpha_e \rho_l g + \tau'''_{i,ge} - \eta\dot{\Gamma}''' u' + \dot{\Upsilon}''' u' + \dot{s}'''_{v,e} \qquad (2.9)
\end{aligned}$$

The left side of these equations is the material derivative of the momentum, and the right side is a variety of surface, boundary, and body forces that act upon them.

The first term on the right side is the pressure force. The only body force acting on each fluid is that of gravity. The $\tau'''_{w,k}$ terms are shear forces between the k phase and any solid structures. The droplet field is assumed not to contact the wall, so $\tau'''_{w,e} = 0$. The interfacial shear force of phase k_2 on phase k_1 is τ'''_{w,k_1k_2}. The equations are formulated for the usual case where vapor is moving faster than liquid, so the interfacial force is a sink in the vapor equation and a source in the others. If this is not the case, the signs are reversed. Also note that there are no interfacial forces between the droplet and liquid field, since they are the same phase. A droplet which contacts the continuous liquid will de-entrain rather than cause interfacial friction.

The phase change term between the vapor and liquid, similar to the other equations, is $\dot{\Gamma}'''$. The velocity of the phase from which the transfer originates is u'. The entrainment models are represented by the inter-field transfer term, which is $\dot{\Upsilon}'''$. The final terms are the external

sources of momentum, which for the momentum equation represent turbulent mixing, void drift, and lateral transfer. Axial turbulent stresses are not modeled in CTF, so there is not a term which accounts for this physics.

Finally, there are three lateral momentum equations which account for transfer in the x-y plane. The lateral velocity appears in the other conservation equations in the divergence of the advection the turbulent mixing terms.

$$\begin{aligned}
&\frac{\partial \alpha_l \rho_l w_l}{\partial t} + \nabla \cdot (\alpha_l \rho_l w_l \vec{u}_l) \\
&\qquad = -\alpha_l \frac{\partial P}{\partial z} - \tau'''_{wx,l} + \tau'''_{ix,gl} - (1-\eta)\dot{\Gamma}''' w' - \dot{\Upsilon}''' w' \qquad (2.10) \\
&\frac{\partial \alpha_g \rho_g w_g}{\partial t} + \nabla \cdot (\alpha_g \rho_g w_g \vec{u}_g) \\
&\qquad = -\alpha_g \frac{\partial P}{\partial z} - \tau'''_{wx,g} - \tau'''_{ix,gl} - \tau'''_{ix,ge} + \dot{\Gamma}''' w' \qquad (2.11) \\
&\frac{\partial \alpha_e \rho_l w_g}{\partial t} + \nabla \cdot (\alpha_e \rho_l w_e \vec{u}_e) \\
&\qquad = -\alpha_e \frac{\partial P}{\partial z} + \tau'''_{ix,ge} - \eta\dot{\Gamma}''' w' + \dot{\Upsilon}''' w' \qquad (2.12)
\end{aligned}$$

All values in the lateral momentum equation have corresponding terms in the axial momentum equations. The lateral direction is defined here as z and w is the lateral velocity component. Once momentum is transferred laterally, it loses its direction. As such, transverse momentum cannot be convected from one gap to another. Such a simplification is only applicable for situations where axial flow is much larger than lateral flow.

2.2 Solid Energy Conservation Equation

CTF has a simple fuel rod model which solves the solid energy equation (or "conduction equation") for solid components with various geometries. The mass and momentum equations are excluded because thermal expansion is not considered and the solids are stationary. The energy conservation equation can be solved using a finite element or finite volume approach. It has been shown that the finite volume approach is more accurate for models with discontinuous properties [16]. Since nuclear fuel rods have very discontinuous properties due to the cladding and gap regions, a variation of the finite volume approach is used [166]. The control volume form of the conduction equation is shown in Equation 2.13.

$$\frac{d}{dt}\int_V \rho c_p T dV = \oint_A \vec{q''} \cdot d\vec{A} + \int_V q''' dV + \oint_A \vec{q''_f} d\vec{A} \qquad (2.13)$$

The first term is a change in the solid energy with time, the second is a surface integral that

accounts for energy conduction in all directions, and the third term is the volumetric generation rate in the solid. The final term accounts for transfer from the solid to the liquid, which will be zero for any control volume that is not at the surface of a solid structure. The area integrals are solved in CTF via a sum over surfaces of each cell, and the volumetric integral of the heat generation is simple since the generation is assumed to be constant for each control volume.

To avoid issues with mass conservation, the expansion or contraction of the fuel is not considered. As such, the density is always evaluated at cold state properties, ρ_c. The left side of Equation 2.13 can be simplified since the density does not vary with time and the specific heat is approximated as a linear function.

$$\int_{\not{V}} \rho_c c_p \frac{dT}{dt} d\not{V} = \oint_A \vec{q''} \cdot d\vec{A} + \int_{\not{V}} q''' d\not{V} \tag{2.14}$$

2.3 Meshing and Discretization

A staggered mesh, where velocities are defined at cell faces, is used in CTF. Staggered meshes where first applied to Eulerian codes in the 1960's [60], and since then have been widely applied in TH codes [42, 60, 127]. CTF uses staggered grids for both the axial and lateral momentum equations (see page 33 for schematic). Each of the axial scalar cells has a cross section which is defined by its flow area and wetted perimeter. These cells are traditionally either channel-centered or rod-centered, both of which are shown in Figure 2.1.

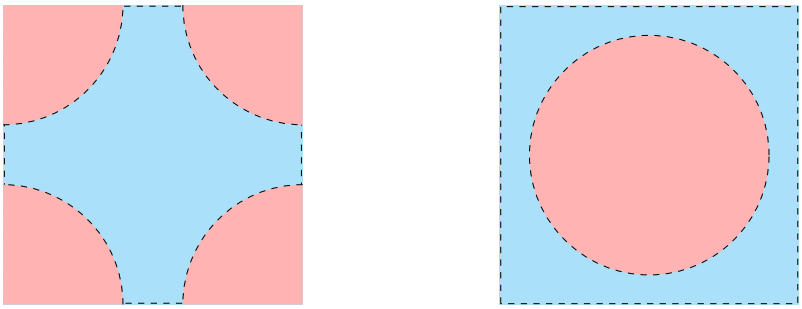

(a) Subchannel-centered (b) Rod-centered

Figure 2.1: Cross sections of traditional control volumes in CTF. Here, the red circles indicate rods and the blue sections are coolant. Subchannel codes generally use control volumes that are defined as the space between four adjacent rods (subchannel-centered), or the space around a rod (rod-centered).

The fuel rods in CTF are discretized such that control volume centers are located at the outside of the cladding, inside of the cladding, and surface of the fuel. Interpolation is therefore not necessary to calculate the temperature at these locations. The control volumes in the fuel

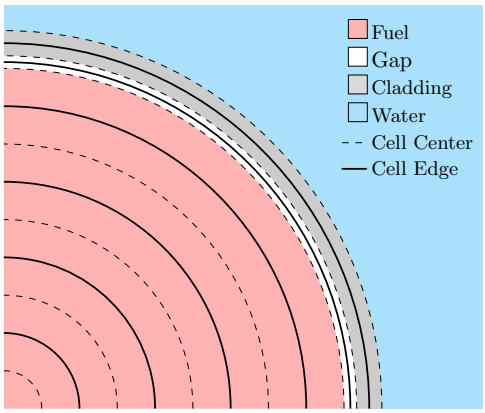

Figure 2.2: Example of CTF solid mesh. CTF uses an equally-spaced mesh inside the fuel with cell centers at the outside of the cladding, inside of the cladding, and surface of the fuel.

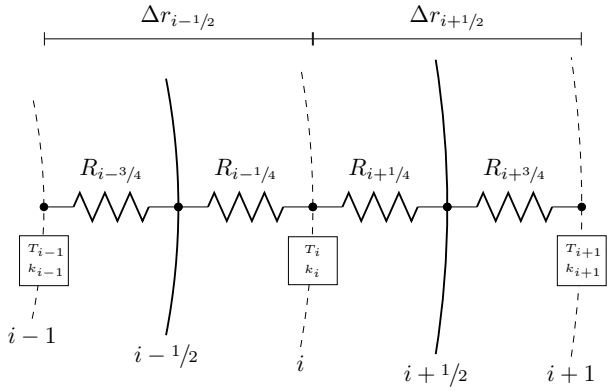

Figure 2.3: Thermal resistance analogy. The nomenclature for the four thermal resistances about cell i is established here.

region are equally spaced. It is necessary to interpolate the centerline temperature, since there is not a face at this location. Figure 2.2 is a schematic of the radial fuel meshing.

In CTF, the conduction equation is solved using a thermal resistance analogy. The resistances provide a justifiable method for averaging the thermal conductivity to face values. For example, with a Cartesian mesh, the resistance analogy is equivalent to using a harmonic average of the surrounding control volumes to calculate face thermal conductivities [127]. This method also allows simple treatment of the boundary conditions, gap region, and transfer to the coolant.

A schematic of the thermal resistances about an arbitrary cell i is shown in Figure 2.3 for cylindrical coordinates. For control volume i, the surface heat fluxes in 2.14 can be calculated.

$$q''_{i-1/2} = \frac{1}{R_{i-3/4} + R_{i-1/4}} \left(T_{i-1} - T_i\right) \tag{2.15}$$

Table 2.1: Thermal resistance equations. All thermal resistances are derived by solving the steady state conduction solution for a particular geometry. This results in relatively simple relations that are easy to implement in a code.

Region	Resistance
Fuel centerline	0
Fuel interior node	$\frac{\ln\left(\frac{r_o}{r_i}\right)}{2\pi k_f L}$
Gap	$\frac{1}{2\pi r_g h_g}$
Cladding	$\frac{\ln\left(\frac{r_o}{r_i}\right)}{2\pi k_c L}$
Rod surface	$\frac{1}{2\pi r_o h_g}$
Axial and azimuthal transfer	$\frac{L}{kA}$

$$q''_{i+1/2} = \frac{1}{R_{i+3/4} + R_{i+1/4}} \left(T_{i+1} - T_i\right) \tag{2.16}$$

Here, the resistances and temperatures refer to those in Figure 2.3. The resistances of the corresponding regions are calculated according to a steady state conduction solution for the given fuel cell. Boundary conditions and gap transfer are included as resistances. The equations to calculate each of the thermal resistances are listed in Table 2.1 [161, 162, 166]. The thermal resistances are updated explicitly.

Axial and azimuthal transfer are added as explicit terms in CTF. The axial mesh in the solid region is the same as the fluid region, so each surface solid cell transfers its energy directly to a single fluid cell.

2.4 Numerical Methods

The conservation equations for mass, momentum, and energy can be arranged and solved in a variety of ways. In the most general sense, the discretized form of the equations are arranged in a matrix and solved for the unknown vector of variable updates, δx.

$$J\delta x = -F(x) \tag{2.17}$$

Here, J is the Jacobian matrix and $f(x)$ is the residual vector. Each row in the Jacobian is related to a specific conservation equation and each column is one of the unknown variables. Most numerical methods are iterative, and convergence is reached when the change between iterations is sufficiently small. In CTF, the full Jacobian matrix is row-reduced to solve for the pressures in each fluid cell.

$$J'\delta P = b \tag{2.18}$$

Here, J' is the pressure matrix, δP are the pressure updates, and b is the row-reduced right hand side. In this way, all fluid conservation equations are incorporated into a single $n \times n$ matrix, where n is the number of computational cells. See [12, Section 3.1] for a description of the pressure matrix construction and solution algorithm.

The fluid conservation equations do not have a general closed-form solution, so it is necessary to find a numerical approximation. The simplifications necessary to find this solution are discussed next.

The first approximation deals with the discretization of the conservation equations in space. Since the continuous form of the equation cannot be solved numerically, one must make an assumption about how the value of all quantities vary throughout a control volume. In CTF, all quantities are assumed to be a constant average value for a specified control volume:

$$\bar{\psi} = \frac{1}{V} \int_V \psi dV, \tag{2.19}$$

where ψ is any continuous variable and $\bar{\psi}$ is the average value over the cell. This assumption is generally accurate, but can cause numerical errors for situations with sharp gradients or discontinuities. Variables will be defined by the mesh for which their conservation equations are defined. For example, density and enthalpy are defined on the "continuity" or "scalar" mesh and velocity is defined on the "momentum" or "vector" mesh. For example, if the indexing of the staggered mesh in Figure 4.1a is used, scalar quantities are assumed to be constant averaged quantities between $i - 1/2$ and $i + 1/2$ with a center at i. Momentum quantities are constant between cell centers. For situations when quantities are shared between the conservation equations, a relationship between the two meshes must be used. In CTF, a linear average is generally used to transition quantities between the two meshes.

Advection terms in the conservation equations are discretized on the spatial mesh using a first-order upwinded difference. This is necessary for convergence, and introduces the Courant-Friedrichs-Lewy condition (CFL) to ensure numerical stability when explicit time integration is used [28]. Other spatial terms are discretized using second-order central differences.

Once the spatial discretization is addressed, the set of equations is spatially discrete and temporally continuous. The discretization in CTF is a one-step difference scheme where the time

variables are evaluated at discrete points between the beginning and end of the simulation. The simplest method to solve these equations is a purely explicit method, where the conservation equations for each control volume are formulated such that a single unknown variable can be directly calculated using each of them. The explicit method is detailed in Algorithm 2.1.

Algorithm 2.1: Fully explicit solution algorithm. Also called a single stage or linearized method, an explicit solution algorithm reduces the cost of the matrix solve but generally requires smaller time steps.

Input : initial conditions $x^o = x(t^o)$, time step Δt, and number of steps N

for $n = 1$ **to** N **do**
  $t^{n+1} = t^n + \Delta t$
  $\delta x = -J(x^n)^{-1} F(x^n)$
  $x^{n+1} = x^n + \delta x$
end

In the explicit algorithm, all discretized conservation equations contain only one value evaluated at the new time, and therefore each one can be solved individually—there are no cross terms in the Jacobian matrix. Though the explicit method is a relatively computationally inexpensive solution algorithm, it is only numerically stable when specific stability criterion are met. Therefore, the explicit method often requires the use of very small time steps.

A fully implicit method evaluates all state variables in each conservation equation at the new time step. The Jacobian is no longer a diagonal matrix, which is more difficult to solve. Though each individual time step may take longer to solve, fully implicit methods are unconditionally stable and therefore very large time steps can be taken. Since the implicit fluid equations are highly nonlinear, Newton's method is often used [80]. This method, which is fully implicit with a nonlinear iteration, is outlined in Algorithm 2.2.

Other methods exist that use some combination of implicit and explicit variables to solve the set of discretized equations [80]. These methods, generally called semi-implicit methods, include the following:

- Pressure projection methods, such as the one used by CTF and its predecessors, which is a predictor-corrector scheme between pressure and velocity [13, 127];
- The Stability-Enhancing Two-Step Method (SETS), which is a multi-stage approach used in TRACE [4, 96];
- The nearly-implicit method, which is similar to SETS and used by RELAP5-3D© [5, 165]; and
- Many other semi-implicit methods [90].

Algorithm 2.2: Fully implicit solution algorithm. Also called a multi-state or nonlinear method, an implicit solution algorithm can take large time steps but the matrix solve is more costly.

Input : initial conditions $x^o = x(t^o)$, time step Δt, and number of steps N

for $n = 1$ **to** N **do**
  $t^{n+1} = t^n + \Delta t$
  $x^k = x^n$
  for $k = 0$ **to** K **do**
    $\delta x^k = -J(x^k)^{-1} F(x^k, x^n)$
    $x^{n+1} = x^k + \delta x^k$
  end
  $x^{n+1} = x^{k+1}$
end

CTF is restricted to using a pressure projection method, since the terms in the algorithm are derived by hand and hard-coded in the solution algorithm. The next chapter will introduce a novel residual-based version of CTF which is not restrained to a particular choice of solution algorithm.

2.5 Possible Improvements

Though CTF is a well-established code which has been applied extensively throughout the literature for the last few decades, some aspects of the code are detrimental to future modeling.

1. Many models in the code were implemented long ago. Most of these were originally well-documented, but not all code developers have followed the same process. As such, many of the models lack proper documentation and the individuals who implemented them are now retired. As an example, see the interfacial mass transfer model in Appendix B. This model was only minimally documented before the appendix was assembled, and the origin of some of the correlations is still unknown. Additionally, some correlation implementations are not consistent with their corresponding models in the literature. Usually, no motivation or justification is given for these changes. With undocumented or adjusted models, it is difficult to perform any assessment of code accuracy.
2. The pressure matrix in CTF was calculated by hand and then hard-coded in the software. This was a requirement when computers had limited memory and speed, since only a few solution algorithms could possibly be implemented. In contrast, codes today have greatly expanded memory, speed, and code structures that no longer require these simplifications. As such, a code can be highly flexible and allow for different discretizations, implicitness,

etc.

3. The equations and closure models in CTF are implemented specifically for LWRs. Assumptions are made throughout the code which depend upon this fact. For example, the effects of natural circulation are mostly ignored, conduction in the fluid is neglected, and the boiling model is specifically for water. It would be necessary to change many of these modeling choices to apply CTF to most other reactor types. This includes any reactor which relies on natural circulation in the event of off-site power, liquid sodium reactors, liquid metal reactors, or even high temperature gas reactors. As such, the development of a tool which can easily be changed would be beneficial for these important future applications.
4. Finally, the software development tools described in the next chapter were not formalized at the time CTF was written. Though the code developers likely used detailed and thorough tests for their code, these tests were rarely documented and never added as regression tests. Since CTF has been implemented in The Consortium for Advanced Simulation of Light Water Reactors (CASL), the verification and validation of the code has been drastically improved. Nonetheless, it is very difficult, if not impossible, to provide a pedigree for a code which was not designed with these ideas in mind.

The new version of CTF, outlined in Chapter 4, addresses all of these issues in some way.

CHAPTER

3

VERIFICATION, VALIDATION, AND UNCERTAINTY QUANTIFICATION

An important part of code development is establishing that the results can be trusted. This can take a variety of forms: testing the numerical methods, benchmarking against other codes, Software Quality Assurance (SQA) programs, comparison to experimental data, or bounding the output with uncertainty. This section will briefly discuss all of these activities.

A variety of authors have developed quantitative methods to address all sources of uncertainty in computational tools. One such method is the Code Scaling, Applicability, and Uncertainty (CSAU) method, which was developed by the NRC to support BEPU analyses [78]. Another example is the Predictive Capability Maturity Model (PCMM), which groups evidence that a code is mature into the following six categories: code bugs, code verification, solution verification, validation, parameter uncertainty, and calibration [121].

Much of the processes in formal Verification, Validation, and Uncertainty Quantification (VVUQ) methods are similar, and the relevant steps are outlined in a number of references [78, 121, 122, 167]. Some of the literature disagrees on terminology for these activities, so this chapter will outline each briefly as used in this work. The process necessary to establish code credibility is outlined in Figure 3.1.

First, SQA is used to minimize general code bugs; it is outlined in Section 3.1. Section 3.2 deals with code verification, which minimizes bugs in the numerical solution algorithm. The

Figure 3.1: General process for establishing code credibility. Each of the five steps minimizes different sources of uncertainty and is described at length in this chapter.

numerical uncertainty in a code is quantified using solution verification, which is described in Section 3.3. Validation is the process of ensuring that the code is a faithful representation of reality and it is detailed in Section 3.4. Some quantitative metrics used in verification and validation problems are defined in Section 3.5. Section 3.6 describes the process of assessing code output uncertainty. Finally, a process related to uncertainty quantification, parameter estimation, is described in Section 3.7. Finally, identifiability and sensitivity are processes important to Uncertainty Quantification (UQ) and parameter estimation. They are outlined in Sections 3.8 and 3.9.

3.1 Software Quality Assurance

SQA is accomplished by employing appropriate software engineering practices to minimize the number of mistakes in the code. A variety of activities fall under this category [122].

First, defect tests ensure that small portions of the code are working correctly. There are three types of defect tests which verify different parts of the code: unit, component, and system. *Unit tests* are very simple test problems which verify a particular function or subroutine. *Component testing* consists of testing isolated parts of the code, such as a call to a module that has an expected result. *System tests* show that the components are coupled correctly. All of these SQA activities can be incorporated as *regression tests*, which are used to ensure that a code does not lose capabilities as it is developed. Regression test suites are run periodically and should include at least one test problem for every feature, combination of features, input and outpute options, and solution algorithms in the code.

If there is a code with similar capabilities to the one being developed, it can be used as a benchmark. When using another code this way, it is important to have confidence in that code's results. If confidence is lacking, then differences between the codes should be analyzed with skepticism and changes should not be made to either code to bring the results into agreement.

3.2 Code Verification

Code verification ensures that a computer code is a faithful representation of the original mathematical model. This is accomplished via order of convergence assessment. The convergence

rate of all numerical methods can be assessed using Modified Equation Analysis (MEA), which is based on Taylor Series approximations of discretized equations [65]. Therefore, it is possible to design test problems with analytical solutions that, when their spatial or temporal mesh is refined, demonstrate the proper convergence rate. The analytical convergence rate is referred to as the *formal order of accuracy*, and the convergence rate of the code is the *observed order of accuracy*. If the formal and observed orders agree, then the analyst can be reasonably confident that the code is an accurate representation of the intended mathematical model.

Code order convergence problems must have an analytical solution, which can be very restrictive. Nonetheless, since the order is a purely mathematical result, there is no requirement that the test problem represent a physical situation. As such, a variety of methods can be used to find problems for which analytical solutions exist. The first, and most obvious, is to design an extremely simple problem which can be analytically solved by hand. These problems generally work well, and they should be included as verification problems. Tests with approximate solutions can also be used, but they must be highly accurate in order to converge as expected.

The Method of Manufactured Solutions (MMS) uses a given solution to calculate source terms for the conservation equations [147]. The source terms are then added directly to the discretized equations, and the code results should match with the original solution. MMS is a very thorough analysis method because the source terms can involve both time and space, as well as different continuous distributions for the state variables. In addition, MMS procedures can be automated using symbolic computation, which eliminates most human error from the process. An MMS problem that converges with the expected order of accuracy is one of the best indications that the mathematical representation of the code is accurate. A method similar to MMS which uses physically realistic test problems is the Method of Nearby Problems (MNP) [144].

3.3 Solution Verification

The main focus of solution verification is the estimation of numerical errors that occur when a mathematical model is discretized and solved on a digital computer. In solution verification, the exact solution to the mathematical model is not usually known, and thus numerical error must be estimated and not simply evaluated.

Solution verification can be concerned with approximating the error originating from a variety of sources. *Round off errors* are due to the limited precision available on computers. This is generally very small and negligible for double-precision programs. *Statistical uncertainty* can dominate for codes that are stochastic in nature. *Iterative error* is due to solution of the coupled system of equations and can be assessed by changing the convergence criterion and quantifying the resulting change. In general, this error is negligible *if* the convergence criterion are properly set and the iterative procedure is not divergent.

The largest source of error is from discretizing the governing equations. This contribution is assessed by comparing the code order of convergence to the formal order. This is similar to convergence assessment in code verification, but an analytical solution is generally not available. Instead, the convergence between successive refinements of the spatial or temporal mesh is used to approximate the error. When performing solution verification, the order of accuracy requirements are generally looser than for code verification.

3.4 Validation

Validation is the process of assessing if code models are an accurate representation of reality. This is done through comparison to experimental data. If the code accurately predicts the experimental results, then it is validated.

Validation can be split into two general categories: separate effects and integral effects. *Separate effects* tests are experiments that were designed to use a single model or correlation. For example, an isothermal pipe flow experiment could be considered a separate effects friction test. For an example of separate effects validation, see Section 4.4.3 and [163]. *Integral effects* tests incorporate the use of many models or systems of the code. Examples of integral effects experiments are the BWR Full-size Fine-mesh Bundle Test (BFBT) [117] and the PWR Subchannel and Bundle Test (PSBT) [145] Benchmarks. An example of integral effects validation can be found in [133]. Integral effects validation is important to the validation process, but compensating errors can produce unreasonably good results, especially if any amount of calibration has been performed. To avoid these compensating errors, separate and integral tests should be used together during code validation.

Some experiments are not suitable to use as validation data. Oberkampf [122] cites three types of traditional experiments which fit into this category: (1) discovery experiments to improve the fundamental understanding of some physical process, (2) model development experiments to improve fairly well-understood physical models, and (3) reliability tests which that test new engineering systems. A *validation experiment*, on the other hand, is conducted primarily to test a simulation code. This requires that all relevant characteristics of the experiment, both within the system and outside it, are accurately measured.

Validation can also be used to assess the model form uncertainty inherent in a code. In order to represent reality, engineers narrow down real physics to create a model. These models are generally good representations, but there is inherent uncertainty in them. If all numerical error has been minimized via verification, then the remaining error can be apportioned to model form and parameter uncertainties. The model form error can also be reduced by quantitatively choosing the best model for particular problems (see [101, 139] for examples).

3.5 Quantitative Metrics

For both verification and validation problems, the results are often summarized quantitatively using a single value. These studies usually require the comparison of two arrays and the distance between them can be quantified in many different ways [102]. This section outlines all metrics used in this work.

Minkowski Distance For verification problems, the change in the quantity of interest between two successive iterations is calculated using the Minkowski Distance. This metric, also called a vector norm, is very commonly used to assess the difference between two vectors.

$$||x||_n = \left[\sum_i (x_i)^n\right]^{1/n} \tag{3.1}$$

Here, x is usually defined as the difference in the quantity of interest between the fine mesh and the coarse mesh. So, if enthalpy is the quantity of interest, $x = h_{fine} - h_{coarse}$. In this work, three norms are used.

$$||x||_1 = \sum_i |x_i| \tag{3.2}$$

$$||x||_2 = \sqrt{\sum_i (x_i)^2} \tag{3.3}$$

$$||x||_\infty = \max |x_i| \tag{3.4}$$

These are respectively the L_1, L_2, and L_∞ norms. The L_2 norm is also known as the Euclidean norm and is likely the most commonly used. By definition, $L_1 \geq L_2 \geq L_\infty$, though they all result in similar orders of accuracy when applied to verification problems.

Root Mean Square Error One of the most common validation metrics is the root-mean-square (RMS). This metric is the square root of the summed errors divided by the number of errors.

$$\text{RMS} = \sqrt{\frac{1}{n}\sum_{i=1}^{n} x^2} \tag{3.5}$$

In general, the error x is defined as $x = x_m - x_p$ where x_m is the experimentally measured quantity and x_p is the quantity predicted by the code. In this work, the relative errors, $x = \left|\frac{x_m - x_p}{x_m}\right|$, are used because the quantity of interest can vary over many orders of magnitude. When using the relative errors, the RMS becomes the relative RMS (rRMS).

A similar metric, the mean square error is also used.

$$\text{mse} = \frac{1}{n}\sum_{i=1}^{n}\left(\frac{x_m - x_p}{x_m}\right)^2 \tag{3.6}$$

3.6 Uncertainty Quantification

Uncertainty Quantification is the science of analyzing uncertainty in order to make predictions and understand the degree to which predictions can be trusted. An uncertainty analysis is essentially meaningless until a thorough verification study has been completed. UQ and validation are often performed simultaneously, since analysts are often interested in calculating uncertainty of their validation results. Sensitivity studies and parameter estimation should be performed before UQ studies to select the sensitive input parameters and give them bounds.

Errors can have various forms that must be treated differently. First, *aleatory* uncertainties are those that are inherent to a process and cannot be reduced with additional information. Examples include boundary conditions and parameter uncertainties. Aleatory uncertainties are generally unbiased and easily defined in a probabilistic framework. The second type of uncertainty, *epistemic*, is more difficult to treat probabilistically. Epistemic uncertainty is due to lack of knowledge, and is often associated with simplifying assumptions or physics that are not accounted for. These errors are generally referred to as model errors if numerical uncertainty has been minimized. During the UQ process, epistemic uncertainties are often recase as aleatory in order to treat all sources of uncertainty in the same way.

Uncertainty analysis is the process of propagating input parameter distributions through a computational tool, and calculating bounds on the resulting quantities of interest. This process can either be deterministic or statistical.

Deterministic methods use derivatives of the parameters of interest with respect to the input uncertainties to analytically calculate the effect on the output uncertainty. These methods are useful for codes whose solution algorithms require the calculation of these gradients. For example, adjoint-based solution algorithms can easily use deterministic UQ methods. The complex nonlinear structure of other codes makes the analytical calculation of these gradients very difficult, and numerical techniques to calculate them are often unreliable. As such, almost all uncertainty analyses of computer results are performed using a statistical approach.

The alternative to deterministic methods is to use a sampling method to propagate input uncertainties to the quantity of interest. This process is much more computationally intensive, but it does not require gradient information. To perform a statistical uncertainty propagation, the code is run using input uncertainties that are sampled from their respective distributions. This process is repeated until the required sample size is reached. The sample size must be large enough to have statistically meaningful results, but small enough that the computational cost is

minimized. Statistical analysis of the output parameters can be used to construct the output distributions and corresponding summary statistics (mean, standard deviation, intervals, etc.).

A popular statistical uncertainty method in nuclear engineering applications is Wilks' Formula. Given a specified percentile and confidence interval, Wilks' formula can be used to calculate the required sample size. This non-parametric uncertainty quantification method is derived and discussed in Appendix C.

3.7 Parameter Estimation

Parameter estimation is the process of optimally fitting parameters to match model output with experimental data. It is often referred to as an "inverse problem" or "inverse uncertainty quantification" because it is closely related to uncertainty quantification. For UQ, the parameter estimates are known and the goal is to estimate how these affect model output. Parameter estimation is the opposite: a set of experimental data (model output) is used to determine what input parameters will give the desired results. This relationship is outlined in Figure 3.2.

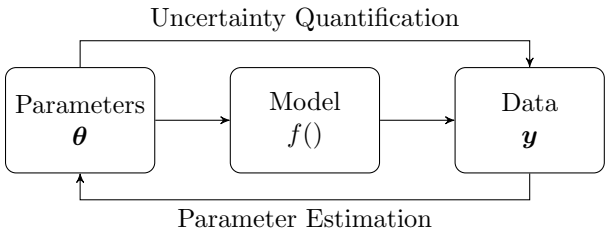

Figure 3.2: UQ and parameter estimation. UQ and parameter estimation both relate parameter estimates to experimental data using some model, but in opposite directions.

Estimated parameters can be treated as single deterministic values or as random variables. The methods discussed in this section will be capable of assessing the uncertainty in parameter estimates, and therefore parameters will be treated as nondeterministic values.

Fixed effects models use the same parameter distributions for the entire population. In most cases, these methods are sufficient if all data is governed by the same physical law or theory. Fixed effects models include fixed effects parameters $\boldsymbol{\theta}$ and an observational error ε, which is generally assumed to be identically and independently distributed (iid) with a mean of zero.

$$y_i = f\left(x_i, \boldsymbol{\theta}\right) + \varepsilon_i \tag{3.7}$$

Here, i indicates the i^{th} observation and f is the model which is fit to the experimental data. The independent variables for point i are represented as x_i. Alternatively, *mixed-effects models* are used when some physical law governs all data but there is also variation due to individuals

or components of the general population. These models are composed of *global parameters* (or fixed parameters), which identify the entire population, and *local parameters* (or random parameters) which are used to distinguish between groups.

$$y_{ij} = f\left(x_{ij}, \boldsymbol{\theta}, \beta_j\right) + \varepsilon_i \tag{3.8}$$

The model result of the i^{th} observation for the j^{th} laboratory is y_{ij}. The fixed effects parameters are again represented by $\boldsymbol{\theta}$, and the mixed-effects parameters for the j^{th} laboratory are β_j. A mixed-effects model is necessary when results from different laboratories have differing behavior due to experimental conditions, various measurement techniques, experimental errors, or physical constraints. Mixed-effects models provide a means to estimate the overall physics of the model while also quantifying the variation due to these effects.

3.7.1 Frequentist Methods

The frequentist—or classical—representation treats probabilities as the frequency with which an event occurs if an experiment is repeated a large number of times. Frequentist statistics require that parameters have a fixed but unknown value. These fixed values are not affected by the addition of more data, since the data comes from the same population. The value of the parameters is approximated using estimators, which map the sample space to a set of parameter estimates. Parameter uncertainty from a frequentist perspective is the uncertainty of these estimators, which is represented by their sampling distributions. Three frequentist techniques are discussed in this section: two for fixed effects models and one for mixed-effects models.

Asymptotic Analysis

For asymptotic frequentist analysis, the behavior of the sampling distribution for large sample sizes is considered. With a large sample size, asymptotic properties—which are based on the theory of local linearity and Taylor series expansions—can be applied. As such, the existing theory for linear Ordinary Least Squares (OLS) estimators can be used.

The use of asymptotic analysis is the most basic process used in this work for parameter estimation and it provides a first estimate of reasonable distributions. However, asymptotic analysis cannot account for nonlinear or non-Gaussian parameters. The asymptotic analysis process is outlined in Algorithm 3.1.

Bootstrapping

In cases where the local linearity assumption is not valid, e.g. for highly nonlinear problems or for problems with small sample sizes, an alternative method is necessary [22, 151]. Bootstrapping

Algorithm 3.1: Fixed effects OLS parameter estimation. This frequentist method for parameter estimation is computationally inexpensive but assumes that the parameters are a joint Gaussian distribution [156].

Input : Experimental data $\boldsymbol{y}$, state points $\boldsymbol{x}$, and model $f()$.
Output : OLS estimates of optimized parameters, variance, and covariance matrix: $\hat{\boldsymbol{\theta}}_{OLS}$, $\hat{\sigma}^2$, and $\hat{V}$, respectively.

1 Determine $\hat{\boldsymbol{\theta}}_{OLS} = \arg\min_{\boldsymbol{\theta}} \sum_{i=1}^{N} [y_i - f(x_i, \boldsymbol{\theta})]^2$.
2 Set $SS_{\boldsymbol{\theta}} = \sum_{i=1}^{N} \left[y_i - f(x_i, \hat{\boldsymbol{\theta}}_{OLS})\right]^2$.
3 Compute variance estimate $\hat{\sigma}^2 = \dfrac{SS_{\boldsymbol{\theta}}}{N-p}$.
4 Calculate the sensitivity matrix $\hat{X}_{ij} = \dfrac{\partial f(x_i, \hat{\boldsymbol{\theta}}_{OLS})}{\partial \boldsymbol{\theta}_j} \approx \dfrac{f(x_i, \hat{\boldsymbol{\theta}}_{OLS} + \epsilon_j) - f(x_i, \hat{\boldsymbol{\theta}}_{OLS})}{\epsilon}$.
5 Construct covariance estimate $\hat{V}(\boldsymbol{\theta}) = \sigma^2(\boldsymbol{X}^T\boldsymbol{X})^{-1} \approx \hat{\sigma}^2(\hat{\boldsymbol{X}}^T\hat{\boldsymbol{X}})^{-1}$.

provides an alternative way to construct sampling distributions using frequentist estimators. The same estimators are resampled to calculate a Monte Carlo approximation of the parameter distributions. Since actually sampling additional data is not practical, the existing data is resampled. The bootstrapping method utilized in this work is detailed in Algorithm 3.2. For the analyses in this work, a large number of resmaples are taken so that this method provides statistically relevant results $M = 10^4$.

Algorithm 3.2: Fixed effects bootstrapping parameter estimation. Bootstrapping is the process of resampling estimators from the same set of data to get a distribution of those estimators [22, 151].

Input : Experimental data $\boldsymbol{y}$, model $f()$, and number of bootstrap samples M.
Output : Frequentist estimates of optimized parameters, experimental error, and covariance matrix: $\boldsymbol{\theta}_{OLS}$, $\hat{\sigma}^2$, and $\hat{V}$, respectively.

1 Determine $\boldsymbol{\theta}_{OLS} = \arg\min_{\boldsymbol{\theta}} \sum_{i=1}^{N} [y_i - f(x_i, \boldsymbol{\theta})]^2$.
2 Construct standardized residuals $r_i = \sqrt{\frac{N}{N-p}}\,[y_i - f(x_i, \boldsymbol{\theta}_{OLS})]$
3 **for** $m = 1$ **to** M **do**
4 | Sample from r with replacement to generate a bootstrap sample of N standardized residuals, $\bar{r}^m$
5 | Generate synthetic data $y^m = f(x, \boldsymbol{\theta}_{OLS}) + \bar{r}^m$
6 | Calculate the OLS estimate to obtain $\boldsymbol{\theta}^m$
7 **end**
8 Now $\boldsymbol{\theta}^m$ is a chain which can be used to construct $\boldsymbol{\theta}_{OLS}$, $\hat{\sigma}^2$, and $\hat{V}$.

Maximum Likelihood Estimation for Mixed-Effects Models

In this work, a Matrix Laboratory (MATLAB©) algorithm for mixed-effects Maximum Likelihood Estimation (MLE) is used. This algorithm, `nlmefit`, provides an estimation of the mean local β and global θ parameters, along with an estimate of the covariance between the local effects, Ψ [100]. The results lack extensive uncertainty information, but they are used to indicate what correlations and state space would requires the use of a mixed-effects model.

3.7.2 Bayesian Methods

The Bayesian perspective is different than the frequentist because it treats probability as the belief that an event will occur based on prior information. Since this interpretation is subjective, it is possible that Bayesian estimates can change as more information is acquired. Bayesian statistics are also different from classical methods in that the parameters are treated as random variables which characterize the current state of knowledge. Hence, Bayesian parameters have no set true value and instead are characterized by some parameter density. Overviews of Bayesian methods are available in the literature [82, 156].

The foundation of all Bayesian methods is Bayes' Theorem:

$$P(A|B) = \frac{P(B|A)P(A)}{P(B)}, \tag{3.9}$$

where A and B are events and $P(i)$ indicates the probability of i occurring. To infer a set of parameters, $\boldsymbol{\theta} = [\theta_1, \theta_2, \ldots, \theta_p]$, based on experimental observations, $\boldsymbol{y} = [y_1, y_2, \ldots, y_n]$, Bayes' relation can be used.

$$\pi(\boldsymbol{\theta}|\boldsymbol{y}) = \frac{\mathcal{L}(\boldsymbol{y}|\boldsymbol{\theta})\pi_o(\boldsymbol{\theta})}{\int_{\mathbb{R}^p} \mathcal{L}(\boldsymbol{y}|\boldsymbol{\theta})\pi_o(\boldsymbol{\theta})d\boldsymbol{\theta}} \tag{3.10}$$

The posterior density is $\pi(\boldsymbol{\theta}|\boldsymbol{y})$, the prior distribution is $\pi_o(\boldsymbol{\theta})$, $\mathcal{L}(\boldsymbol{y}|\boldsymbol{\theta})$ is the likelihood function, and the denominator is a normalization factor which is integrated over all parameter space. The direct calculation of the normalization factor is very computationally intensive, so it is necessary to use sampling methods.

Delayed Rejection Adaptive Metropolis

The Delayed Rejection Adaptive Metropolis (DRAM) algorithm [57] is a modified form of the Metropolis-Hastings algorithm, which is one of many Markov Chain Monte Carlo (MCMC) methods for randomly sampling from posterior distributions. The DRAM algorithm uses two additional steps to increase the performance of the algorithm. The *delayed rejection* step allows for the proposal function to be updated after a rejection, which improves the mixing of the chains [58]. The *adaptive metropolis* part of the algorithm allows the covariance matrix to

be recalculated throughout the simulation, which makes the exploration of the chains more efficient [107].

The DRAM code used in this work is implemented in MATLAB© and was developed by Laine [85] and it includes Algorithms 3.3 and 3.4. The DRAM algorithm is very computationally intensive, but it requires no assumptions on parameter shape or behavior.

Algorithm 3.3: Basic DRAM method. The DRAM algorithm allows for second stage proposals [58] and updates the covariance throughout the simulation [107]. In this work, a Gaussian likelihood function and uninformative priors are used [85, 156].

Input : Experimental data $\boldsymbol{y}$, model $f()$, chain length M, error variance update parameters n_s and σ_s^2, $s_p = 2.38^2/p$, iterations between covariance updates k_o.

Output : Bayesian chain, which can be used to construct posterior distributions.

Use Algorithm 3.1 to calculate $\boldsymbol{\theta}_{OLS}$, σ_0^2, and V_0.
Set initial residuals $R_0 = \text{chol}(V_0)$.
for $k = 1$ **to** M **do**
    Sample $z_k \sim \mathcal{N}(0, I)$.
    Construct candidate $\boldsymbol{\theta}^* = \boldsymbol{\theta}^{k-1} + R_{k-1}^T z_k$.
    Sample $u_\alpha \sim \mathcal{U}(0, 1)$
    Compute $SS_{\boldsymbol{\theta}^*} = \sum_{i=1}^{N} \left[y_i - f\left(x_i, \boldsymbol{\theta}^*\right) \right]$
    Compute $\alpha\left(\boldsymbol{\theta}^* | \boldsymbol{\theta}^{k-1}\right) = \min\left(1, e^{-\left[SS_{\boldsymbol{\theta}^*} - SS_{\boldsymbol{\theta}^{k-1}}\right]/2\sigma_{k-1}^2}\right)$
    if $u_\alpha < \alpha$ **then**
        Set $\boldsymbol{\theta}^k = \boldsymbol{\theta}^*$ and $SS_{\boldsymbol{\theta}^k} = SS_{\boldsymbol{\theta}^*}$
    else
        Algorithm 3.4.
    end
    Update $\sigma_k^2 \sim \text{Inv-gamma}\left(a, b\right)$, where $a = 0.5(n_s + N)$ and $b = 0.5(n_s\sigma_s^2 + SS_{\boldsymbol{\theta}^k})$.
    if $\text{mod}(k, k_0) = 1$ **then**
        Update $V_k = s_p \,\text{cov}(\boldsymbol{\theta})$ and $R_k = \text{chol}(V_k)$
    else
        $V_k = V_{k-1}$ and $R_k = R_{k-1}$
    end
end

All DRAM analyses in this work will use the OLS estimates of parameter values as initial estimates. Noninformative priors will be used, since the parameters are generally fit to experimental data and have no physical meaning. Standard practice in the nuclear industry is to bound the parameters by $[0, 2\boldsymbol{\theta}_{OLS}]$ [114]. All analyses take 10^4 samples from the posterior after a burn-in period of 10^5 chains. The large number of burn-in samples is sufficient to converge the chains, but future work will address the convergence in a more quantitative way [18, 48].

Algorithm 3.4: Delayed rejection part of DRAM. The delayed rejection part of DRAM, outlined in [107], allows the algorithm to propose a second candidate, which significantly increases the mixing of the chains [156].

Set the design parameter $\gamma_2 < 1$. This work uses $\gamma_2 = 1/5$.
Sample $z_k \sim \mathcal{N}(0, I)$.
Construct a second state candidate $\boldsymbol{\theta}^{*2} = \boldsymbol{\theta}^{k-1} + \gamma_2 R_{k-1}^T z_k$.
Sample $u_{a_2} \sim \mathcal{U}(0, 1)$.
Compute $SS_{\boldsymbol{\theta}^{*2}} = \sum_{i=1}^{N} \left[y_i - f\left(x_i, \boldsymbol{\theta}^{*2}\right)\right]^2$.
Compute the proposal distribution
$J(\boldsymbol{\theta}^a|\boldsymbol{\theta}^b) = \frac{1}{\sqrt{(2\pi)^p\,|V|}} \exp\left(-\frac{1}{2}\left[(\boldsymbol{\theta}^a - \boldsymbol{\theta}^b)V^{-1}(\boldsymbol{\theta}^a - \boldsymbol{\theta}^b)^T\right]\right)$.
Compute $\alpha_2\left(\boldsymbol{\theta}^{*2}|\boldsymbol{\theta}^{k-1}, \boldsymbol{\theta}^*\right) = \min\left(1, \frac{\mathcal{L}(\boldsymbol{\theta}^{*2}|\boldsymbol{y})J(\boldsymbol{\theta}^*|\boldsymbol{\theta}^{*2})\left[1 - \alpha(\boldsymbol{\theta}^*|\boldsymbol{\theta}^{*2})\right]}{\mathcal{L}(\boldsymbol{\theta}^{k-1}|\boldsymbol{y})J(\boldsymbol{\theta}^*|\boldsymbol{\theta}^{k-1})\left[1 - \alpha(\boldsymbol{\theta}^*|\boldsymbol{\theta}^{k-1})\right]}\right)$ where $\mathcal{L}$ is the likelihood.
if $u_{\alpha_2} < \alpha_2$ **then**
  Set $\boldsymbol{\theta}^k = \boldsymbol{\theta}^{*2}$ and $SS_{\boldsymbol{\theta}^k} = SS_{\boldsymbol{\theta}^{*2}}$.
else
  Set $\boldsymbol{\theta}^k = \boldsymbol{\theta}^{k-1}$ and $SS_{\boldsymbol{\theta}^k} = SS_{\boldsymbol{\theta}^{k-1}}$.
end

3.8 Identifiability

A prerequisite of calibration is that the parameterized model is identifiable, meaning that there exists a unique parameter set which can be determined from the observations. The parameter set $\boldsymbol{\theta} = \{\theta_1, \theta_2, \ldots, \theta_k\}$ is identifiable at $\boldsymbol{\theta}^*$ if, for any admissible parameter set, $Y(\boldsymbol{\theta}) = Y(\boldsymbol{\theta^*})$ implies that $\boldsymbol{\theta} = \boldsymbol{\theta^*}$. The parameter set $\boldsymbol{\theta}$ is identifiable if this holds for all $\boldsymbol{\theta}^*$ in the parameter space.

A sensitivity matrix is approximated numerically at each calibration state point.

$$X_{ij} = \frac{\partial Y_i}{\partial \boldsymbol{\theta}_j} \approx \frac{Y_i(\boldsymbol{\theta} + \varepsilon_j) - Y_i(\boldsymbol{\theta})}{\varepsilon_j} \tag{3.11}$$

If X is rank deficient, it is necessary to determine the identifiable parameter subspace. To accomplish this, a QR decomposition with rank-revealing column pivoting is used [156].

The sensitivity matrix is decomposed into orthogonal (Q) and upper triangular (R) parts, $XP = QR$, where P is a permutation matrix which pivots the columns of X so that R has an $r \times r$ upper triangular block whose diagonal elements are nonzero. This process reveals the r vectors of Q which correspond to the identifiable parameters, where Q_i (the r diagonal values in Q) quantify the identifiability of the corresponding parameters.

3.9 Sensitivity Studies

The goal of sensitivity analysis is to determine which input parameters influence the quantities of interest. These analyses are used to eliminate inputs that have relatively little importance, which can focus future development and make calibration, optimization, and uncertainty analyses simpler and more manageable. Additionally, some methods can measure model smoothness, nonlinear trends, simulation robustness, or interactions between inputs. As such, preliminary sensitivity studies are critical to any uncertainty analysis.

Sensitivity measures can either be local or global. *Local sensitivities* measure the variability of the response as inputs are varied about one point in state space. These measures are often used in optimization, adjoint methods, and model calibration. Local sensitivities can be calculated using finite difference approximations, sensitivity equations, or automatic differentiation [156]. *Global sensitivity* aims to apportion uncertainty in the output to different inputs. Global sensitivity measures are often composed of local measures sampled from the parameter space. They can be categorized as regression, variance, or screening-based methods [156]. In this work, three global sensitivity methods are used.

CHAPTER

4

CTF-RESIDUAL

The original version of CTF was optimized to run on computers with limited capabilities and the code architecture has remained essentially stagnant since then. Recent work has focused on modernizing the code. A residual form, COBRA-IE, is used at Bettis Atomic Power Laboratory [11, 20, 91]. Similar work, the state of which is the topic of this chapter, has commenced at NCSU to introduce a residual formulation into the CASL version of the code.

The initial development of CTF-R was performed by Chris Dances at Pennsylvania State University (PSU) [30, 31, 32, 33]. The first version did not include any closure relationships and had a rudimentary one-dimensional Cartesian form of the conduction equation. His work has been expanded to include closure relationships for frictional and gravitational pressure drops, heat transfer between the solid and liquid, and solution of the one-dimensional cylindrical conduction equation [135]. A manual for CTF-R with one-dimensional single phase flow was published by CASL [136]. The addition of a lateral momentum equation to CTF-R has also been detailed previously [138, Chapter 6].

The basic theory and benefits of CTF-R are discussed in Section 4.1. The conservation equations are given in Section 4.2 in both continuous and discretized forms. The implementation is discussed in Section 4.3. All verification and validation of CTF-R is outlined in Section 4.4.

4.1 Theory

As discussed in Section 2.4, the discretized conservation equations solved in a computational tool are often organized into a matrix system.

$$J\delta x = -F(x) \tag{4.1}$$

Here, J is the Jacobian matrix, δx is the array of state variable updates, and $F(x)$ is the evaluated residual equations. Here, the update array is defined as the difference in the state variables between consecutive iterations.

$$\delta x = x^{n+1} - x^k \tag{4.2}$$

Each state variable is indicated by x, the new time value is $n+1$, and the old time value is n. Each fluid cell has three residuals, which correspond to the mass, energy, and momentum equations. Each solid cell has a single residual, which corresponds to the solid energy equation.

$$\delta P = P^{n+1} - P^n \tag{4.3a}$$

$$\delta h = h^{n+1} - h^n \tag{4.3b}$$

$$\delta u = u^{n+1} - u^n \tag{4.3c}$$

$$\delta T = T^{n+1} - T^n \tag{4.3d}$$

The equation of state is incorporated into the other conservation equations, so there is no corresponding residual in density.

CTF-R infrastructure was designed to use Newton's method to resolve nonlinearities in the solution (Algorithm 2.2), but it currently only takes a single linear iteration. This is a decent approximation for single phase flow since it is not highly nonlinear, but should be corrected in the future. Using this single-iteration time iteration scheme, the Jacobian is first evaluated numerically.

$$J_{i,j} = \frac{\delta F_j(x^n)}{\delta x_i} \approx \frac{F_j(x^n + \epsilon_i) - F_j(x^n)}{\epsilon_i} \tag{4.4}$$

Here, $F_j()$ indicates the j^{th} conservation equation and ϵ_i is a small perturbation to the i^{th} state variable. Next, the remaining terms in the conservation equations are evaluated, $F(x^n)$. Then the residual vector is calculated using a linear algebra library.

$$\delta x = -J^{-1}F(x^n) \tag{4.5}$$

The new time values of the state variables can then be calculated $x^{n+1} = x^n + \delta x$. After each

iteration, the state variables are updated to the correct time levels and the process is repeated until convergence. CTF-R currently uses CTF's convergence algorithm, which sets tolerances on global conservation and the change in state variables from one iteration to the next.

In CTF-R, each conservation equation $F(x)$ is coded as an individual function and the state variables are stored as a matrix with x^n, x^k, and x^{n+1} values. Keeping the data structures in this generalized form and constructing the Jacobian numerically provides many benefits.

- The conservation equations are easier to understand and locate, which reduces the time necessary to learn the code.
- The equations can be changed easily, which allows the the implicitness, discretization, and physics to be adjusted for application to a specific case.
- A true steady state solution can be found by removing the temporal terms from the conservation equations.
- Conservation equations can be added or removed from the Jacobian.
- More tools from the numerical solver can be utilized, including more advanced solution algorithms, built-in parallelization, and direct coupling to other codes.
- Since Equation 4.5 is used to calculate the residual array directly, the residuals can be used to assess convergence without any additional computations. This is a significant improvement over the traditional ad hoc method used in the CASL version of CTF.
- CTF-R has been designed to enable VVUQ. All empirical models can be disabled, there is no under relaxation, and coded models have been provided with suggest parameter uncertainties (see Chapter 5). Most importantly, every model currently in the code has at least a minimal level of Verification and Validation (V&V) (See Section 4.4).
- The full Jacobian is available, which allows a variety of solution algorithm options. Different nonlinear iterations can be added, and the Jacobian can be row-reduced to the pressure matrix.

CTF-R is early in its development, but these benefits act as motivation to gradually increase its modeling capabilities. Currently, CTF-R is single-phase and solves the conservation equations outlined in Section 4.2. The code implementation is briefly outlined in Section 4.3, and all V&V work is discussed in Section 4.4. The chapter concludes with a discussion of shortcomings of the current implementation, future applications, and future work in Section 4.5.

4.2 Conservation Equations

CTF solves eight conservation equations for the fluid domain, but only four of these have been implemented in CTF-R. These are the conservation of mass, energy, axial momentum, and lateral momentum for liquid water. There is also an energy equation for solid components. All

four of these equations are summarized in the following sections in both their continuous and discretized form. All equations are consistent with the current CTF-R implementation. See Appendix A for derivations of the enthalpy and both momentum equations.

4.2.1 Discretization

The discretization nomenclature in both axial and lateral directions are shown schematically in three dimensions in Figures 4.1a and 4.1b. The black cubes are scalar cells and the red cubes are vector cells. The black dots indicate the location of all scalar quantities, and the red arrows define velocities. All discretized equations in this section are consistent with this nomenclature.

4.2.2 Mass Equation

The conservation of mass equation, or continuity equation, in CTF-R is relatively simple.

$$\frac{\partial \rho}{\partial t} + \frac{\partial \rho u}{\partial x} + \frac{\partial \rho w}{\partial z} - \kappa_1 \frac{\partial^2 \rho}{\partial z^2} = 0 \tag{4.6}$$

The independent variables of time and space are represented by t, x, and z, where x is in the upward axial direction and z is in the lateral direction. The density, mean axial velocity, and mean lateral velocity are respectively ρ, u, and w. The first two terms are the rate of change in density and advection in the axial direction, the third is lateral transfer. The final term in the mass equation is turbulent mixing, which smooths density in the lateral direction. The constant κ_1 has units ft^2/s and is currently a tunable input parameter.

In CTF-R, the mass equation is discretized as follows:

$$\frac{\rho_i^{n+1} - \rho_i^n}{\Delta t} + \frac{\dot{\rho}_{i+1/2}^n u_{i+1/2}^{n+1} - \dot{\rho}_{i-1/2}^n u_{i-1/2}^{n+1}}{\Delta x} + \sum_g^{N_g} \left[\frac{\dot{\rho}_g^n w_g^n}{L_g} - \kappa_1 \frac{\rho_{g+1/2}^n - \rho_{g-1/2}^n}{L_g^2} \right] = 0. \tag{4.7}$$

Here, i indicates the current scalar cell, $i - 1/2$ is the momentum cell below it, and $i + 1/2$ is the momentum cell above it (see Figure 4.1a). The summation is over all gaps g connected to the scalar cell. The gaps are defined such that lateral velocity w_g is from the lower indexed channel $g - 1/2$ to the higher indexed channel $g + 1/2$ (see Figure 4.1b). The lateral distance between cells $g - 1/2$ and $g + 1/2$ is L_g. The last time step values are indicated by an n superscript and new time values are at $n + 1$. The dotted quantities are upwinded in space.

$$\dot{\rho}_{i+1/2}^n = \begin{cases} \rho_i^n, & u_{i+1/2}^n > 0 \\ \rho_{i+1}^n, & u_{i+1/2}^n \leq 0 \end{cases} \tag{4.8a}$$

$$\dot{\rho}_{i-1/2}^n = \begin{cases} \rho_{i-1}^n, & u_{i-1/2}^n > 0 \\ \rho_i^n, & u_{i-1/2}^n \leq 0 \end{cases} \tag{4.8b}$$

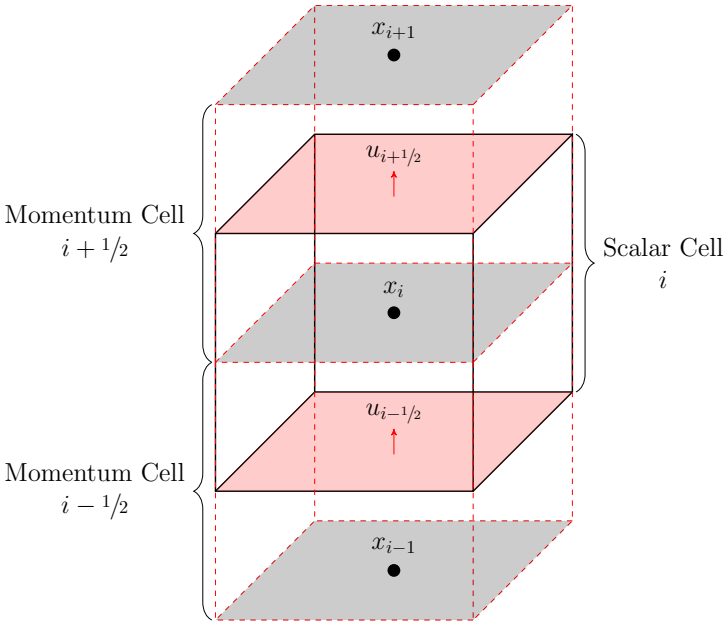

(a) Axial mesh

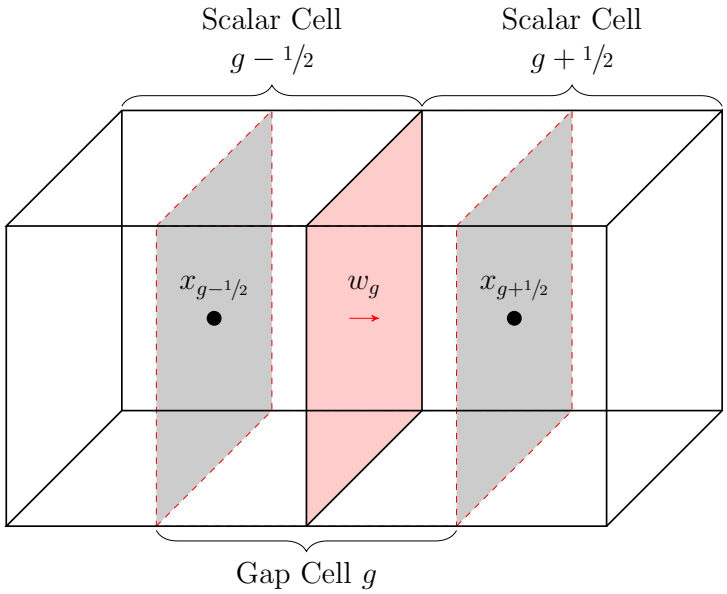

(b) Lateral mesh

Figure 4.1: CTF-R staggered mesh. This figure establishes the nomenclature used to discretize the conservation equations in CTF-R. Scalar values, such as density, enthalpy, and pressure are indicated by x and defined for each scalar cell (black box) on the gray plane. Velocity vectors are defined on the red planes, which are centered in the momentum cells (red dashed box).

$$\dot{\rho}_g^n = \begin{cases} \rho_{g-1/2}^n, & w_g^n > 0 \\ \rho_{g+1/2}^n, & w_g^n \leq 0 \end{cases} \tag{4.8c}$$

4.2.3 Energy Equation

The energy equation in CTF-R is in enthalpy form, which is inherited from CTF. For a derivation and discussion of this equation, see Section A.1.

$$\rho \frac{\partial h}{\partial t} + \rho u \frac{\partial h}{\partial x} - \frac{\partial P}{\partial t} + \frac{\partial \rho h w}{\partial z} - \kappa_2 \frac{\partial^2 h}{\partial z^2} = \frac{S_{ht}}{\not{V}} \tag{4.9}$$

The specific enthalpy is h, P is pressure, and cell volume is $\not{V}$. The first two terms are the change rate and advection of enthalpy. The pressure work is the third term, followed by lateral advection and turbulent mixing. The tunable parameter κ_2 has units $lbm/ft \cdot s$. The source S_{ht} is heat transfer from the surface of nuclear fuel rods to the fluid and it is defined in Section 4.2.9.

In CTF-R, the enthalpy conservation equation is discretized as follows:

$$\rho_i^n \frac{h_i^{n+1} - h_i^n}{\Delta t} + \rho_i^n \bar{u}_i^n \left. \frac{\dot{\partial h}}{\partial x} \right|_i^n - \frac{P_i^{n+1} - P_i^n}{\Delta t} + \sum_g^{N_g} \left[\frac{(\dot{\rho h})_g^n w_g^n}{L_g} - \kappa_2 \frac{h_{g+1/2}^n - h_{g-1/2}^n}{L_g^2} \right] = \frac{S_{ht}}{\not{V}_i}. \tag{4.10}$$

Here, i indicates the current scalar cell, $i-1$ is the scalar cell below it, and $i+1$ is the scalar cell above it. The sum over gaps g connected to the scalar cell uses the same nomenclature as Equation 4.6. The dotted quantities are upwinded for numerical stability.

$$\left. \frac{\dot{\partial h}}{\partial x} \right|_i^n = \begin{cases} (h_i^n - h_{i-1}^n)/\Delta x, & \bar{u}_i^n > 0 \\ (h_{i+1}^n - h_{i-1}^n)/2\Delta x, & \bar{u}_i^n = 0 \\ (h_{i+1}^n - h_i^n)/\Delta x, & \bar{u}_i^n < 0 \end{cases} \tag{4.11a}$$

$$(\dot{\rho h})_g^n = \begin{cases} (\rho h)_{g-1/2}^n, & w_g^n > 0 \\ (\rho h)_{g+1/2}^n, & w_g^n \leq 0 \end{cases} \tag{4.11b}$$

The average velocity in the advective term is currently defined as a linear average of the surrounding velocities: $\bar{u}_i^n = (u_{i+1/2}^n + u_{i-1/2}^n)/2$. The cell volume is calculated using the input continuity area for the channel A_c and the axial spacing Δx: $\not{V}_i = A_c \Delta x$.

4.2.4 Axial Momentum Equation

Derivation of the CTF axial momentum equation is in Section A.2.

$$\frac{\partial u}{\partial t} + u \frac{\partial u}{\partial x} + \frac{1}{\rho} \frac{\partial P}{\partial x} + \frac{1}{\rho} \frac{\partial \rho u w}{\partial z} - \frac{\kappa_3}{\rho} \frac{\partial^2 u}{\partial z^2} = g + S_f \tag{4.12}$$

The first two terms are the material derivative of velocity, followed by the pressure force. The final two terms on the left side are lateral advection and turbulent mixing. The tunable parameter in the turbulent mixing model, κ_3, has units $lbm/ft \cdot s$. The gravitational constant is g, and the friction source S_f is defined in Section 4.2.8.

In CTF-R, the momentum equations are discretized on vector cells.

$$\begin{aligned}\frac{u_{i+1/2}^{n+1} - u_{i+1/2}^{n}}{\Delta t} + u_{i+1/2}^{n} \left.\frac{\dot{\partial u}}{\partial x}\right|_{i+1/2}^{n} + \frac{1}{\bar{\rho}_{i+1/2}^{n}} \frac{P_{i+1}^{n+1} - P_{i}^{n+1}}{\Delta x} \\ + \frac{1}{\bar{\rho}_{i+1/2}^{n}} \sum_{g}^{N_g} \left[\frac{(\dot{\rho u})_{g}^{n} w_{g}^{n}}{L_g} - \kappa_3 \frac{u_{g+1/2}^{n} - u_{g-1/2}^{n}}{L_g^2} \right] = g + S_f\end{aligned} \tag{4.13}$$

The scalar cell density is not averaged: $\bar{\rho}_{i+1/2}^{n} = \rho_{i}^{n}$. This is a decent approximation for single phase water, since the density is relatively constant. For other applications, an average density should be used. The dotted quantities are upwinded.

$$\left.\frac{\dot{\partial u}}{\partial x}\right|_{i+1/2}^{n} = \begin{cases} (u_{i+1/2}^{n} - u_{i-1/2}^{n})/\Delta x, & u_{i+1/2}^{n} > 0 \\ (u_{i+3/2}^{n} - u_{i-1/2}^{n})/2\Delta x, & u_{i+1/2}^{n} = 0 \\ (u_{i+3/2}^{n} - u_{i+1/2}^{n})/\Delta x, & u_{i+1/2}^{n} < 0 \end{cases} \tag{4.14a}$$

$$(\dot{\rho u})_{g}^{n} = \begin{cases} (\rho u)_{g-1/2}^{n}, & w_{g}^{n} > 0 \\ (\rho u)_{g+1/2}^{n}, & w_{g}^{n} \leq 0 \end{cases} \tag{4.14b}$$

The densities in the lateral source term are averaged to the axial momentum cells: $\rho_{g+1/2} = (\rho_{i,g+1/2}^{n} + \rho_{i+1,g+1/2}^{n})/2$ and $\rho_{g-1/2} = (\rho_{i-1,g-1/2}^{n} + \rho_{i,g-1/2}^{n})/2$.

4.2.5 Lateral Momentum Equation

The CTF-R lateral momentum equation is derived in Section A.3.

$$\frac{\partial w}{\partial t} + \frac{1}{\rho} \frac{\partial P}{\partial z} = H|w|w \tag{4.15}$$

The change in lateral velocity is due to lateral pressure gradients, with a form loss opposing the change. Note that the form loss—which is implemented to model the advection term and lateral friction—is tunable using the input form loss H. The equation is discretized.

$$\frac{w_{g}^{n+1} - w_{g}^{n}}{\Delta t} + \frac{1}{\bar{\rho}_{g}^{n}} \frac{P_{g+1/2}^{n+1} - P_{g-1/2}^{n+1}}{L_g} = H|w_{g}^{n}|w_{g}^{n} \tag{4.16}$$

The gap density is a linear average of the surrounding scalar cells, $\bar{\rho}_{g}^{n} = (\rho_{g+1/2}^{n} + \rho_{g-1/2}^{n})/2$.

4.2.6 Equation of State

CTF-R uses the CTF equation of state. The change in density is a linear combination of changes due to pressure and enthalpy changes. The partial derivatives are evaluated using the existing CTF code.

$$\Delta\rho = \frac{\partial\rho}{\partial P}\Delta P + \frac{\partial\rho}{\partial h}\Delta h \tag{4.17}$$

Or, in discretized form:

$$\rho^{n+1} = \rho^n + \left.\frac{\partial\rho}{\partial P}\right|_i^n (P_i^{n+1} - P_i^n) + \left.\frac{\partial\rho}{\partial h}\right|_i^n (h_i^{n+1} - h_i^n). \tag{4.18}$$

4.2.7 Solid Energy Equation

CTF-R uses a simplified form of the conduction equation to calculate the temperature profile in a nuclear fuel rod. First, thermal expansion is neglected, so the cold mass of material is used. Second, the equation is simplified to eliminate radial and azimuthal conduction. Third, this equation assumes that specific heat c_p is a linear function of temperature. The continuous control volume form of the conduction equation is used.

$$Mc_p\frac{\partial T}{\partial t} = \sum_s q_s'' A_s + q'''\forall - S_{ht} \tag{4.19}$$

Here, M is the cold mass of the material, c_p is specific heat, and T is the temperature of the solid. For each surface s connected to a cell, q_s'' is the heat flux and A_s is the surface area available to heat transfer. The volumetric heat source is q''' and $\forall$ is volume of the current cell. Finally, S_{ht} is heat transferred from the solid to the fluid.

The equation is discretized according to Figure 2.3, where each cell in the fuel is equally spaced.

$$M_i c_{pi}\frac{T_i^{n+1} - T_i^n}{\Delta t} = \frac{T_{i-1}^n - T_i^{n+1}}{R_{i-3/4}^n + R_{i-1/4}^n} + \frac{T_{i+1}^n - T_i^{n+1}}{R_{i+3/4}^n + R_{i+1/4}^n} + q_i'''\forall_i - S_{ht} \tag{4.20}$$

Here, i is the current annular solid cell, $i-1$ is the cell inside it, and $i+1$ is the cell outside it. The resistances are defined according to Table 2.1 depending on their location and they include all information about geometry and thermal conductivity. Note that q_i''' is assumed to be zero in the gap and cladding regions and $S_{ht} = 0$ for every cell except the rod surface.

4.2.8 Friction Source Term

Friction in CTF-R appears as a source term in the axial momentum equation, Equation 4.12. The force of friction is calculated using the Darcy friction factor f.

$$S_f = \frac{f|u|u}{2D_h} \tag{4.21}$$

Here, the hydraulic diameter is $D_h = 4A_c/P_w$. In discretized form, one velocity is evaluated at new time and the other at the previous time step.

$$S_f = \frac{f^n|u^n_{i+1/2}|u^{n+1}_{i+1/2}}{2D_h} \tag{4.22}$$

The friction factor is a function of Reynolds number and surface roughness. CTF-R uses the same function to calculate friction factor as the main version of the code, where `IRFC` is the input option. There are five options that correspond to `IRFC` values from 1 to 5, respectively [13]: the original CTF correlation, modified version of the McAdams Correlation [103], Zigrang-Sylvester Correlation [179], modified Churchill Correlation [24], and a user defined function.

4.2.9 Heat Transfer Source Term

Heat transfer between the solid and coolant is implemented as a source term in both the solid and fluid energy equations. The wall heat transfer is the temperature potential multiplied by a heat transfer coefficient.

$$S_{ht} = hA_s(T_w - T_f) \tag{4.23}$$

Here, h is the heat transfer coefficient, A_s is the surface area available to heat transfer, T_w is the temperature of the wall, and T_f is the temperature of the fluid. The term is discretized explicitly.

$$S_{ht} = h^n A_s(T^n_{co} - T^n_f) \tag{4.24}$$

The heat transfer coefficient is a constant in laminar flow [157] and it is calculated using the Dittus-Boelter correlation in turbulent flow [38].

$$h = \frac{k_l}{D_h} \max\left[7.86, 0.023\, Re^{0.8} Pr^{0.4}\right] \tag{4.25}$$

4.3 Implementation

The current version of CTF-R splits away from CTF after the input is read and code variables are instantiated. This separation of the solution algorithms ensures that future merge conflicts will be minimized.

After the input deck is read and all working arrays are initialized, CTF-R creates its own copies of the arrays (pressure, density, enthalpy, and velocity) to work with. These arrays are used to independently construct and solve the Jacobian. Once the Jacobian solution is found,

the CTF-R results are copied back to the CTF arrays for the output process. In this way, the CTF and CTF-R input/output processes are identical. The general structure of CTF and how it relates to CTF-R is outlined in Algorithm 4.1.

Algorithm 4.1: CTF-R call structure. CTF-R and CTF solution algorithms are called separately in the `Outer_iteration` module. Blue text indicates a call or processes that is relevant to the CTF-R algorithm and comments indicate important connection points between the two codes.

```
1  cobra_tf
2      Init_tf
3          Pre_input_initialization
4          Input // Read Card 20 for residual options
5          Post_input_initialization // Initializes CTF-R arrays
6      Trans
7          pre_trans
8          for n = 1 to N do
9              Time_step
10                 Timestep
11                 prep3d // CTF working arrays copied to CTF-R arrays
12                 heat
13                 Outer_iteration
14                     if residual form then
15                         inner_iteration
16                             build_matrix
17                             PETSc_JacSolve
18                             get_deltas
19                             update_variables
20                             check_convergence
21                     else
22                         xschem
23                         gssolv
24                     end
25                 post3d // CTF-R arrays copied back to CTF
26             post_step
27         end
28         post_trans
29     Cobra_cleanup
```

There are four files specific to CTF-R: (1) `residual_drivers.F90` contains the high-level subroutines of the code, (2) `residual_functions.f90` has all residual functions and other low-level parts of the code, (3) `Mod_Jacobian_construction.f90` defines an object and associated

methods which are used to numerically construct the Jacobian, and (4) `Mod_variable_index.f90` which defines a convenient structure for storing index information.

The Jacobian matrix is solved using the linear algebra package PETSc. The Generalized Minimal Residual (GMRES) solution algorithm [146] is used with relative and absolute tolerances available to the user via input.

4.4 SQA and V&V

SQA and V&V activities were discussed in Chapter 3. In this section, a series of defect, verification, and validation tests are outlined to reinforce confidence in the predictions of CTF-R.

4.4.1 Software Quality Assurance

Defect tests were designed to test friction, solid conduction, heat transfer, and lateral transfer. All test problems model subchannels with conditions and geometry similar to that in Table 4.1.

Table 4.1: Boundary conditions and geometry of CTF-R defect tests. The defect tests use conditions representative of a PWR channel at normal operating conditions.

Parameter	Symbol	Value	Unit
Outlet pressure	P_{out}	152	bar
Inlet temperature	T_{in}	292	$°C$
Mass flow rate	$\dot{m}$	0.365	kg/s
Flow area	A	1.1445	cm^2
Wetted perimeter	P_w	3.43125	cm
Axial height	L	3.6	m
Rod outer diameter	D_{co}	1.0922	cm
Fuel outer diameter	D_{fo}	0.9400	cm

Constant Friction Factor with Exact Solution

Under steady state and isothermal conditions, the one-dimensional momentum equation (Equation 4.12) can be solved if the friction factor is a known constant.

$$\frac{\partial P}{\partial x} - \rho g = f\frac{\rho u^2}{2D_h} \tag{4.26}$$

$$\int_{P(x)}^{P_{out}} \partial P = \int_x^L \left[f\frac{\rho u}{2D_h} + \rho g \right] \partial x \tag{4.27}$$

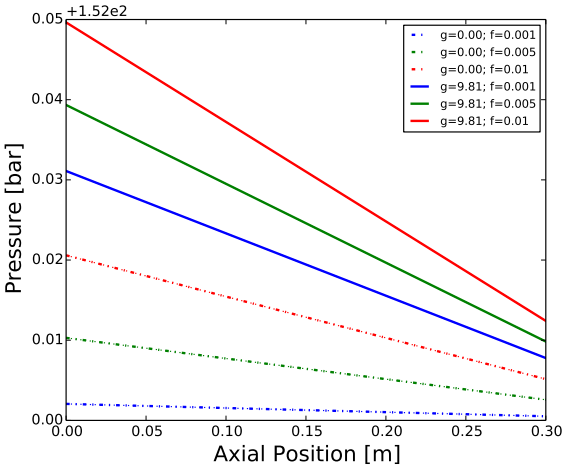

(a) Predicted and analytical pressure

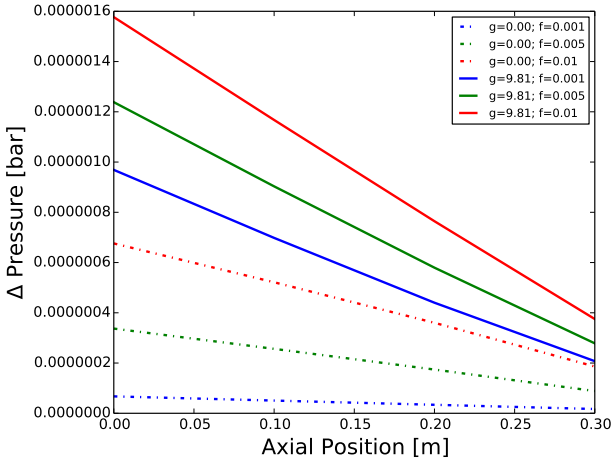

(b) Comparison of code results with Equation 4.28

Figure 4.2: Constant friction factor defect test results. The defect test models a subchannel at PWR conditions and three different friction factors with gravity both enabled and disabled. All tests match the analytical solution to within $2 \times 10^{-6}\, bar$.

$$P(x) = P_{out} - \left[f \frac{\rho u}{2D_h} + \rho g \right] (L - z) \tag{4.28}$$

The results for these tests problems are shown in Figure 4.2a for a variety of constant friction factors with and without gravity. A comparison to the analytical solution is shown in Figure 4.2b. CTF-R accurately predicts the steady state pressure gradient under these conditions.

Friction Factor Correlations with Approximate Solution

When the friction factor is calculated using a correlation, it varies slightly throughout the axial length due to variations in the Reynolds number. This case cannot be solved analytically, but an approximate solution is appropriate because the error is small in single phase flow. Isothermal steady state flow is modeled at different inlet temperatures, pipe diameters, outlet pressures, and axial lengths. The approximate solution is an integral form of Equation 4.28.

$$\Delta P \approx f L \frac{\rho u^2}{2D_h} + \rho g L \tag{4.29}$$

The friction factor is calculated using all four CTF-R correlations. The fluid properties are evaluated at the inlet temperature and outlet pressure. These component tests are performed for a large range of geometry and operating conditions: $1 \leq D \leq 10\, cm$, $0 \leq \epsilon/D \leq 0.05$, $293 \leq T_{in} \leq 374\, K$, $0.1 \leq P_{out} \leq 15.5\, MPa$, and $0.25 \leq v_{in} \leq 5\, m/s$. The results of the 576 defect tests are shown in Figure 4.3. They indicate correct implementation, where the constant property assumption likely causes most of the error.

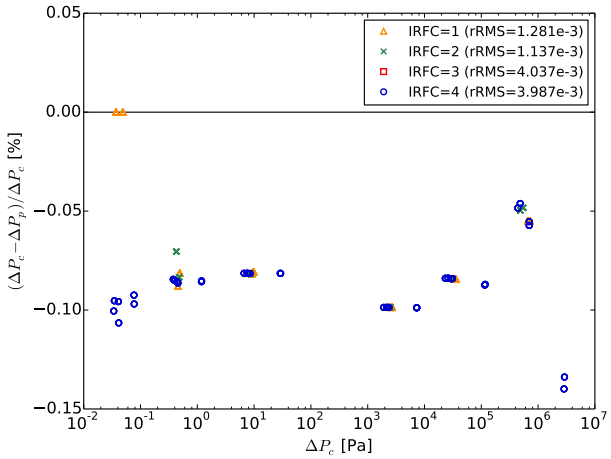

Figure 4.3: Friction factor correlation defect test results. The approximately calculated solution is ΔP_c and the code prediction is ΔP_p. All four friction factor correlations are tested with 148 different combinations of geometry and conditions. The maximum error is less than 0.15% and the rRMSs are shown in the legend.

Constant Conductivities

The conduction equation can be solved for a problem with constant conductivities. For a steady state case with constant properties, the temperature profile inside the fuel pin is calculated analytically starting with the cylindrical conduction equation.

$$\rho c_p \frac{\partial T}{\partial t} = \frac{1}{r}\frac{\partial}{\partial r}\left(kr\frac{\partial T}{\partial r}\right) + q''' \tag{4.30}$$

$$\frac{k}{r}\frac{\partial}{\partial r}\left(r\frac{\partial T}{\partial r}\right) + q''' = 0 \tag{4.31}$$

$$k\frac{\partial T}{\partial r} + q'''\frac{r}{2} + \frac{C_1}{r} = 0 \tag{4.32}$$

Now the boundary condition at zero is applied to find $C_1 = 0$, then the equation is integrated again.

$$\Delta T = \frac{q'''r^2}{4k} \tag{4.33}$$

Applying this to various regions of the fuel gives the following analytical equations for temperature at the inside of the cladding T_{ci}, surface of the fuel T_{fo}, and centerline temperature T_{cl} [162]:

$$T_{ci} = T_{co} + \frac{\ln\frac{r_{co}}{r_{ci}}}{2\pi k_c} \tag{4.34a}$$

$$T_{fo} = T_{ci} + \frac{q'}{2\pi r_{fo} h_g} \tag{4.34b}$$

$$T_{cl} = T_{fo} + \frac{q'}{4\pi k_f}. \tag{4.34c}$$

CTF-R temperature profiles are compared to these solutions. The results are shown in Figure 4.4. The analytical solution is only compared at the outside of the cladding, inside of the cladding, outside of the fuel, and the fuel centerline. It is shown that all of these predictions are within $0.3\,K$ of the analytical solution, with the largest difference at the centerline. Not only is the centerline the furthest from the fluid boundary condition, but there is significant error due to the temperature interpolation at the center of the pin.

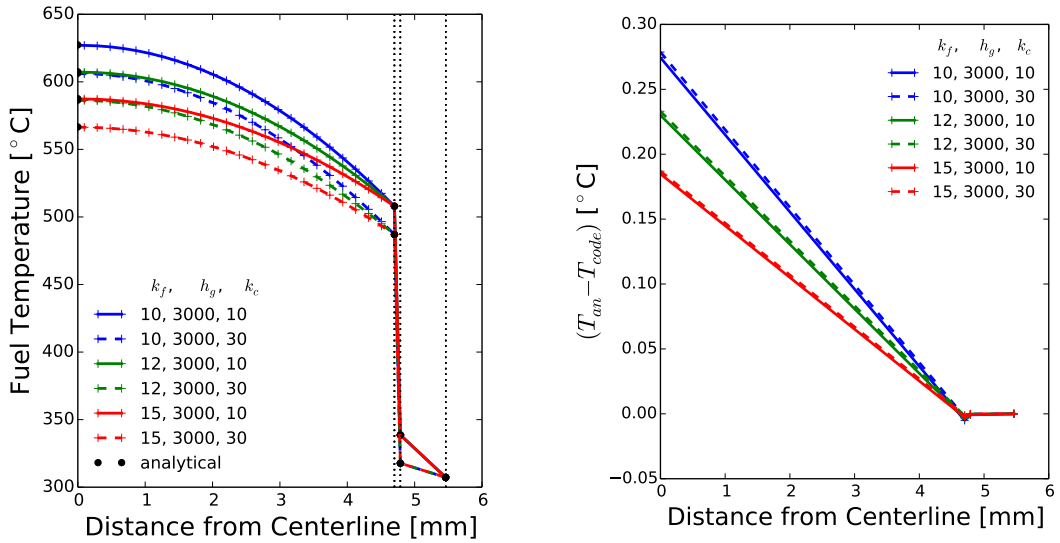

(a) Temperature distribution

(b) Comparison with Equation 4.34

Figure 4.4: Conduction equation defect test results. Six cases with varying conductivities are tested and compared to the analytical solution. The largest error is at the fuel centerline.

Heat Transfer with Uniform Power Profile

Given a constant axial power profile and assuming that all power is deposited into the coolant, the coolant enthalpy rise can be calculated analytically. Steady state is assumed without the pressure gradient or dissipation terms [162].

$$\dot{m}\frac{dh}{dx} = q'(z) \tag{4.35}$$

$$\dot{m}\int_{h_{in}}^{h(x)} dh = \int_0^x q'(x)dx \tag{4.36}$$

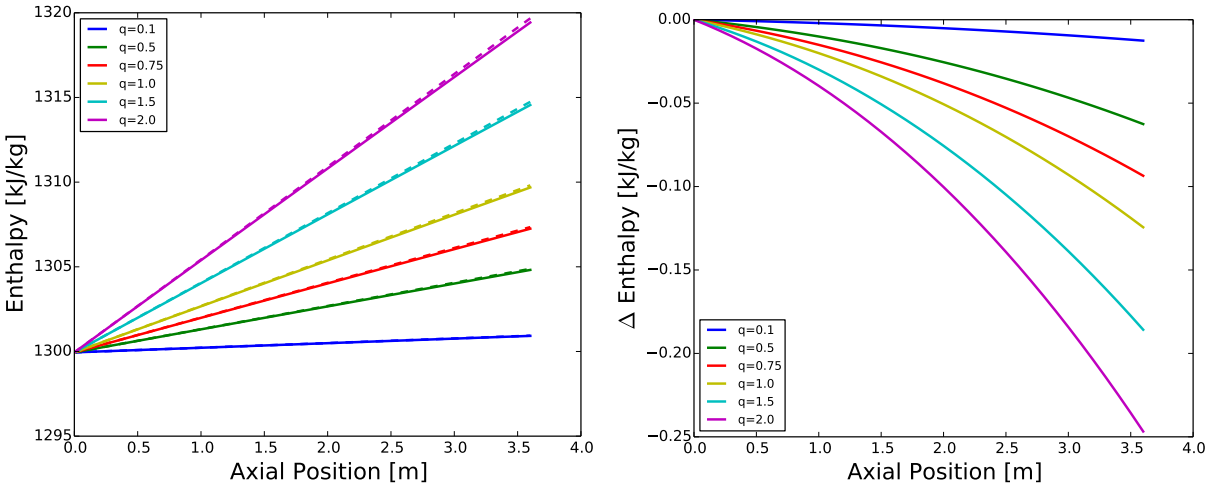

(a) Enthalpy distribution

(b) Comparison of code results with Equation 4.37

Figure 4.5: Constant heat rate defect test results. CTF-R accurately predicts the enthalpy to within $0.25\,kJ/kg$ for these six defect tests for a subchannel at approximately PWR conditions.

$$h(x) = h_{in} + \frac{q'x}{\dot{m}} \tag{4.37}$$

A steady state test problem is analyzed for a variety of linear heat rates. The enthalpy rise in the fluid when modeled in CTF-R is shown in Figure 4.5a. The code and analytical results are compared in Figure 4.5b.

Heat Transfer with Cosine Power Profile

Once the heat transfer is tested with a constant heat rate, it is necessary to also demonstrate that the power profile is properly implemented. This series of defect tests is nearly identical to the tests in the previous section, but with a cosine power distribution. Under this condition, the enthalpy in the channel is calculated using Equation 4.36 with $q'(x) = q'_o \cos(\pi x/L - \pi/2)$.

$$h(x) = h_{in} + \frac{q'_o L}{\pi \dot{m}} \left[1 + \sin\left(\frac{\pi x}{L} - \frac{\pi}{2}\right)\right] \tag{4.38}$$

The CTF-R results for this power distribution are shown in Figure 4.6a for a variety of heat rates. The comparison between the CTF-R and analytical solutions are shown in Figure 4.6b.

Two Channels with Different Areas

To test the lateral momentum equation, two isothermal channels with a gap between them are simulated. The two channels have different areas and the same inlet mass flux. The two channels have different frictional pressure drops, which leads to a lateral pressure difference. The pressure

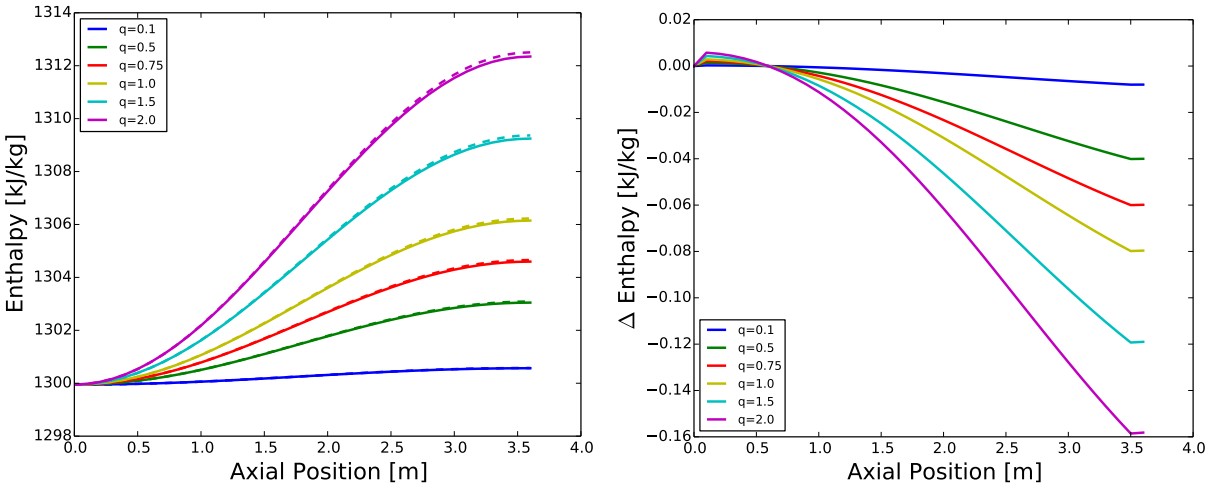

(a) Enthalpy distribution

(b) Comparison of code results with Equation 4.38

Figure 4.6: Cosine heat rate enthalpy defect tests. CTF-R accurately predicts the enthalpy to within $0.16\,kJ/kg$ for these test problems which approximate a PWR subchannel.

distribution in the two channels is allowed to reach steady state, at which point pressure in laterally adjacent cells will equalize and the lateral velocities will reach a steady state value. This problem is essentially equivalent to the flow split problem in the CTF documentation [149].

The two subchannels each have three axial cells with a total flow area equal to $0.003\,m^2$. The results for three different area ratios are plotted in Figure 4.7. As the area ratio increases, the pressure difference between laterally adjacent cells and the steady state value for the lateral velocities both increase.

Two Identical Channels

For these defect tests, the lateral velocity between two identical channels is initialized to a nonzero value. Because the two channels are identical, lateral gradients eventually equalize and the lateral velocities go to zero. The results for these defect tests are shown in Figure 4.8. As the initial velocity increases, the oscillations before steady state are more severe, but the velocity eventually go to zero.

4.4.2 Solution Verification

Only one verification problem is currently used to verify CTF-R. For this isokinetic advection problem, the initial conditions are designed such that the pressure and velocity are constant throughout the domain, then the inlet conditions are allowed to advect through the channel at a constant velocity, u. All closure terms are disabled for these simulations.

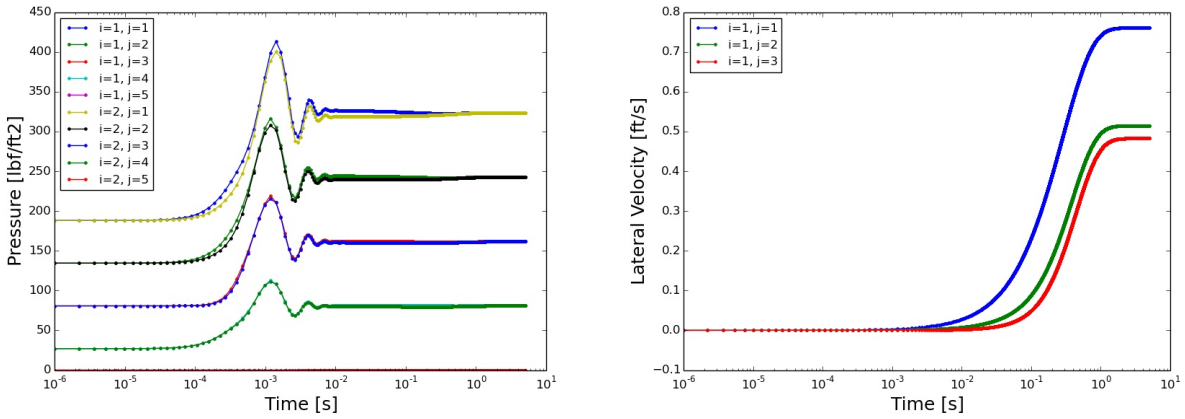

(a) $A_2/A_1 = 1.5$

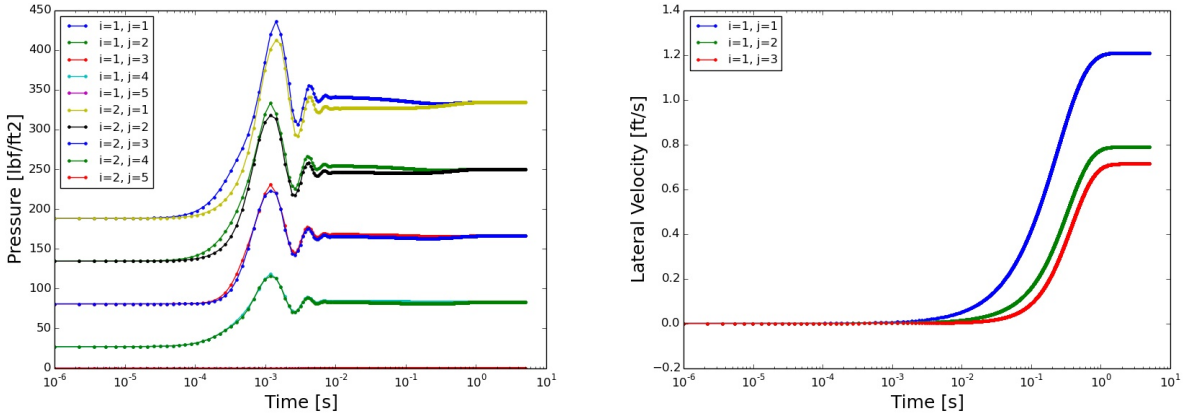

(b) $A_2/A_1 = 2.0$

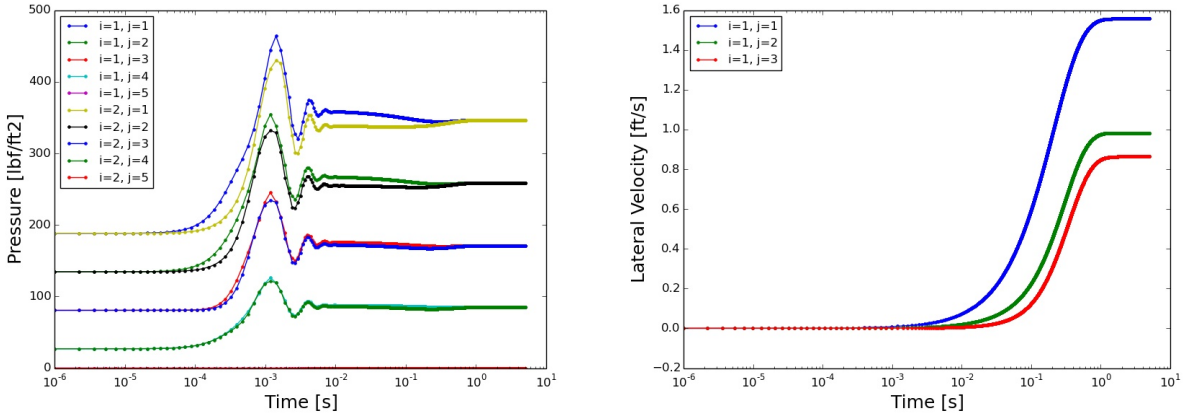

(c) $A_2/A_1 = 2.5$

Figure 4.7: Lateral momentum defect tests with different areas. The pressure (left) and lateral velocity (right) are shown as a function of time. The channel numbers i and axial level j are indicated in the legends, where the two ghost cells are $j = 1$ and $j = 5$. Over time, the lateral pressure gradients go to zero and the lateral velocity approaches a steady state value.

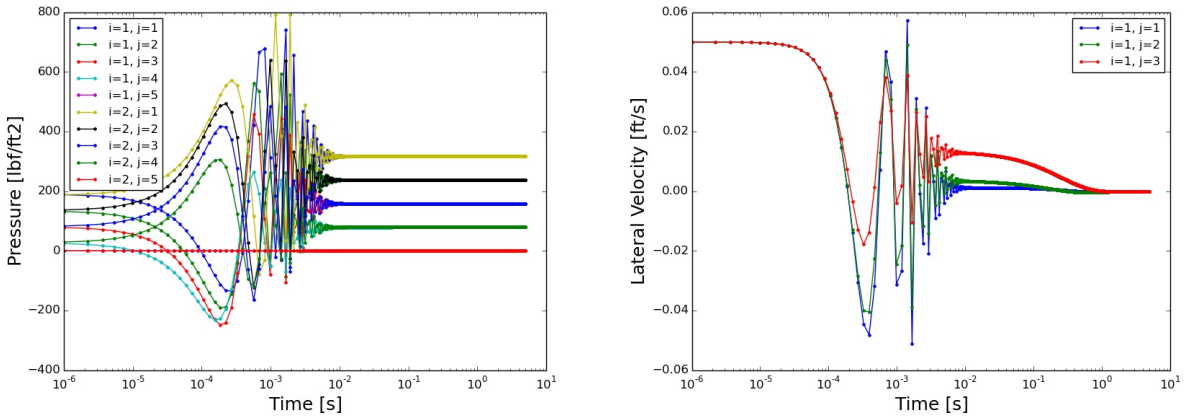

(a) $w_0 = 0.05\, ft/s$

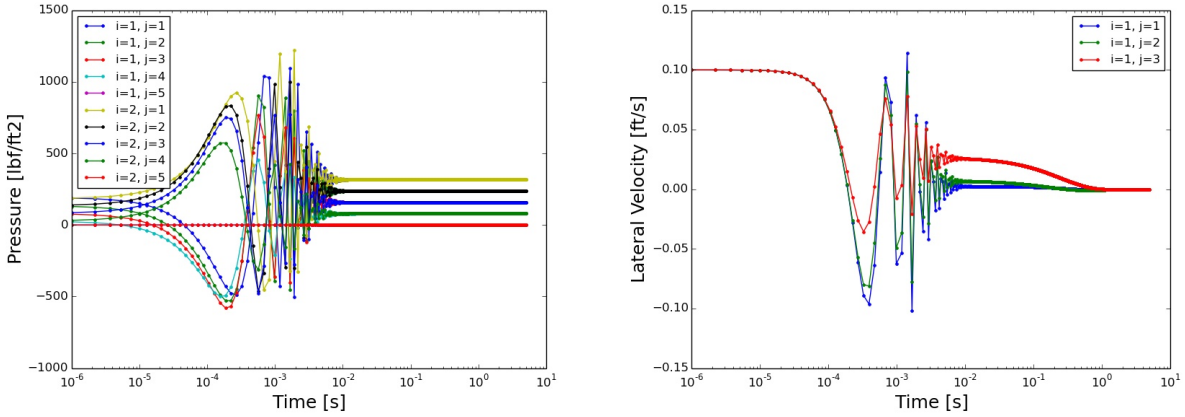

(b) $w_0 = 0.10\, ft/s$

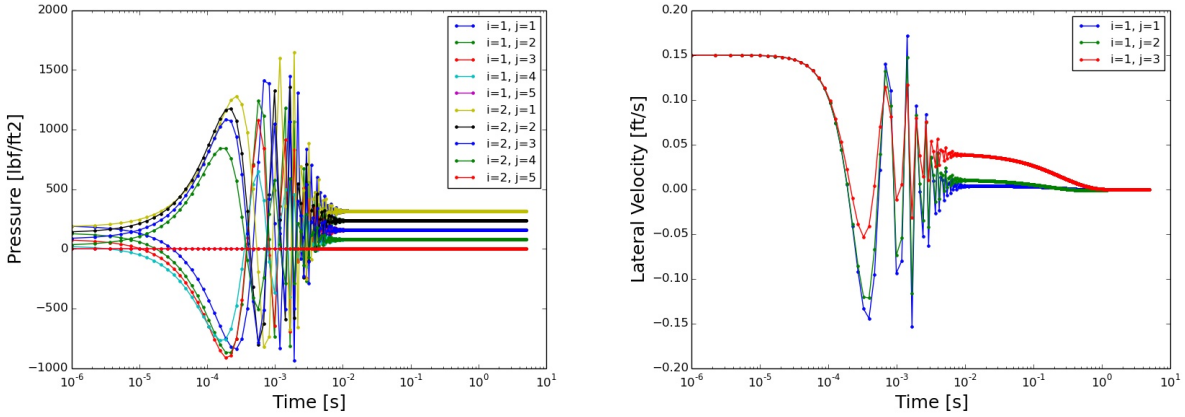

(c) $w_0 = 0.15\, ft/s$

Figure 4.8: Lateral momentum defect tests with equal areas. The pressure (left) and lateral velocity (right) are shown as a function of time. The channel numbers i and axial level j are indicated in the legends, where the two ghost cells are $j = 1$ and $j = 5$. Over time, the lateral pressure gradients go to zero and the lateral velocity approaches zero.

Each of the problems is run for successively refined temporal and spatial meshes. The results are compared using the vector norms defined in Section 3.5. The observed order of accuracy p is determined by finding a line of best fit with the exponential form, $||h|| = cx^p$. Here, $||h||$ is the vector norm, c is some constant, and x is the mesh being refined. The coefficient of determination, R^2, demonstrates how closely the line approximates the results.

Problem Definition

With a constant velocity u_o and constant pressure in single phase with no closures, the conservation equations simplify significantly. The momentum equation becomes trivial, and the mass and energy equations take similar forms.

$$\frac{\partial \rho}{\partial t} + u_o \frac{\partial \rho}{\partial x} = 0 \tag{4.39}$$

$$\frac{\partial \rho h}{\partial t} + u_o \frac{\partial \rho h}{\partial x} = 0 \tag{4.40}$$

The parameters which define the problem are outlined in Table 4.2. The conditions approximate a subchannel with reactor geometry at near standard pressure and temperature. There is a maximum change in temperature of $2°C$. The water is subcooled throughout all simulations. The inlet condition advects to the outlet in about ten seconds. The time of interest for all simulations is when the inlet condition has advected half way through the channel.

Table 4.2: Problem Parameters for Isokinetic Advection

Parameter	Symbol	Value	Units
Channel Length	L	0.5	m
Flow Area	A	0.0001	m^2
Wetted Perimeter	P_w	0.040	m
Pressure	P	1.00	bar
Initial Temperature	T_{out}	40	$°C$
Initial Enthalpy	h_{out}	167.6	kJ/kg
Initial Density	ρ_{out}	992.22	kg/m^3
Initial Flow Rate	$\dot{m}_{out}$	0.005	kg/s
Velocity	u_o	0.05039	m/s
Inlet Temperature	T_{in}	38	$°C$
Inlet Enthalpy	h_{in}	159.22	kJ/kg
Inlet Density	ρ_{in}	992.90	kg/m^3
Inlet Flow Rate	$\dot{m}_{in}$	0.05004	kg/s
Hyperbolic Tangent Width	l	0.05	m
Hyperbolic Tangent Offset	τ	5.0	s
Cosine Wave Period	p	L/u	s

Three inlet condition types are chosen: square wave, hyperbolic tangent, and cosine wave. The square wave is selected for its simplicity; both the inlet condition and the initial condition are constant. For the square wave, solution of Equation 4.40 is a step function.

$$h_{sq} = \begin{cases} h_{out}, & u_o t \leq x \\ h_{in}, & u_o t > x \end{cases} \tag{4.41}$$

The second inlet condition type is the hyperbolic tangent. This condition is selected because, like the square wave condition, it is smooth with the initial condition, but lacks the discontinuity at the wave location.

$$h_{tanh} = \begin{cases} h_{out}, & u_o t \leq x \\ \frac{1}{2}\left[(h_{out} + h_{in}) - (h_{out} - h_{in}) \tanh\left(\frac{u_o(t-\tau)-x}{l}\right)\right], & u_o t > x \end{cases} \tag{4.42}$$

A characteristic length, l, determines how wide the hyperbolic tangent is. The constant τ is necessary to shift the wave left, which allows the inlet and initial condition to be approximately equal at the beginning of the simulation. When using the hyperbolic tangent inlet condition, the time of interest for all simulations will be at five seconds plus the offset.

The final inlet condition type is a cosine wave. The cosine is selected such that it is continuous with the initial condition.

$$h_{cos} = \begin{cases} h_{out}, & u_o t \leq x \\ \frac{1}{2}\left[(h_{out} + h_{in}) + (h_{out} - h_{in}) \cos\left(\frac{2\pi}{p}\left(t - \frac{x}{u_o}\right)\right)\right], & u_o t > x \end{cases} \tag{4.43}$$

The cosine period, p, is equal to the channel length divided by the velocity, u. Therefore, the wavelength is equal to the channel length.

To ensure that all derivatives of the solution are smooth, the initial condition should also be a cosine shape. CTF input does not allow for nonuniform initial conditions, so there may be a small amount of error that originates from the discontinuous second derivative at the wave location.

Modified Equation Analysis

MEA [65] is used to define the formal order of accuracy by estimating the truncation error of a given discretization scheme. The analysis starts with a discretized form of Equation 4.39 with a constant positive velocity and upwinded advection term.

$$\frac{\rho_i^{n+1} - \rho_i^n}{\Delta t} + u_o \frac{\rho_i^n - \rho_{i-1}^n}{\Delta x} = 0 \tag{4.44}$$

Second order Taylor series expansions about i and n are used to approximate ρ_i^{n+1} and ρ_{i-1}^n.

$$\rho_i^{n+1} = \rho_i^n + \left.\frac{\partial \rho}{\partial t}\right|_i^n \Delta t + \frac{1}{2}\left.\frac{\partial^2 \rho}{\partial t^2}\right|_i^n \Delta t^2 + \mathcal{O}\left(\Delta t^3\right) \tag{4.45}$$

$$\rho_{i-1}^n = \rho_i^n - \left.\frac{\partial \rho}{\partial x}\right|_i^n \Delta x + \frac{1}{2}\left.\frac{\partial^2 \rho}{\partial x^2}\right|_i^n \Delta x^2 + \mathcal{O}\left(\Delta x^3\right) \tag{4.46}$$

Equations 4.44, 4.45, and 4.46 are combined and rearranged with the original conservation equation on the left and the error terms on the right.

$$\frac{\partial \rho}{\partial t} + u_o \frac{\partial \rho}{\partial x} = \left[\frac{u_o}{2}\frac{\partial^2 \rho}{\partial x^2}\right]\Delta x - \left[\frac{1}{2}\frac{\partial^2 \rho}{\partial t^2}\right]\Delta t \tag{4.47}$$

This defines the general behavior of error in CTF. The formal order of accuracy is first order in both space and time when the higher order terms are sufficiently small that they can be neglected. The selection of suitable Δx and Δt combinations is an important part of the convergence study process. The solution must be stable, while also having a feasible computational time. Equation 4.47 can be used to derive the CFL, which directly determines the stability of the single-phase solutions in this work.

Equation 4.6 is used to find a relationship between the second derivative with respect to space and the second derivative with respect to time, $\left(\partial^2\rho/\partial t^2\right) = u^2\left(\partial^2\rho/\partial x^2\right)$. This result is combined with Equation 4.47 to derive a stability criterion.

$$\frac{\partial \rho}{\partial t} + u_o \frac{\partial \rho}{\partial x} = \frac{u_o \Delta x}{2}\frac{\partial^2 \rho}{\partial x^2}\left(1 - \text{CFL}\right) \tag{4.48}$$

The CFL is defined as $u_o \Delta t/\Delta x$. When the CFL is less than one, the error term causes diffusion. When the CFL number is larger than one, the diffusion term becomes an anti-diffusion operator and the solution is unstable. The CFL is below 1.0 for all simulations in this work.

Square Wave Advection Results

Typical enthalpies for the square wave advection problem are shown in Figure 4.9a. The results are compared to Equation 4.41, which is represented as dashed lines in the figure. The difference between the analytical and code results are shown in Figure 4.9b. CTF-R predicts the solution well, with characteristic diffusion around the discontinuity.

A temporal order of accuracy study is performed and the results are shown in Figure 4.10. Three norms—L_1, L_2, and L_∞—are shown along with the lines of best fit with corresponding R^2 values. See Section 3.5 for the definition of these norms. The resulting order of accuracy is essentially one for both codes.

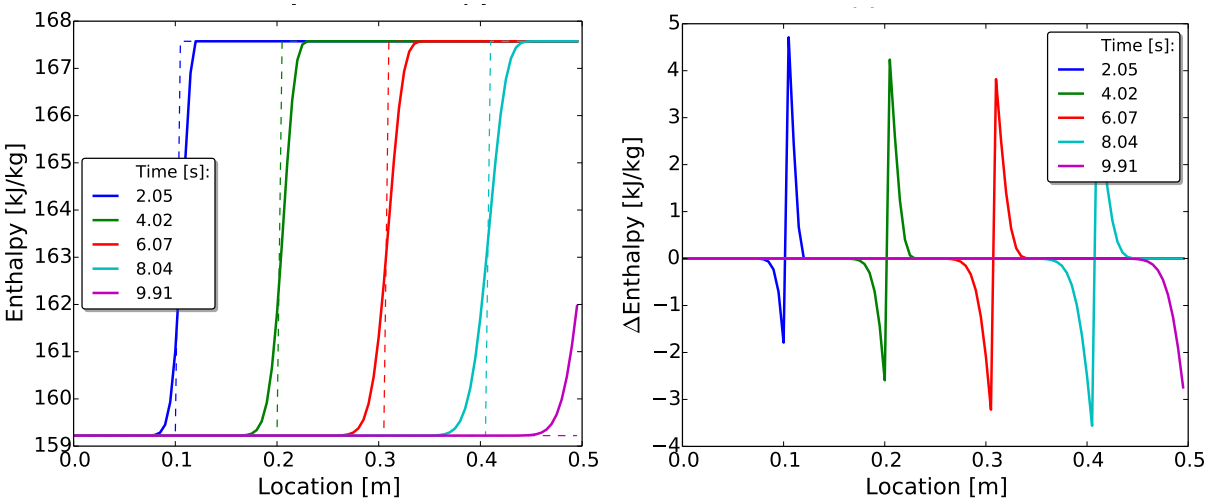

(a) Code results and analytical solutions

(b) Error $h_{sq} - h_{code}$

Figure 4.9: Square wave advection results. Enthalpy is plotted for an example square wave advection run with $\Delta x = 0.05\,m$, $\Delta t = 0.0893\,s$, and CFL $= 0.9$.

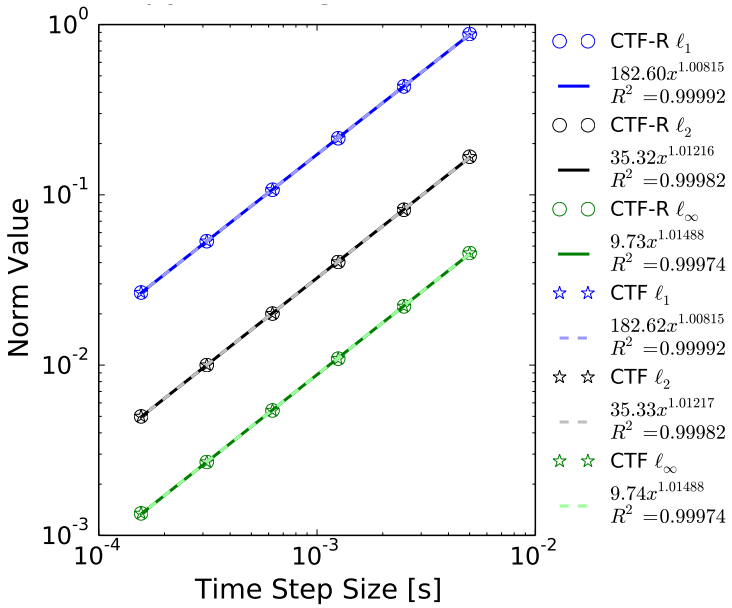

Figure 4.10: Square wave temporal convergence study. The axial spacing is held constant at $\Delta x = 6.25 \times 10^{-3}\,m$ while the time step size is refined by factors of two.

Hyperbolic Tangent Advection Results

Results for the hyperbolic tangent inlet condition are shown in Figure 4.11. Similar to the square wave results, Figure 4.11a shows the code results and analytical solution, and Figure 4.11b is the difference between the two. The offset of the wave, τ, is sufficiently large that the solution is smooth. The error follows the wave location and again shows the expected diffusion behavior.

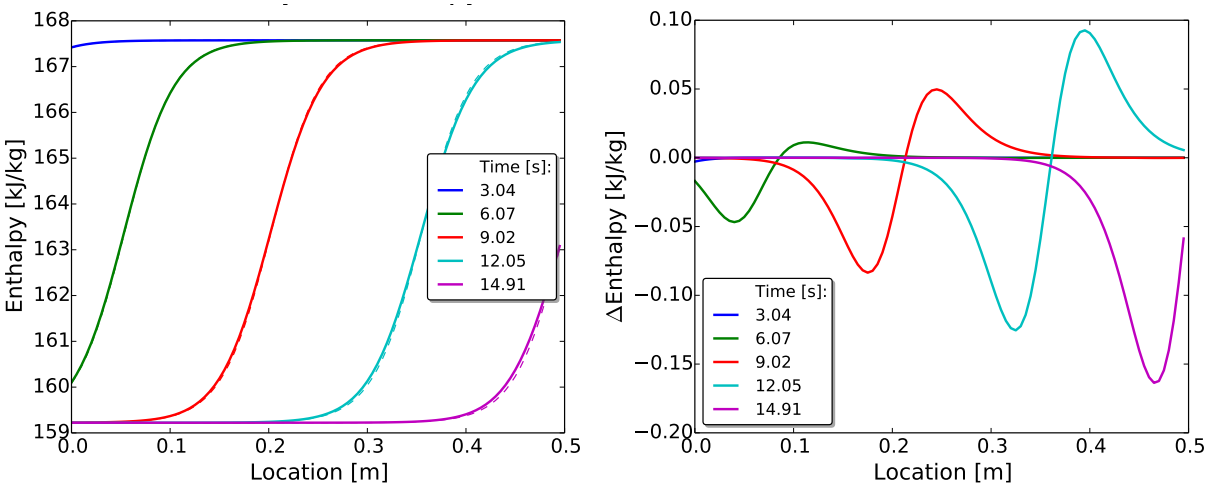

(a) Code results and analytical solutions

(b) Error $h_{tanh} - h_{code}$

Figure 4.11: Hyperbolic tangent wave advection results. Enthalpy is plotted for an example hyperbolic tangent advection run with $\Delta x = 0.05\,m$, $\Delta t = 0.0893\,s$, and CFL $= 0.9$.

Temporal, spatial, and constant CFL convergence studies were performed with the hyperbolic tangent condition and the results are shown in Figures 4.12a, 4.12b, and 4.12c, respectively. All three studies have observed orders of accuracy approximately equal to one.

Cosine Wave Advection Results

Typical results for the cosine advection problem are shown in Figure 4.13a, and the difference between the code and analytical solution are shown in Figure 4.13b. Again, the CTF results are solid and the analytical solution is dashed. The code results match well with the analytical solution.

Finally, the cosine wave isokinetic advection test problem is used to perform three convergence studies. The results are shown in Figures 4.14a, 4.14b, and 4.14c. All observed orders of accuracy are near unity, which demonstrates that the codes are first order in both space and time.

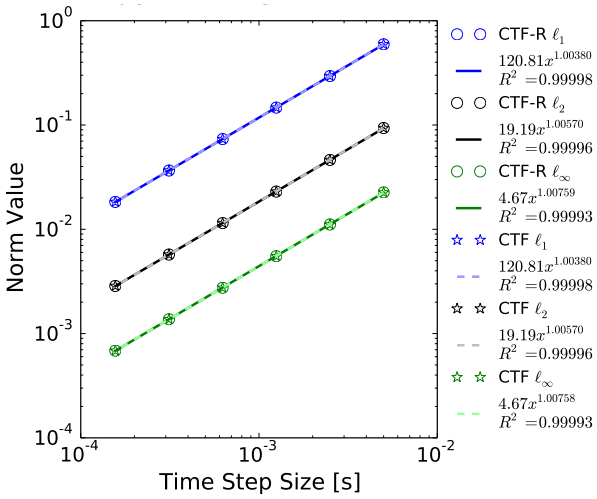

(a) Temporal convergence with $\Delta x = 6.25 \times 10^{-3}\, m$

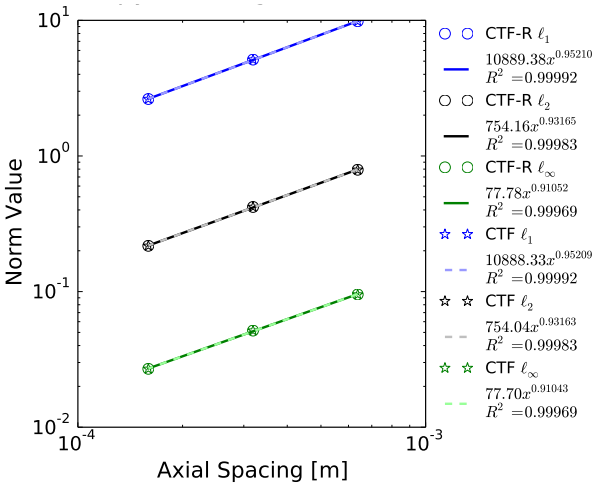

(b) Spatial convergence with $\Delta t = 3 \times 10^{-3}\, s$

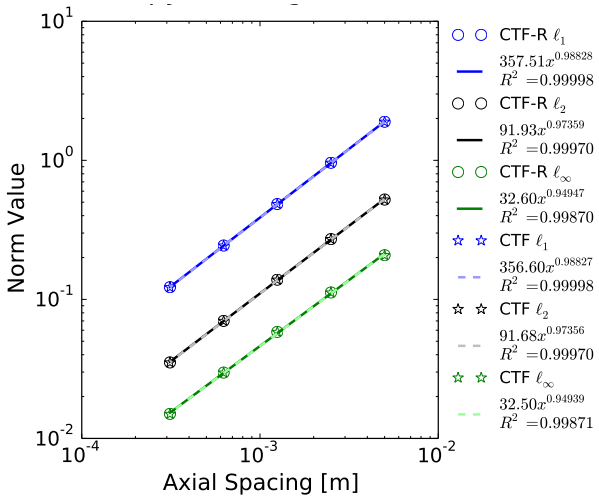

(c) CFL convergence with CFL = 0.9

Figure 4.12: Hyperbolic tangent wave convergence studies. Each study holds Δx, Δt, or CFL constant while refining the mesh. All results are approximately first order.

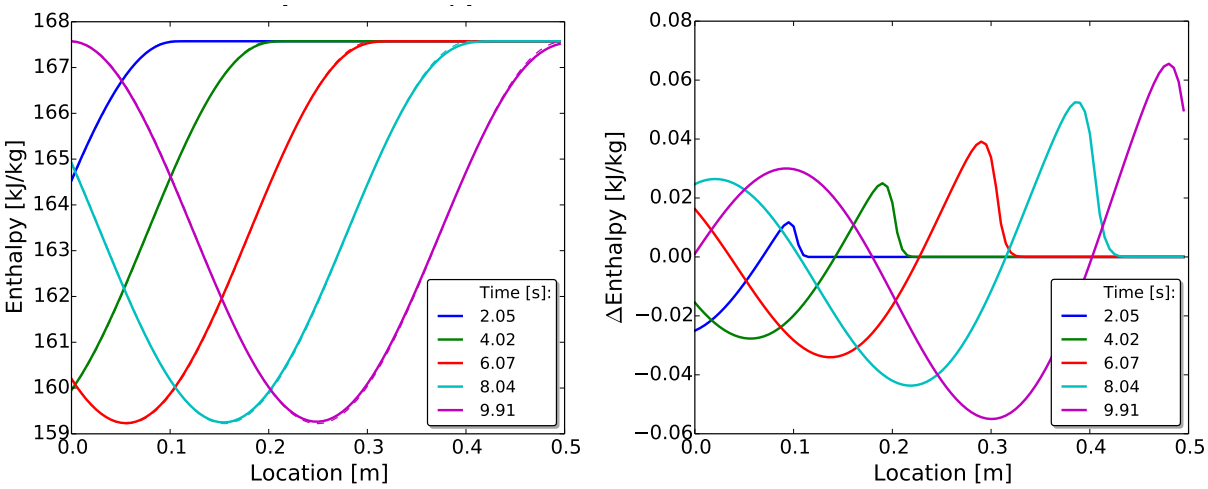

(a) Code results and analytical solutions

(b) Error $h_{cos} - h_{code}$

Figure 4.13: Cosine wave advection results. The enthalpy is plotted for a cosine advection run with $\Delta x = 0.05\,m$, $\Delta t = 0.0893\,s$, and CFL $= 0.9$.

Table 4.3: Summary of observed orders of accuracy. The ℓ_2 norm for each boundary condition and convergence type are shown. All results are approximately one.

Boundary	Type	CTF-R	CTF
square	Δt	1.012	1.012
tanh	Δt	1.006	1.006
	Δx	0.932	0.932
	CFL	0.974	0.974
cos	Δt	1.002	1.002
	Δx	0.951	0.951
	CFL	0.993	0.993

Conclusions

All observed orders of accuracy are summarized in Table C.1.

It has been shown that the formal order of accuracy and the observed order match for both CTF and CTF-R when using an isokinetic advection test problem. Small variations can be attributed to a variety of sources, but the differences are sufficiently small to conclude that the code is overall first order. Therefore, the solution algorithms for both codes have been implemented correctly. For further discussion, refer to [30, 32, 132, 136, 149].

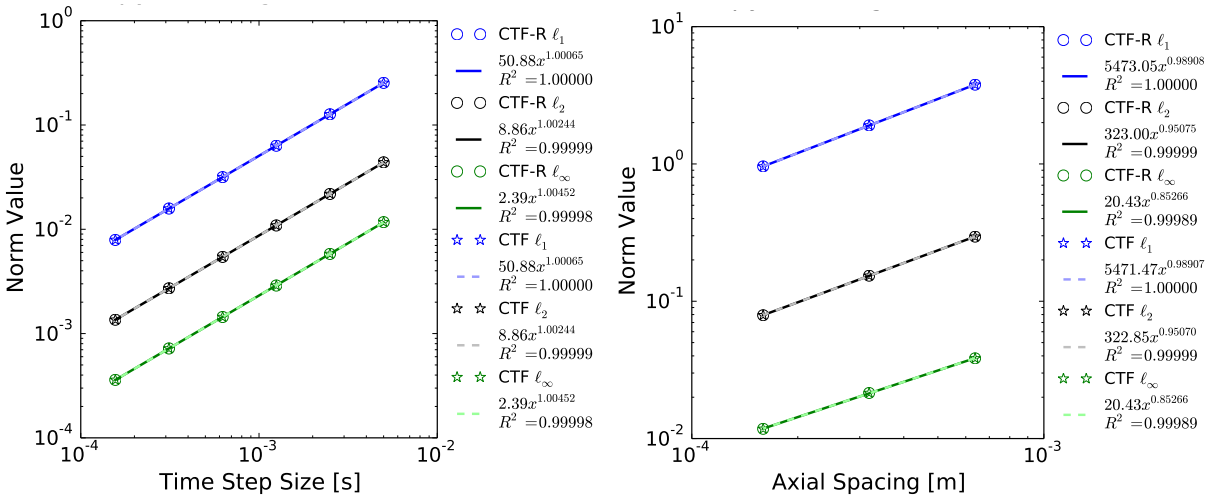

(a) Temporal convergence with $\Delta x = 6.25 \times 10^{-3}\, m$ (b) Spatial convergence with $\Delta t = 3 \times 10^{-3}\, s$

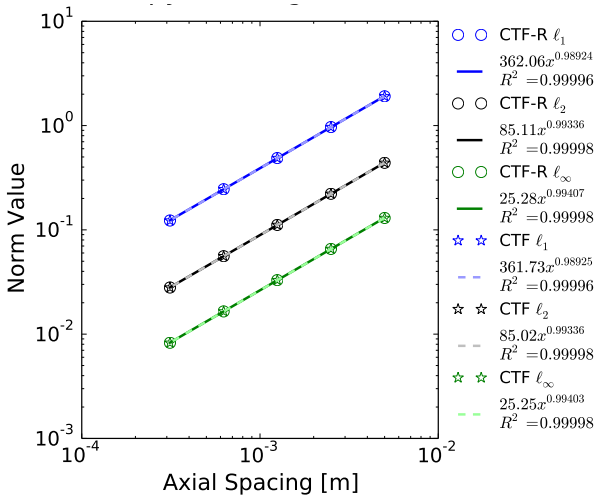

(c) CFL convergence with CFL = 0.9

Figure 4.14: Cosine wave convergence studies. Each study holds Δx, Δt, or CFL constant while refining the mesh. All results are approximately first order.

4.4.3 Validation

The current validation of CTF-R includes only a separate effects study of the frictional pressure drop, which is outlined in this section. This analysis has already been performed for the main version of CTF and incorporated into the Validation Manual [149], and the same input decks are used for this study.

Friction

All friction validation is for single phase flow through horizontal isothermal pipes with circular cross sections. In these studies, the geometry is defined by pipe diameter D and total length L. The boundary conditions are inlet velocity v_{in}, inlet temperature T_{in}, and outlet pressure $P_{out} = P_{atm}$. The pressure drop in the pipe is measured between two locations, P_1 and P_2, which are a defined distance from each end of the pipe. The geometry is shown schematically in Figure 4.15.

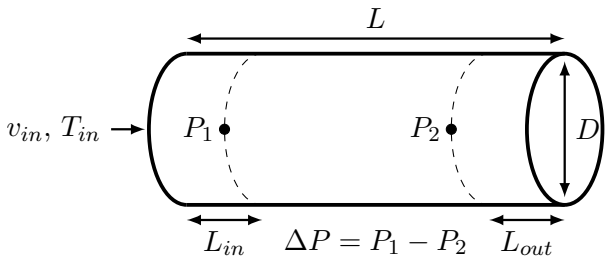

Figure 4.15: Geometry of friction validation experiments. Each case models isothermal horizontal single phase flow through a pipe.

The first set of experiments are taken from the smooth and rough pipe data of Nikuradse [118, 119]. Of the 487 tests run by Nikuradse, 398 are selected for this validation study. The results are shown in Figures 4.16a and 4.16b for the smooth and rough data, respectively. The second set of data is taken from the experiments of Furuichi et al. [46]. These were performed at a higher pressure than Nikuradse's, but all pipes were smooth. The results are outlined in Figure 4.17.

The RMS between the experimental pressure drops and the code results are summarized in Table 4.4 for each friction factor option and each experimental setup. The second option is the least accurate, especially for the rough data. This is because these friction factor options do not include any effect for roughness. The second two options, which were recently implemented [163], are much more accurate.

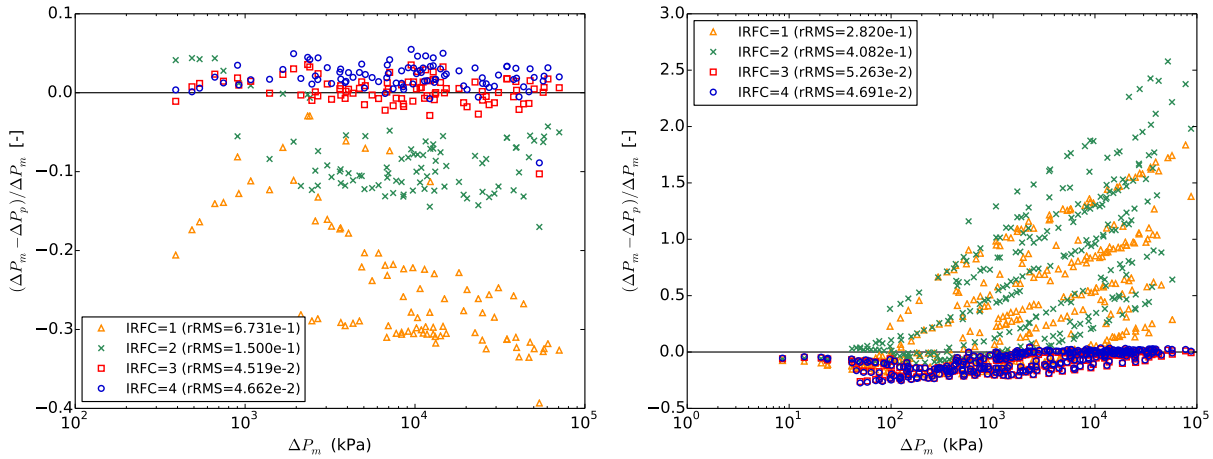

(a) Smooth pipe (b) Rough pipe

Figure 4.16: Nikuradse pressure drop validation results. Both smooth pipe and rough pipe results are plotted for all four friction factor correlations. The rRMS for each option is summarized in the legend. The first two options are inaccurate for the rough pipe data, since they do not account for the effect of pipe roughness.

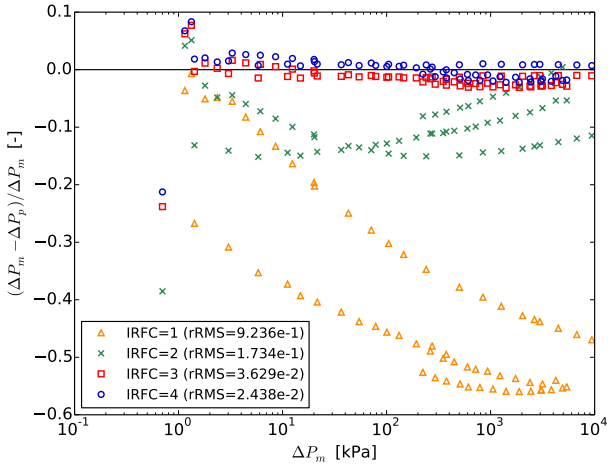

Figure 4.17: Furuichi pressure drop validation results. The first two options are relatively inaccurate, with the second two matching the data extremely well.

Table 4.4: Summary of rRMSs for separate effects friction validation. The friction factor options corresponds to the correlations in Section 4.2.8, which are determined by the user input `IRFC`. For all cases, options 3 and 4 yield better results than the other two.

`IRFC`	Nikuradse Smooth	Nikuradse Rough	Furuichi
1	0.673	0.282	0.924
2	0.150	0.408	0.173
3	0.0452	0.0526	0.0363
4	0.0466	0.0469	0.0244

4.4.4 Regression Tests

A subset of the defect tests discussed in the previous sections have been selected as regression tests. All of these are incorporated into the automated CTF test matrix. These tests are summarized in Table 4.5. All tests are run by invoking the command `ctest -R res` in the CTF build directory.

4.5 Discussion

This chapter has demonstrated the theory, conservation equations, implementation, and V&V of a novel residual-based version of CTF. The residual form is capable of modeling single phase flow through rod-centered subchannels with nuclear fuel rods, friction, heat transfer, and lateral flow. Each of these capabilities have associated defect tests, though there are some features that remain to be tested.

- No test problems have been designed where an azimuthal rod fraction is connected to a channel. This would test that the azimuthal fraction is implemented correctly in the conservation equations and would be necessary for channel-centered control volumes.
- The temperature dependence of the fuel thermal conductivity has not been tested. In order to thoroughly test the conduction ;resistance analogy, a conduction solution defect test with temperature-dependent conductivities should be implemented. For example, if the thermal conductivity is linear $k = C_1 + C_2 T$, the steady state conduction equation in cylindrical coordinates can be solved analytically.

$$C_1(T_i - T_o) + \frac{C_2}{2}(T_i^2 - T_o^2) = \frac{q''' r^2}{4} \tag{4.49}$$

- A channel with reverse flow should be tested to ensure that axial upwinding terms are properly implemented.

Table 4.5: CTF-R regression tests. Each of the 21 regression tests are listed here with their name, the model that is tested, and general notes about the test. Each test corresponds to a defect test that was discussed earlier in this chapter.

Name	Model	Notes
square	Isokinetic advection	square wave
cosine		cosine wave
tanh		tanh wave
fric_g0_f001	Friction	$f = 0.01$, $g = 0$
firc_g0_f005		$f = 0.005$, $g = 0$
fric_g0_f01		$f = 0.01$, $g = 0$
fric_g1_f001		$f = 0.001$, $g = 9.81$
firc_g1_f005		$f = 0.005$, $g = 9.81$
fric_g1_f01		$f = 0.01$, $g = 9.81$
friction_1	Friction correlation	`IRFC`= 1
friction_2		`IRFC`= 2
friction_3		`IRFC`= 3
friction_4		`IRFC`= 4
ht1	Heat transfer	$q' = 0.1$, constant
ht2		$q' = 2.0$, constant
ht3		$q' = 0.1$, cosine
ht4		$q' = 2.0$, cosine
cond1	Conduction solution	$k_f = 20$, $k_c = 10$
cond2		$k_f = 15$, $k_c = 8$
lat1	Lateral momentum	$A_r = 2.0$, $w_o = 0.0$
lat2		$A_r = 1.0$, $w_o = 0.5$

- Negative lateral flows must be tested to verify that the lateral momentum equation properly incorporates channel indeces.
- Though each code capability is tested individually, the code lacks defect tests that incorporate combinations of models. For example, there is no test which includes both lateral transfer and fuel rods.
- Convergence studies should be designed and implemented for the momentum equations and the conduction solution.

Once all existing capabilities are fully tested, there are four tasks which should be performed for CTF-R to make it more robust.

1. The Jacobian matrix is dimensional, which means that different rows can vary many orders of magnitude. To resolve numerical issues, the Jacobian matrix can be nondimensionalized

in one of two ways. The first option is to multiply each conservation equation by some representative values. For example, the mass equation would become

$$\frac{\tau}{\rho_o}\left[\frac{\partial \rho}{\partial t}+\frac{\partial \rho u}{\partial x}+\frac{\partial \rho w}{\partial z}-\kappa_1\frac{\partial^2 \rho}{\partial z^2}\right]=0. \tag{4.50}$$

The second option for nondimensionalizing the Jacobian is to simply multiply each row by a constant. These constants will be selected such that each row of the Jacobian has values of similar magnitudes.

2. The PETSc tolerances used to solve the Jacobian should be re-examined. Currently, these values are input by the user because they are strongly problem-dependent. By nondimensionalizing the Jacobian, these tolerances should be more universal.
3. The CTF-R algorithm currently uses CTF convergence criterion for the steady state solution. Instead, the convergence should be based on a norm of the residuals over the entire system. This will require three tolerances: (1) the relative value of the residuals, (2) the absolute value of the residuals, and (3) the change in residuals between successive iterations. This capability is partially implemented, but not currently used.
4. Finally, the nonlinear iteration should be finalized and tested. The basic structures and algorithm for a CTF-R nonlinear iteration are already in place, but the algorithm is thus far unused and untested. With a nonlinear iteration, the code will be much more stable as more implicitness is added to the conservation equations.

Though CTF-R provides a much more flexible tool, it lacks many of the features already included in the CASL version of CTF. Much of the future work for CTF-R will include the implementation of these capabilities.

- CTF-R is currently single phase, a large amount of work will be required to transition to two phase modeling.
- Only nuclear fuel rods are modeled in CTF-R, other solid components will need to be implemented for reactor geometries.
- Azimuthal and axial transfer should be added to the conduction equation.
- The CTF and CTF-R turbulent mixing and lateral friction models are currently inconsistent. The turbulent friction coefficients—κ_1, κ_2, and κ_3—are currently tunable parameters in CTF-R.
- CTF has the capability to model sections, which are axial lengths of a reactor that have significantly different geometries. For example, these can be used to model partial-length rods in Boiling Water Reactors (BWRs). This capability is not yet implemented in CTF-R.
- Tables for temporal or spatial variation of geometry are not read by CTF-R.

- CTF-R is only capable of modeling the typical boundary conditions for a reactor: inlet temperature and velocity with outlet pressure. CTF has other options which should be implemented.
- CTF-R uses the same output files as CTF, but not all state variables have been consistently updated in these outputs. Fuel temperature and lateral flow quantities need to be pushed to the CTF working arrays.
- CTF-R does not track boron or model noncondensible gases.
- CTF-R does not have a restart capability.
- Error checking in CTF-R needs to be expanded.

CTF-R run times are currently longer than corresponding CTF run times for the same problem. For example, the run times for the cosine wave spatial convergence study corresponding to Figure 4.14b are shown in Figure 4.18. The CTF-R run times scale poorly as the mesh is refined because the full Jacobian matrix is solved in PETSc, which takes much longer. If N is the number of fluid cells, then the CTF matrix is $N \times N$ and the CTF-R matrix is $3N \times 3N$. In the future, this will be resolved by increasing the implicitness of the solution algorithm, using Jacobian preconditioning, and using Jacobian-free solution algorithms.

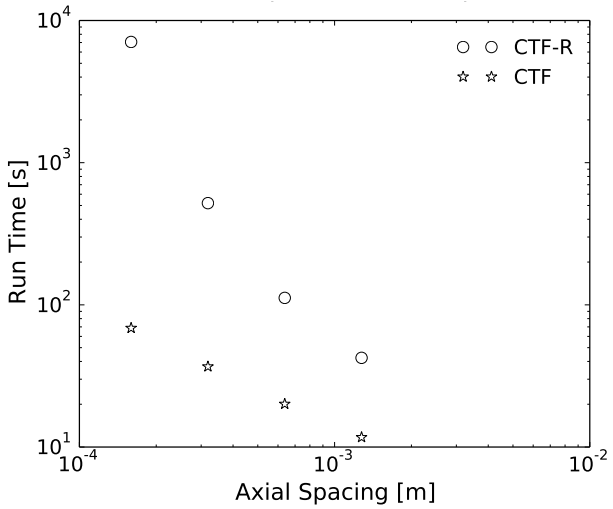

Figure 4.18: Run times for cosine verification simulations. The run times for four problems with $\Delta t = 0.003$ and different spatial meshes are shown for both CTF and CTF-R.

As a new code, CTF-R is not restricted to particular conservation equations, discretizations, or solution algorithms. There are a few particular applications that represent interesting future work.

- Next generation reactors will be much easier to model. For example, liquid sodium and liquid metal reactors will require that a conduction term is added to the liquid energy equation. This is not possible in the main version of CTF, but would be trivial in CTF.
- It would be possible to add multi-physics conservation equations to the Jacobian. This could include coupling to residual-based nuclear physics or fuel rod modeling codes. An implicit coupling method could be used by including off-diagonal terms in the combined Jacobian.
- CTF-R can solve the steady state conservation equations by simply eliminating the temporal terms. This would require significant effort to develop an algorithm which sets an initial condition which is sufficiently close to the steady state solution.

CTF-R has been developed as a flexible solver through general data structures and a numerical construction of the Jacobian and it was designed with VVUQ explicitly in mind. Given it's current modeling capabilities and future potential, CTF-R will be an important development step in the history of COBRA codes.

CHAPTER

5

CORRELATION CALIBRATION

As part of CTF-R development, each empirical model is provided with suggested parameter distributions for use in uncertainty analyses. These parameter distributions are based purely on experimental data, so they will be an improvement over "expert opinion" distributions that are commonly employed in UQ studies (see [134] for an example of traditional UQ methods). The experimental data can be included in the code distribution and additional data may be appended in the future. With better experimental data, the parameter estimates will be more accurate.

The parameter estimation framework used in this chapter incorporates both frequentist and Bayesian calibration methods. Most analyses are performed using a fixed effects statistical model, though an initial mixed-effects analysis is used to motivate future work. Each correlation is individually calibrated multiple times to ensure that a suitable statistical model is used. The same process is followed for each correlation.

- The correlation purpose, origin, and inherent assumptions are outlined and discussed.
- A specific correlation is chosen for calibration that is continuous, smooth, relatively accurate, and has reasonable derivatives with respect to all parameters.
- An extensive set of experimental data is gathered to be used in the calibration.
- An identifiability analysis is performed and used to eliminate any unidentifiable parameters. The algorithm outlined in Section 3.8 is used for this step, where the least identifiable parameters are successively fixed until all calibration methods run without errors.

- The empirical model is calibrated to the experimental data using three fixed effects statistical frameworks.
  1. Algorithm 3.1: OLS asymptotic minimization.
  2. Algorithm 3.2: a statistical bootstrapping method with 10^4 samples.
  3. Algorithm 3.3: the DRAM algorithm with uninformative priors, a Gaussian likelihood function, OLS estimates as initial values, 10^5 burnin samples, and 10^4 samples.
- A mixed-effects MLE algorithm implemented in MATLAB©, `nlmefit`, is employed to demonstrate which datasets would be more accurately modeled using a mixed-effects statistical model.
- Final remarks are made, including suggestions for parameter distributions, possible improvements to the model, and future work.

Four CTF-R empirical correlations are considered in this chapter: friction factor, heat transfer coefficient, fuel thermal conductivity, and cladding thermal conductivity. This covers all correlations that are currently implemented in the code.

5.1 Single-Phase Wall Friction

Pressure drop due to wall friction is calculated by integrating wall shear stress: $\tau_w = \mu \left(\partial u/\partial y\right)_w$, but the derivative of velocity is difficult to predict near walls so it is nondimensionalized.

$$f = \frac{8\tau_w}{\rho u^2} \tag{5.1}$$

Here, f is the Darcy friction factor, ρ is density, and u is mean flow velocity. The friction factor is determined empirically and related to pressure drop with the Darcy-Weisbach equation.

$$\Delta P = fL\frac{\rho u^2}{2D_h} \tag{5.2}$$

The length of a pipe is L and the hydraulic diameter is D_h. In the most general sense, friction factor is a function of Reynolds number, pipe roughness, Grashof number, and geometry. In most engineering applications, the effects of natural circulation and entrance effects are neglected. In addition, correlations for circular pipes are commonly applied to all geometries, where the hydraulic diameter is used $D_h = 4A/P$. Here, A is flow area and P is the wetted perimeter. This approach is generally accepted in nuclear engineering applications, even though it can result in errors as large as 23% [43].

Many pipe friction factor correlations exist throughout the literature, and most are based on the graphical representation of Moody [109]. For laminar flow of incompressible Newtonian

fluids through circular pipes, the friction factor can be analytically derived [131].

$$f_{lam} = \frac{64}{Re} \tag{5.3}$$

In the transitional and turbulent regimes, however, the friction factor must be approximated. Examples of commonly used correlations are those from McAdams [83, 103], Churchill [24], and Zigrang [179]. Here we use a correlation which is a logarithmic combination of correlations for turbulent flow through smooth pipes and flow through fully rough pipes [23].

$$f_{turb} = 8\left[2.457\ln\left(\frac{1}{(7/Re)^{0.9} + 0.27\epsilon/D}\right)\right]^{-2} \tag{5.4}$$

The laminar and turbulent correlations are combined using a smooth sigmoid function.

$$S = \frac{1}{1 + e^{-a(x-b)}} \tag{5.5}$$

Here, a and b are sigmoid parameters which determine how quickly the sigmoid transitions from $y = 0$ to $y = 1$ and at what x-value the transition takes place. The sigmoid function is plotted in Figure 5.1 with $a = 1$ and $b = 0$.

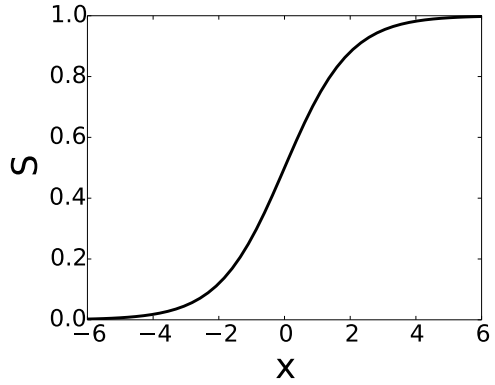

Figure 5.1: Sigmoid function. A sigmoid is any function which transitions smoothly from $y = 0$ to $y = 1$. The sigmoid used to smooth the friction factor is shown here with $a = 1$ and $b = 0$.

The laminar and smooth parts of the equation are combined such that $f = (1-S)f_{lam} + Sf_{turb}$. The sigmoid parameters are given initial values $a = 0.005$ and $b = 2500$.

$$\begin{aligned} f = &\left(1 - \frac{1}{1 + e^{-0.005(Re-2500)}}\right)\frac{64}{Re} \\ &+ \left(\frac{1}{1 + e^{-0.005(Re-2500)}}\right) 8\left[2.457\ln\left(\frac{1}{(7/Re)^{0.9} + 0.27\epsilon/D}\right)\right]^{-2} \end{aligned} \tag{5.6}$$

This new correlation is continuous and smooth and has reasonable derivatives of the friction factor throughout the entire parameter space. The correlation is parameterized with $\boldsymbol{\theta} = [\theta_1, \theta_2, \theta_3, \theta_4, \theta_5, \theta_6]$.

$$f = \left(1 - \frac{1}{1 + e^{-\theta_1(Re-\theta_2)}}\right)\frac{64}{Re} + \left(\frac{1}{1 + e^{-\theta_1(Re-\theta_2)}}\right) 8 \left[\theta_3 \ln\left(\frac{1}{(\theta_4/Re)^{\theta_5} + \theta_6 \epsilon/D}\right)\right]^{-2} \tag{5.7}$$

Because the laminar parameter is derived analytically, it is not treated as uncertain. Instead, its application outside of the conditions for which it was derived is accounted for by additional model error in the model uncertainty, ε (defined in Equation 3.7).

Experimental data for isothermal flow through smooth and rough circular pipes is gathered from 24 different experimentalists. In general, these experiments consist of a long horizontal tube through which the working fluid flows. After steady state is reached, the pressure differential between two points in the pipe is measured. This pressure drop is used with the Darcy-Weisbach equation to calculate the friction factor. The experiments with rough pipes are generally performed using "artificial roughness", where the experimentalist adheres sand or some other small particles to the interior of the pipe. In total, there are 2,194 data points over a large range of Reynolds numbers and pipe roughnesses. All data sources are listed chronologically in Table 5.1 and the data is plotted in Figure 5.2.

An identifiability analysis is applied to the model. After the QR decomposition, the diagonal elements of the matrix Q are $[-261, -0.00476, 3.56, -0.242, 67.9, -45.7]$. Additionally, the sensitivity matrix is not rank deficient, so all six parameters are identifiable.

A statistical fixed effects model is formulated using Equation 3.7, where $f(x, \boldsymbol{\theta})$ is determined according to Equation 5.7 with state points Re and ϵ/D. An initial OLS calibration is performed and the residuals are shown in Figure 5.3. The shape of the residuals indicates that the observational error is dependent upon a state variable, and therefore it is heteroskedastic. Therefore, the original data and the model are log-transformed such that $y = \ln(f)$ instead of $y = f$.

$$\ln y = \ln\left(f(x, \boldsymbol{\theta})\right) + \varepsilon \tag{5.8}$$

An alternative to transforming the data in this way would be to formulate an error model such that the error scales with model values.

$$y = f(x, \boldsymbol{\theta})(1 + \varepsilon) \tag{5.9}$$

This method is not possible using the current coding implementation, so the data is transformed according to Equation 5.8 instead. With the transformed model, the residuals are still not iid, but they are much more reasonable. This is shown in Figure 5.4.

Table 5.1: Data sources for single-phase wall friction. Sources of data are listed chronologically with the pipe material, working fluid, and number of data points extracted.

Year	Author	Ref.	Pipe	Fluid	Data points
1886	Smith	[83]	iron	water	13
1909	Schoder	[83]	iron	water	32
1909	Eberle	[83]	iron	steam	13
1914	Gibson	[83]	copper	water	15
1914	Stanton & Pannell	[158]	brass	water, air	312
1918	Greve	[83]	plastic	black water	42
1920	Scobey	[26]	concrete	air	5
1922	Corp & Ruble	[83]	iron	water	58
1923	Francis	[83]	iron	water	57
1923	Freeman	[83]	brass, iron	water	224
1923	Darcy	[83]	iron	water	10
1923	Mills	[83]	bass	water	25
1927	Corp & Hartwell	[83]	iron, steel	water	244
1930	Hsaio	[83]	glass, copper, iron	water	183
1930	Carnegie	[83]	steel	steam	21
1932	Nikuradse	[119]	brass	water	123
1933	Nikuradse	[118]	sanded brass	water	362
1937	Colebrook & White	[27]	roughened metal	air	50
1969	Patel & Head	[128]	brass	air	53
1982	Schlichting & Gersten	[150]			98
1998	Zagarola & Smits	[178, 106]	aluminum	air	26
2002	Swanson et al.	[160, 106]	stainless steel	gases, liquid He	59
2015	Furuichi et al.	[46]	glass	water	66
2017	Everts & Meyer	[39]	copper	water	103

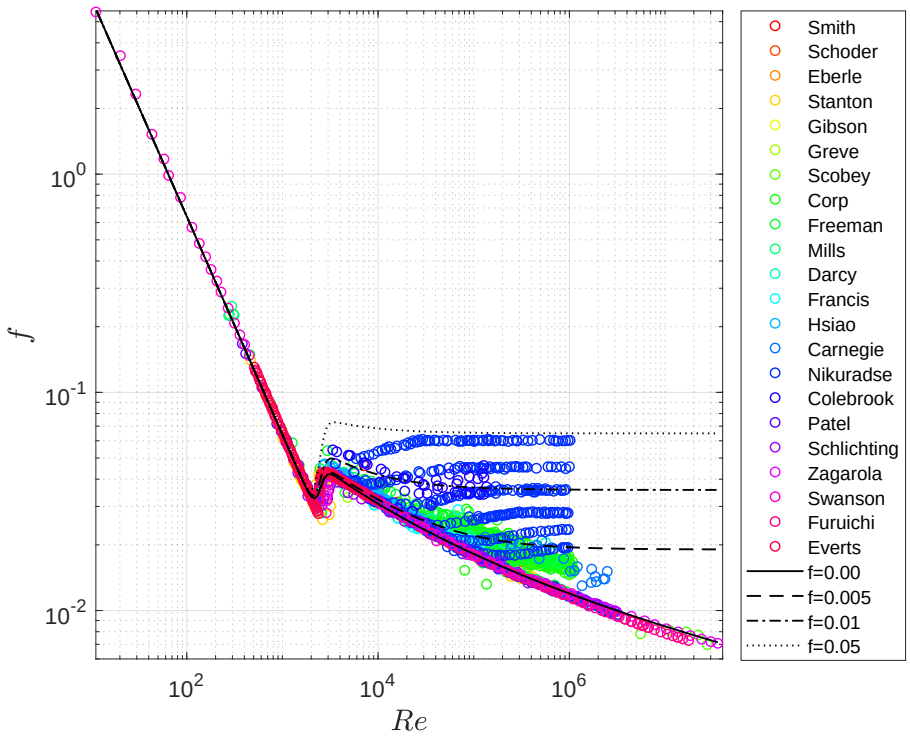

(a) two-dimensional representation, similar to the Moody chart

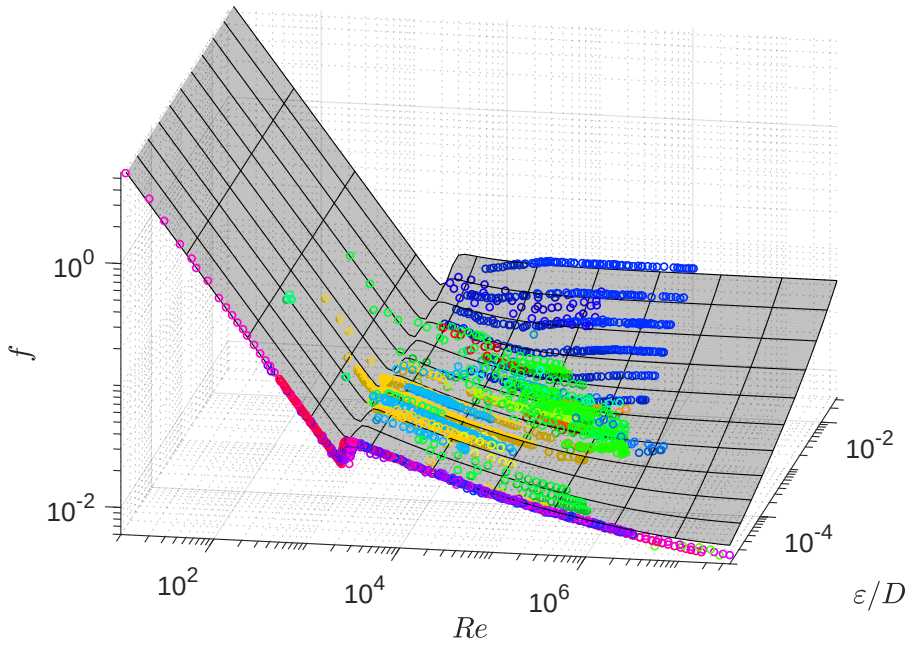

(b) three-dimensional data

Figure 5.2: Friction factor experimental data. Friction factors are dependent upon the Reynolds number and pipe roughness. The color scheme indicated in the legend is used throughout this section.

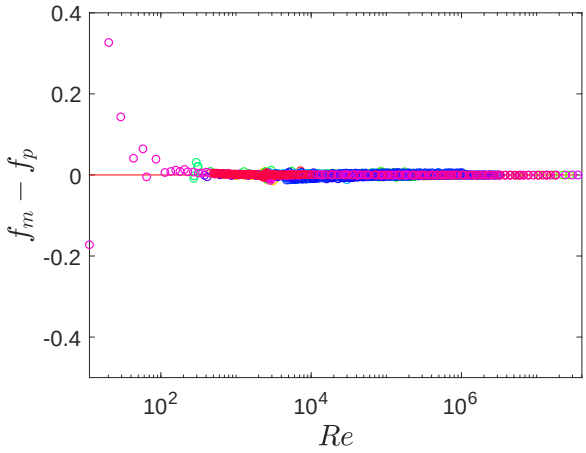

Figure 5.3: Friction factor residuals for untransformed data. The residuals between the data and model vary by many orders of magnitude, which requires a change to the statistical model because the observational error is heteroskedastic.

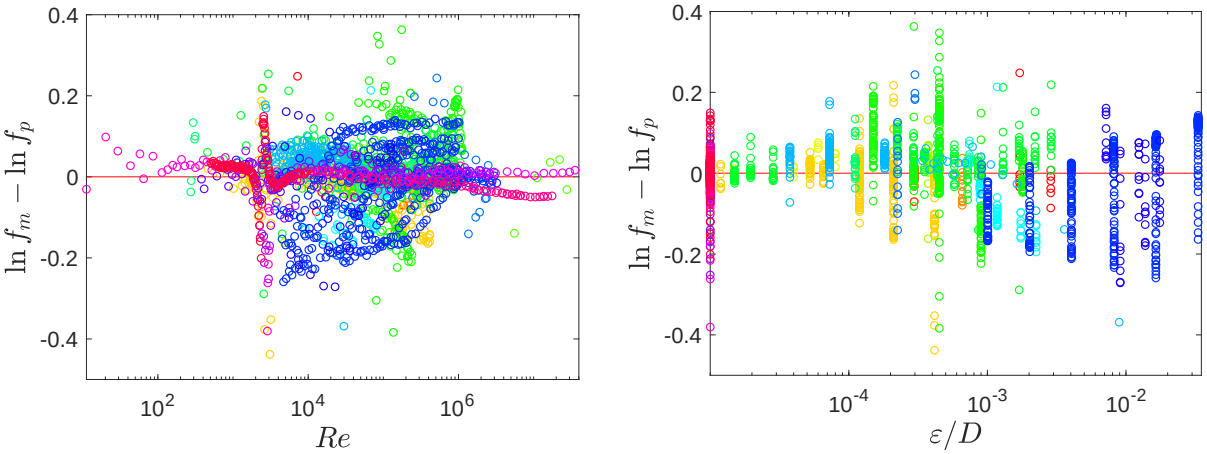

(a) Plotted against Reynolds number

(b) Plotted against relative roughness

Figure 5.4: Friction factor residuals for transformed data. The residuals between the friction factor data and optimized model are more reasonable than for the untransformed data.

Table 5.2: Friction factor marginal parameter distributions. The distributions of all six parameters are summarized by their mean (μ) and standard deviation (σ). These results do not include covariance between the parameters, which is also estimated by all three methods.

	Initial	**Asymptotic**		**Bootstrap**		**DRAM**	
	value	μ	σ	μ	σ	μ	σ
θ_1	0.005	0.00443	0.000327	0.00442	0.000328	0.00419	0.000388
θ_2	2500	2531	17.09	2531	17.18	2535	16.69
θ_3	2.457	2.262	0.02363	2.261	0.02377	2.245	0.02561
θ_4	7	6.544	0.3653	6.567	0.3704	6.568	0.3731
θ_5	0.9	0.9663	0.01358	0.9667	0.01366	0.9741	0.01475
θ_6	0.27	0.1292	0.009120	0.1294	0.009186	0.1232	0.009890
σ^2	0.0881	0.0815	–	0.0815	0.00184	0.0815	0.00124

With the statistical model selected, the three different fixed effects methods are applied: OLS calibration, bootstrapping, and DRAM. All results are summarized in Table 5.2, which shows the marginal distribution of each parameter for the three methods as well as the estimates of the observational error. In addition, Figure 5.5 plots these distributions.

The covariance structure of the parameters is not trivial in this example. The propagation of marginal distributions can lead to a significant overprediction of uncertainty, so the covariance matrix should also be propagated for UQ studies. The three methods have similar results, so the DRAM covariance is shown here.

$$V_{dram} = \begin{bmatrix} 1.50\times10^{-7} & -1.30\times10^{-3} & 8.65\times10^{-7} & -4.48\times10^{-5} & -1.03\times10^{-6} & 3.02\times10^{-7} \\ -1.30\times10^{-3} & 2.79\times10^{+2} & -2.21\times10^{-2} & 2.34\times10^{+0} & 4.44\times10^{-2} & -7.86\times10^{-3} \\ 8.65\times10^{-7} & -2.21\times10^{-2} & 6.56\times10^{-4} & -3.25\times10^{-3} & -3.42\times10^{-4} & 2.49\times10^{-4} \\ -4.48\times10^{-5} & 2.34\times10^{+0} & -3.25\times10^{-3} & 1.39\times10^{-1} & 3.83\times10^{-3} & -1.15\times10^{-3} \\ -1.03\times10^{-6} & 4.44\times10^{-2} & -3.42\times10^{-4} & 3.83\times10^{-3} & 2.17\times10^{-4} & -1.28\times10^{-4} \\ 3.02\times10^{-7} & -7.86\times10^{-3} & 2.49\times10^{-4} & -1.15\times10^{-3} & -1.28\times10^{-4} & 9.78\times10^{-5} \end{bmatrix} \quad (5.10)$$

Once the fixed effects model is finalized and all methods have similar results, a mixed-effects model can be employed. The systematic differences between different laboratories are due to (1) differences in the onset of turbulence due to entry geometry and other effects [160], (2) variations in the fluid properties used to calculate Re and f, (3) different manufacturing procedures and measurement techniques for pipe roughness, (4) possible biases in measurement methods or equipment, and (5) any human errors such as offsets in plotting or incorrect calculations.

With better experimental data, these sources of uncertainty could be minimized. In the meantime, a mixed-effects model can indicate those experiments which are significantly different than the others. A MATLAB© algorithm, `nlmefit`, is used to calculate an MLE estimate of the parameters. The resulting parameter estimates and covariance matrix of the mixed-effects,

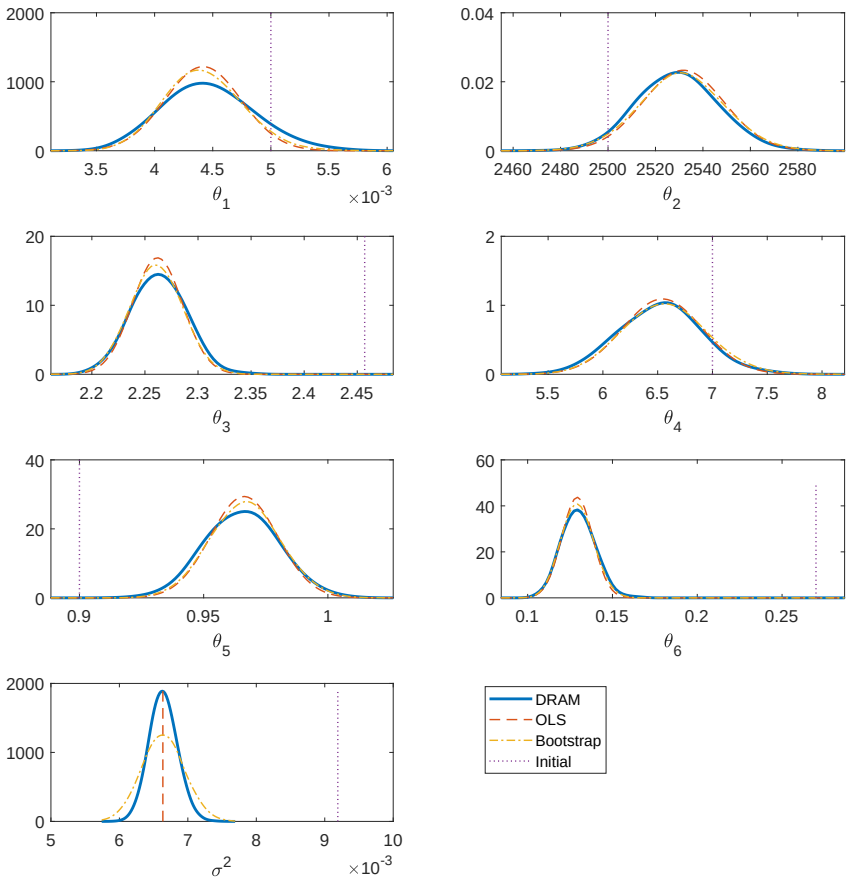

Figure 5.5: Friction factor results. The three different fixed effects models have similar estimates for all six parameters as well as the estimate of variance, σ^2.

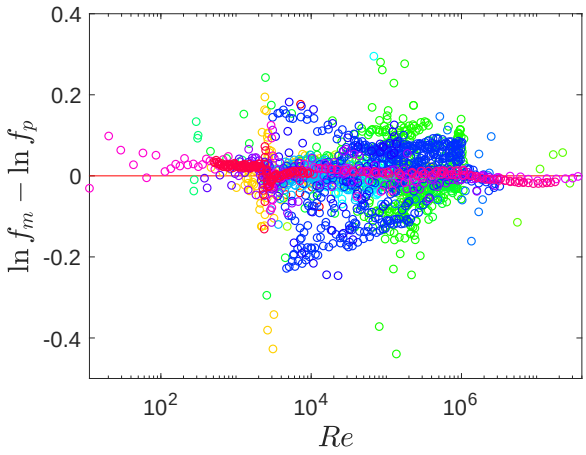

Figure 5.6: Friction factor mixed-effects residuals. The residuals for the mixed-effects model are smaller than the fixed effects residuals. This indicates that the mixed-effects model appropriately accounts for systematic differences between the laboratories.

Ψ, are shown in Table 5.3.

Since the mixed-effects model accounts for differences between the laboratories, the resulting model is more accurate. To demonstrate this, the residuals are shown in Figure 5.6. There is an overall reduction in the residuals compared to Figure 5.4.

The fixed effects and mixed-effects residuals are compared in Figure 5.7. Each data set is shown as a separate box plot, each of which indicate the quartiles, minimum, maximum, and outliers for each laboratory. Many of the fixed effects box plots are significantly displaced from zero. In the mixed-effects analysis, the residuals are mostly centered about zero and therefore the laboratory errors are accounted for. In addition, the overall error is smaller for the mixed-effects results, which is displayed on the plot as a mean squared error.

Finally, the transition region is shown in Figure 5.8 with data from four of the laboratories. The plot also shows the fixed effect result and the global parameters of the mixed-effects analysis. This is a situation where the fixed model cannot account for laboratory errors.

The friction factor correlation was calibrated using a fixed effects statistical model. It was shown that all three models give similar results for the joint parameter distribution and observational error. In addition, the mixed-effects analysis accounted for systematic biases in the data that artificially inflate the observational error in the fixed effect model.

5.2 Convective Heat Transfer

Heat transfer from a heated solid to a flowing liquid is an important physical process, especially in nuclear reactors. This heat transfer process is governed by the heat transfer coefficient, which

Table 5.3: Estimated parameter values for mixed-effects friction model. Results are summarized for the frequentist `nlmefit` MATLAB© algorithm, where the combination of fixed and mixed results $\theta + \beta$ are shown along with the covariance matrix of the mixed-effects Ψ.

	`nlmefit` parameter estimates					
Parameter	$i = 1$	$i = 2$	$i = 3$	$i = 4$	$i = 5$	$i = 6$
$\theta_i + \beta_{i1}$	0.008123	2576.8	2.153	4.255	0.894	-0.0252
$\theta_i + \beta_{i2}$	0.008123	2576.8	2.205	3.767	0.925	0.0757
$\theta_i + \beta_{i3}$	0.008123	2576.8	2.207	3.158	0.946	0.0913
$\theta_i + \beta_{i4}$	0.003896	2508.5	2.271	6.231	0.952	-0.0073
$\theta_i + \beta_{i5}$	0.008123	2576.8	2.214	4.184	0.920	0.0660
$\theta_i + \beta_{i6}$	0.008123	2576.8	2.141	1.746	0.865	0.0533
$\theta_i + \beta_{i7}$	0.008123	2576.8	2.244	3.032	0.934	0.0612
$\theta_i + \beta_{i8}$	0.008123	2576.8	1.977	0.298	0.770	0.0037
$\theta_i + \beta_{i9}$	0.005666	2584.7	2.251	9.530	0.999	0.1484
$\theta_i + \beta_{i10}$	0.007654	2449.0	2.199	3.665	0.909	0.0624
$\theta_i + \beta_{i11}$	0.008127	2576.8	2.162	3.873	0.927	0.0964
$\theta_i + \beta_{i12}$	0.008127	2576.8	1.965	0.281	0.815	0.0128
$\theta_i + \beta_{i13}$	0.008883	2473.0	2.243	5.597	0.930	0.0073
$\theta_i + \beta_{i14}$	0.008127	2576.8	2.103	4.905	0.860	-0.0091
$\theta_i + \beta_{i15}$	0.009217	2543.6	2.572	1.842	0.771	0.2816
$\theta_i + \beta_{i16}$	0.008375	2572.1	2.056	4.511	1.003	0.0606
$\theta_i + \beta_{i17}$	0.007005	2473.6	2.196	3.276	0.907	0.0612
$\theta_i + \beta_{i18}$	0.004014	2803.3	2.263	5.448	0.945	0.0612
$\theta_i + \beta_{i19}$	0.008127	2576.8	2.262	5.237	0.944	0.0612
$\theta_i + \beta_{i20}$	0.011908	2912.2	2.264	5.415	0.945	0.0612
$\theta_i + \beta_{i21}$	0.008127	2576.8	2.317	8.269	0.974	0.0612
$\theta_i + \beta_{i22}$	0.014653	2447.9	2.178	2.826	0.897	0.0612
σ^2	0.004195					
Ψ	$\begin{bmatrix} 1.74 \times 10^{-5} & 0 & 0 & 0 & 0 & 0 \\ 0 & 30670 & 0 & 0 & 0 & 0 \\ 0 & 0 & 0.0331 & 0 & 0 & 0 \\ 0 & 0 & 0 & 7.54 & 0 & 0 \\ 0 & 0 & 0 & 0 & 0.00762 & 0 \\ 0 & 0 & 0 & 0 & 0 & 0.00778 \end{bmatrix}$					

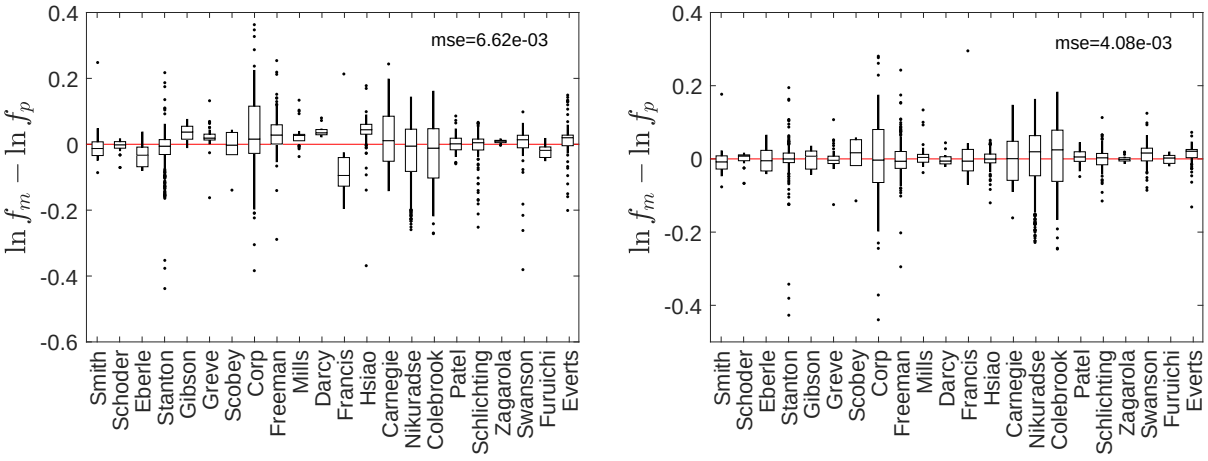

(a) Fixed effects model

(b) Mixed-effects model

Figure 5.7: Friction factor residual box plots. The mixed-effects model accounts for systematic biases due to the different laboratories.

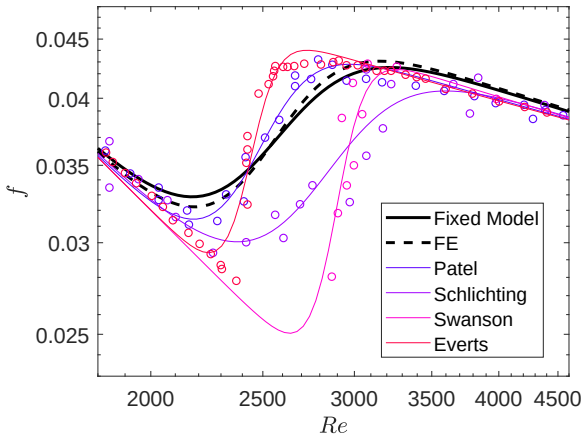

Figure 5.8: Example of mixed-effects results for the friction factor. A selection of smooth pipe results are plotted here with (1) the fixed effect DRAM results, (2) the fixed part of the mixed DRAM model, and (3) the overall mixed-effects model for each laboratory. The clear biases between the different experiments in the transition regime are accounted for in the mixed framework.

relates heat flux to a temperature difference.

$$h = \frac{q''}{T_w - T_f} \tag{5.11}$$

Here, the heat transfer coefficient h is related to the heat transfer per area from the solid q'' and the temperature differential between the wall and the bulk fluid $T_w - T_f$. In general terms, the heat transfer coefficient is influenced by the Reynolds number, Prandtl number, Grashof number, pipe roughness, entrance effects, and geometry. Similar to the friction factor correlation, the effect of natural circulation and entrance effects are assumed negligible. The roughness effect is generally neglected as well. The heat transfer coefficient is determined empirically based on experimental data for smooth pipes, where an equivalent diameter is used for other geometries.

The most commonly used correlation is that of Dittus-Boelter, which is for heating of internal flow through smooth tubes.

$$Nu = 0.023 Re^{0.8} Pr^{0.4} \tag{5.12}$$

Here, Nu is the Nusselt number and Pr is the Prandtl number. The Prandtl exponent is changed to 0.3 for cooling liquid, but this section is only concerned with heating because it is the general mode of transfer in nuclear reactors. As pointed out in [176], this form of the heat transfer correlation is incorrectly attributed to Dittus and Boelter's work [38]. Instead, it originated in an early edition of McAdams' heat transfer book [103]. It is derived through a combination of the Chilton-Colburn analogy with Moody's equation for friction in smooth pipes $f = 0.184/Re^{0.2}$, where the Prandtl exponent is adjusted to fit data.

$$Nu = \frac{f Re Pr^{1/3}}{8} = \frac{0.184 Re Pr^{1/3}}{8 Re^{0.2}} = 0.023 Re^{0.8} Pr^{1/3} \tag{5.13}$$

McAdams merely credited Dittus and Boelter with the use of average fluid properties rather than film properties in the equation. Nonetheless, the Dittus-Boelter correlation is used throughout the nuclear industry to approximate heat transfer in nuclear reactors. It is included in the heat transfer models of CTF, CTF-R, and RELAP5-3D©.

The correlation is calibrated to an extensive set of experimental data for heat transfer from smooth tubes to flowing fluid. Twelve sources are used to obtain 829 data points for the calibration. All data sources are shown chronologically in Table 5.4 with the type of transfer measured, the material of the pipe used, the working fluid, and number of data points extracted. The data is plotted in Figure 5.9 as the traditional two-dimensional plot with the Reynolds number and Prandtl number are collapsed into a single dimension, as well as in three dimensions.

The Dittus-Boelter equation is parameterized with $\boldsymbol{\theta} = [\theta_1, \theta_2, \theta_3]$.

$$Nu = \theta_1 Re^{\theta_2} Pr^{\theta_3} \tag{5.14}$$

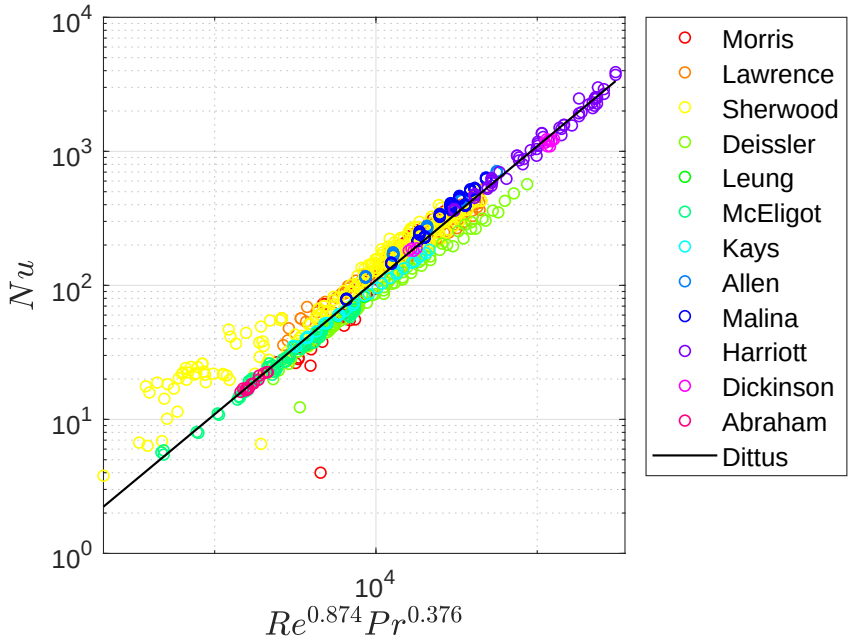

(a) two-dimensional

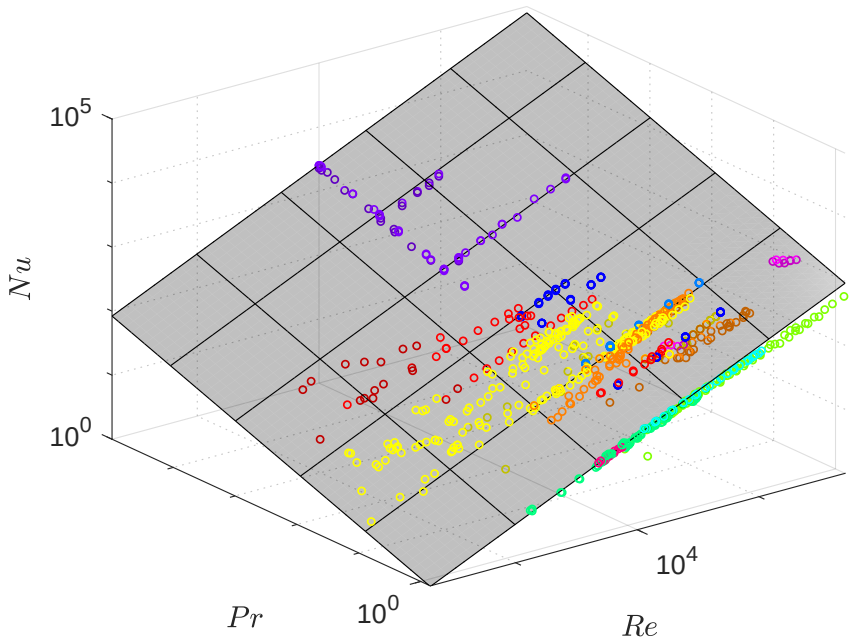

(b) three-dimensional

Figure 5.9: Heat transfer experimental data. Heat transfer is determined by the Nusselt number, which depends on Reynolds number and Prandtl number. Both plots also show a the calibrated Dittus-Boelter model.

Table 5.4: Data sources for the heat transfer correlation. Each source is indicated chronologically with the transfer type modeled, pipe material, working fluid, and number of data points extracted.

Year	Author	Ref.	Transfer type	Pipe	Fluid	Data points
1928	Morris & Whitman	[113]	heating	steel	water	12
					oil	44
			cooling			62
1931	Lawrence & Sherwood	[87]	heating	copper	water	127
1932	Sherwood & Petrie	[152]	heating	copper	water	34
					acetone	34
					benzene	83
					kerosene	79
					n-butyl alc.	30
1952	Deissler & Eian	[36]	heating	Inconel	air	74
1962	Leung et al.	[89, 105]	heating	Inconel	air	14
1963	McEligot et al.	[104]	heating	Inconel	air, He	66
1963	Kays & Leung	[79]	heating	Inconel	air	29
1964	Allen & Eckert	[6]	heating	stainless steel	water	37
1964	Malina & Sparrow	[97]	heating	stainless steel	water	29
					oil	53
1965	Harriott & Hamilton	[61]	mass	benzoic acid	glycerin sol.	58
1968	Dickinson	[37, 155]	heating	stainless steel	water	12
2011	Abraham et al.	[2]	heating		air	14

An initial OLS calibration indicates that the residuals are non-iid, as shown in Figure 5.10. The heteroskedastic Nusselt number errors range over four orders of magnitude, which leads to huge variation in the corresponding residuals. As such, the heat trasfer data and model are logarithmically transformed such that $\ln y = \ln f$. This is the same transformation that was used for the friction factor model.

The residuals for the transformed model are plotted in Figure 5.11 against both the Reynolds number and Prandtl number. Once the heat transfer correlation is transformed, the residuals behave much more appropriately.

The identifiability analysis of the Dittus-Boelter equation is performed and the resulting diagonal elements of Q are $[-825, 36.0, 66.7]$. The sensitivity matrix is rank sufficient, so the three parameters are uniquely identifiable. Therefore, the model with three parameters will be used for the fixed effects analysis.

After the data and model are finalized and the identifiable and sensitive parameters are selected, the three fixed effects calibration methods are applied. The marginal distributions of the parameters are summarized as a mean and standard deviation in Table 5.5. In addition, the

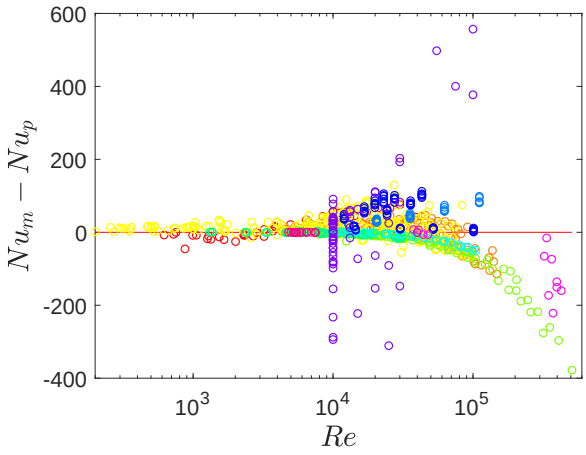

Figure 5.10: Heat transfer residuals for untransformed data. The residuals between the data and model vary by many orders of magnitude, which must be treated so that the iid assumption of the statistical model is not violated.

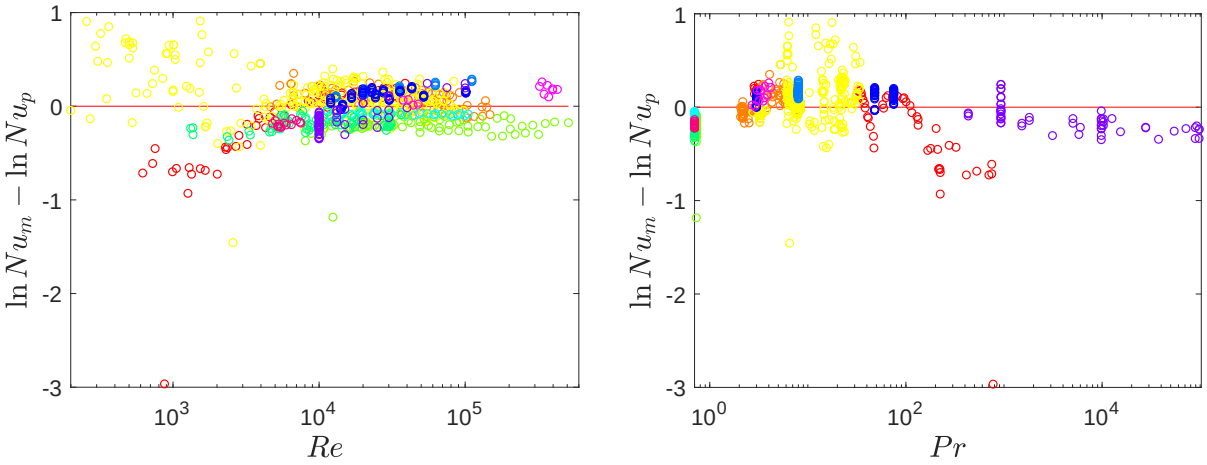

(a) Plotted against Reynolds number

(b) Plotted against Prandtl number

Figure 5.11: Heat transfer residuals for transformed data. The residuals between the experiment and optimized model are more iid for the transformed data.

Table 5.5: Heat transfer parameter results. The distributions of all six parameters are summarized by their mean (μ) and standard deviation (σ). These results do not include covariance between the parameters, which is also estimated by all three methods.

	Initial value	**Asymptotic**		**Bootstrap**		**DRAM**	
		μ	σ	μ	σ	μ	σ
θ_1	0.023	0.0349	0.00244	0.0350	0.00242	0.0367	0.00247
θ_2	0.8	0.761	0.00682	0.761	0.00677	0.757	0.00689
θ_3	0.4	0.384	0.00380	0.384	0.00384	0.378	0.00386
σ^2	0.252	0.246	–	0.245	0.0231	0.246	0.00604

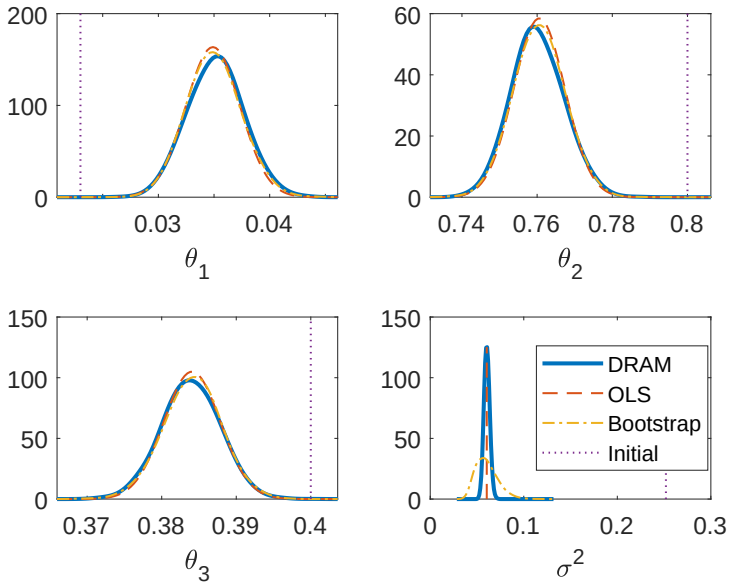

Figure 5.12: Heat transfer marginal parameter distributions. The three different fixed effects models have similar estimates for all six parameters as well as the estimate of variance, σ^2.

estimates of variance of the observational error σ^2 are shown.

The estimate of the covariance matrix from the DRAM algorithm is shown here.

$$V_{dram} = \begin{bmatrix} 6.11 \times 10^{-6} & -1.68 \times 10^{-5} & -3.34 \times 10^{-6} \\ -1.68 \times 10^{-5} & 4.75 \times 10^{-5} & 6.54 \times 10^{-6} \\ -3.34 \times 10^{-6} & 6.54 \times 10^{-6} & 1.49 \times 10^{-5} \end{bmatrix} \tag{5.15}$$

Two of the parameters, θ_1 and θ_2, are strongly correlated ($\text{corr}\,(\theta_1, \theta_2) = \text{cov}\,(\theta_1, \theta_2)/(\sigma_{\theta_1}\sigma_{\theta_2}) = 0.99$). As such, it will be important to incorporate the joint distribution into any future propagation exercises.

Before transitioning to a mixed-effects analysis, the strong correlation between θ_1 and θ_2 will

require an adjustment to the model. Even though the two parameters are strictly identifiable, their strong correlation will cause the mixed-effects model to be overparameterized. As such, either θ_1 or θ_2 will be fixed for the mixed-effects analysis. Here, we fix θ_2 to its optimized value.

$$Nu = \theta_1 Re^{0.761} Pr^{\theta_3} \tag{5.16}$$

Fixing θ_2 is consistent with experimental procedures, since most experimentalists tune θ_1 to match data. The results from `nlmefit` are shown in Table 5.6. The results indicate that a mixed-effects model would be beneficial and account for laboratory errors.

Table 5.6: Estimated parameter values for mixed-effects heat transfer model. Results are summarized for the frequentist `nlmefit` MATLAB© algorithm and DRAM method, where the combination of fixed and mixed results $\theta + \beta$ are shown along with the covariance matrix of the mixed-effects Ψ.

	`nlmefit`	
Parameter	$i = 1$	$i = 2$
$\theta_i + \beta_{i1}$	0.0556	0.216
$\theta_i + \beta_{i2}$	0.0316	0.487
$\theta_i + \beta_{i3}$	0.0335	0.447
$\theta_i + \beta_{i4}$	0.0284	0.405
$\theta_i + \beta_{i5}$	0.0323	0.407
$\theta_i + \beta_{i6}$	0.0290	0.406
$\theta_i + \beta_{i7}$	0.0325	0.401
$\theta_i + \beta_{i8}$	0.0383	0.423
$\theta_i + \beta_{i9}$	0.0380	0.393
$\theta_i + \beta_{i10}$	0.0443	0.340
$\theta_i + \beta_{i11}$	0.0378	0.427
$\theta_i + \beta_{i12}$	0.0294	0.405
σ^2	0.03363	
Ψ	$\begin{bmatrix} 6.38 \times 10^{-5} & 0 \\ 0 & 8.68 \times 10^{-3} \end{bmatrix}$	

The residuals between the mixed-effects results and the experimental data are shown in Figure 5.13. A small reduction is apparent when these residuals are compared to Figure 5.11.

The residuals for the fixed and mixed-effects models are compared in Figure 5.14. Similar to the friction factor results, this demonstrates how a mixed-effects statistical model improves model predictions.

The Dittus-Boelter equation was calibrated to an extensive set of data in this section. Future work should transition nuclear codes to correlations which account for natural circulation and

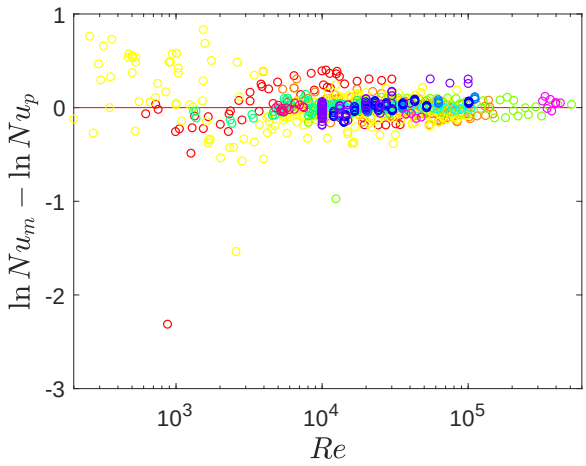

Figure 5.13: Heat transfer mixed-effects residuals. These residuals are smaller than the fixed effects residuals, which indicates that the mixed-effects model accounts for laboratory errors.

entrance effects (such as the Gnielinski equation [51]). These effects are relatively small in LWRs at normal operating conditions, but they will be important in next generation reactors which often rely on natural circulation and use working fluids which have thicker thermal boundary layers than water. In addition, the correlation should be adjusted to account for rod array geometries and the incorporation of roughness effects.

5.3 Uranium Dioxide Thermal Conductivity

Because fuel temperature is an important safety criteria for nuclear reactors, the fuel thermal conductivity is a very important model. An inaccurate prediction of thermal conductivity can drastically impact the predicted temperature distribution in the fuel. This is especially true for thermal hydraulic codes, which do not have any feedback mechanisms to reduce the fuel temperature if it is overpredicted.

Various correlations for thermal conductivity of uranium dioxide are used throughout the industry including the various versions of Material Properties (MATPRO) [59, 154], the Nuclear Fuel Industries (NFI) model [123], the SIM-FUEL model [94], and the Massih model [99]. The most commonly used correlation, the modified NFI model [86], is selected in this work. It was designed for use in FRAPCON, is used in RELAP5-3D© [5], and was recently incorporated into the CTF fuel rod model [164].

The modified NFI model alters the temperature-dependent part of the original NFI model and incorporates the gadolinium term suggested by Massih [99].

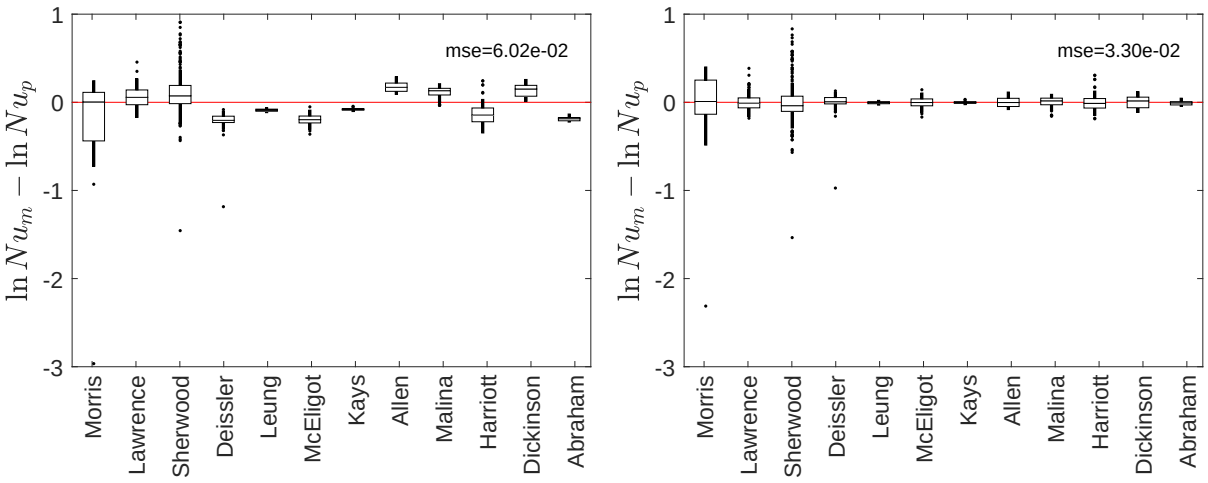

(a) Fixed effects model

(b) Mixed-effects model

Figure 5.14: Heat transfer residual box plots. The mixed-effects model accounts for systematic biases due to the different laboratories.

$$k_f = \Bigg[4.52 \times 10^{-2} + 2.46 \times 10^{-4} T + 1.1599x + 1.87 \times 10^{-3} BU + 0.038 \frac{BU^{0.28}\left(1 - 0.9e^{-0.04BU}\right)}{1 + 396e^{-6380/T}} \Bigg]^{-1} + \frac{3.5 \times 10^9}{T^2} e^{-16361/T} \tag{5.17}$$

Here, k is the fuel thermal conductivity in $W/(mK)$, T is temperature in Kelvin, x is weight percent gadolinium, and Bu is burnup in GWd/MTU. Note that the correlation is not derived analytically and therefore has inconsistent units. The modified NFI model does not account for non-ideal stoichiometry of uranium dioxide or thermal recovery after heating.

The thermal conductivity of nuclear fuel has been the subject of various experiments since the 1970's. Experimental limitations forced early experimentalists to use only unirradiated pure UO_2, but recent studies have been conducted with a variety of burnup and gadolinium contents. For this work, only data extracted using reliable experimental methods is considered and experiments with theoretical densities lower than those in nuclear reactors are excluded. All sources of data used in this work are summarized chronologically in Table 5.7. Most experiments consisted of a thin slab of UO_2 which was heated on one side and the temperature response was measured on the opposite side. Using the steady state conduction equation, the average thermal conductivity in the slab was estimated.

The experimental data is plotted in Figure 5.15. In total, 1,608 data points have been extracted from the available literature. The state space is very well explored for unirradiated fuels, but there is a lack of data for irradiated fuels; for irradiated pellets, there are only 154 data

Table 5.7: Data sources for the thermal conductivity of fuel. Each source is listed chronologically with its burnup, gadolinium content, and number of data points extracted.

Year	Author	Ref.	Burnup [GWd/MTU]	Gadolinium [wt%]	Data points
1960	Lucks & Deem	[93]	0	0	15
1964	Christensen et al.	[59]	0	0	10
	Godfrey et al.	[52, 59]	0	0	57
	Stora et al.	[159]	0	0	13
1970	Bates	[15, 59]	0	0	153
1971	Gibby	[49, 59]	0	0	45
1972	Fayl & Hansen	[41]	0	0	9
	Weilbacher	[172, 59]	0	0	30
1973	Goldsmith & Douglas	[53, 59]	0	0	52
	Washington	[171]	0	0	144
1974	Hobson et al.	[66, 59]	0	0	36
1982	Fukushima et al.	[45]	0	0-10	525
	Newman	[99]	0	0-6	45
1990	Hirai	[64]	0	0-10	122
1994	Carrol et al.	[86]	40	0	10
1996	Nakamura et al.	[116]	63	0	30
1997	Ohira & Itagaki	[123]	61	0	12
1999	Ronchi et al.	[142]	0	0	125
2000	Ikeda et al.	[72]	0, 40	0, 10	57
2002	Amaya et al.	[7]	38-61	0-4.5	84
2004	Ronchi et al.	[143]	30-60	0	11
2006	Walker et al.	[169]	100	0	23

points without additives and 59 points with gadolinium. Note that the thermal conductivities of all experiments have been adjusted to 95% theoretical density using Loeb's porosity correction factor [92].

The modified NFI correlation is initially parameterized with 12 parameters.

$$k_f = \left[\theta_1 + \theta_2 T + \theta_3 x + \theta_4 BU + \theta_5 \frac{BU^{\theta_6}\left(1 - \theta_7 e^{-\theta_8 BU}\right)}{1 + \theta_9 e^{-\theta_{10}/T}}\right]^{-1} + \frac{\theta_{11}}{T^2} e^{-\theta_{12}/T} \tag{5.18}$$

The identifiability analysis indicates that the sensitivity matrix is rank deficient, so one parameter is unidentifiable. The initial sensitivity results indicate diagonal elements of Q in the QR decomposition of [396, 2.82×10^5, -811, -5490, 102, 2.83, 0.00325, -0.510, 0.0415, -3.28×10^{-4}, -3.73×10^{-10}, $-0.005\,93$]. The unidentifiable parameter, θ_{11}, is fixed along with other nearly identifiable parameters. The resulting model has five parameters.

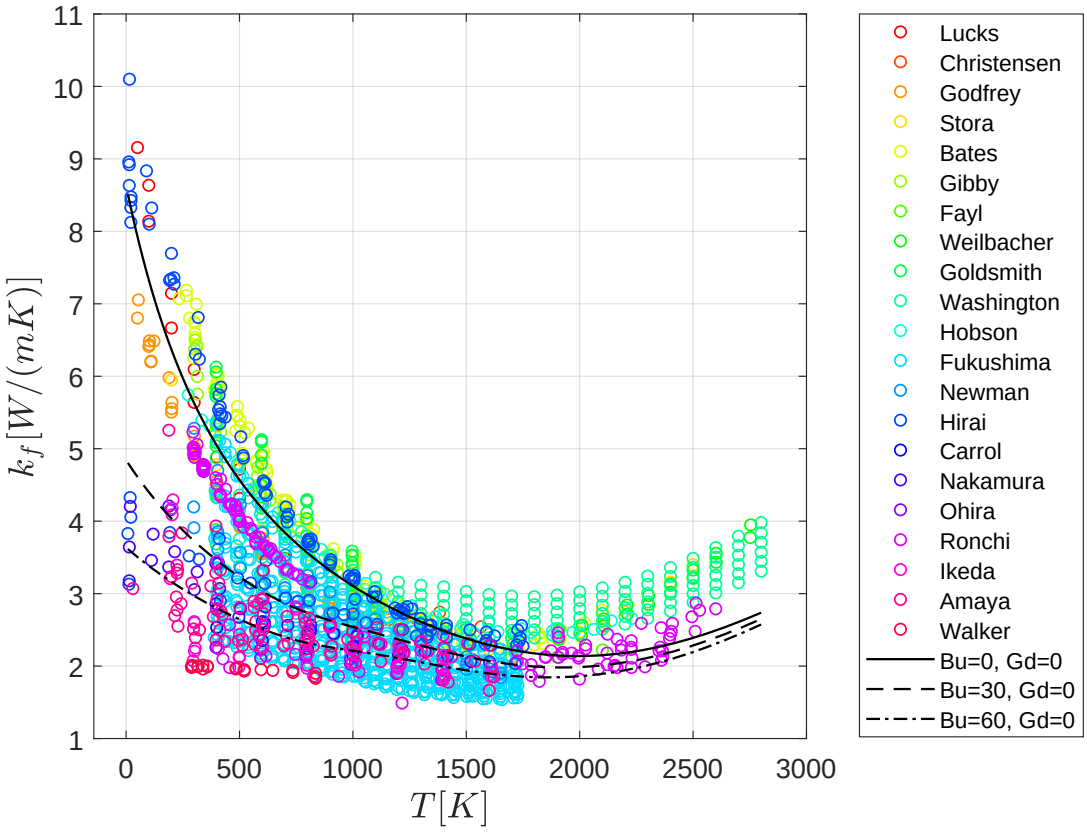

Figure 5.15: Fuel thermal conductivity experimental data. The empirical model for uranium dioxide thermal conductivity is four dimensional and therefore difficult to plot. All data is shown here, though it should be noted that burnup and gadolinium content both degrade the thermal conductivity.

$$k_f = \left[\theta_1 + \theta_2 T + \theta_3 x + \theta_4 BU + \theta_5 \frac{BU^{0.28}\left(1 - 0.9e^{-0.04BU}\right)}{1 + 396e^{-6380/T}}\right]^{-1} + \frac{3.5 \times 10^9}{T^2} e^{-16361/T} \quad (5.19)$$

An initial OLS optimization is performed using the selected parameterized model. The resulting residuals are shown in Figure 5.16. The residuals are plotted with respect to the different independent variables in Figures 5.16a, 5.16b, and 5.16c. A few of the datasets have clear lines on the residual plot, which indicate that there is a dependence between the residual and the independent variables. Therefore, the residuals are not iid.

The three fixed effects calibrations are performed and resulting marginal parameter distributions are summarized in Table 5.8. The results for all five parameters match relatively well for both their mean and standard deviation. The mean model variance σ^2 is almost the same for all three methods, and is significantly reduced when compared to the initial model.

Table 5.8: Fuel thermal conductivity marginal parameter distributions. The distributions of all five parameters are summarized by their mean (μ) and standard deviation (σ). The variance σ^2 of observational error is also included.

	Initial value	**Asymptotic**		**Bootstrap**		**DRAM**	
		μ	σ	μ	σ	μ	σ
θ_1	0.0452	0.1158	0.001160	0.1165	0.001166	0.1162	0.001181
θ_2	0.000246	0.000206	0.00000227	0.000203	0.00000218	0.000205	0.00000224
θ_3	1.1599	0.0186	0.000522	0.0184	0.000511	0.0190	0.000556
θ_4	0.00187	0.00144	0.000314	0.00181	0.000319	0.00177	0.000304
θ_5	0.038	0.0251	0.00691	0.0160	0.00694	0.0172	0.00661
σ^2	1.947	0.416	–	0.415	0.00875	0.416	0.00727

These distributions are plotted in Figure 5.17. The parameter distributions are slightly offset from one another, but still relatively consistent. The covariance matrix from the DRAM algorithm is given here.

$$V_{dram} = \begin{bmatrix} 1.40 \times 10^{-6} & -2.00 \times 10^{-9} & -7.34 \times 10^{-9} & 1.75 \times 10^{-8} & -5.76 \times 10^{-7} \\ -2.00 \times 10^{-9} & 5.02 \times 10^{-12} & -3.01 \times 10^{-10} & -4.74 \times 10^{-11} & 8.96 \times 10^{-10} \\ -7.34 \times 10^{-9} & -3.01 \times 10^{-10} & 3.09 \times 10^{-7} & 7.40 \times 10^{-9} & -1.70 \times 10^{-7} \\ 1.75 \times 10^{-8} & -4.74 \times 10^{-11} & 7.40 \times 10^{-9} & 9.21 \times 10^{-8} & -1.94 \times 10^{-6} \\ -5.76 \times 10^{-7} & 8.96 \times 10^{-10} & -1.70 \times 10^{-7} & -1.94 \times 10^{-6} & 4.37 \times 10^{-5} \end{bmatrix} \quad (5.20)$$

Once the fixed effects analysis is complete, the correlation is analyzed using a mixed-effects model. For the thermal conductivity experiments, laboratory errors originate from considerations such as (1) measurement techniques or accuracy, (2) inaccurate theoretical density measurements, (3) non-stoichiometric samples, and (4) different delays between irradiation and measurement.

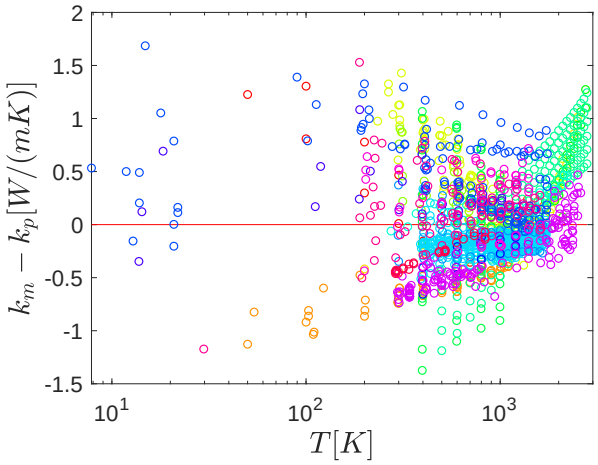

(a) Plotted against temperature

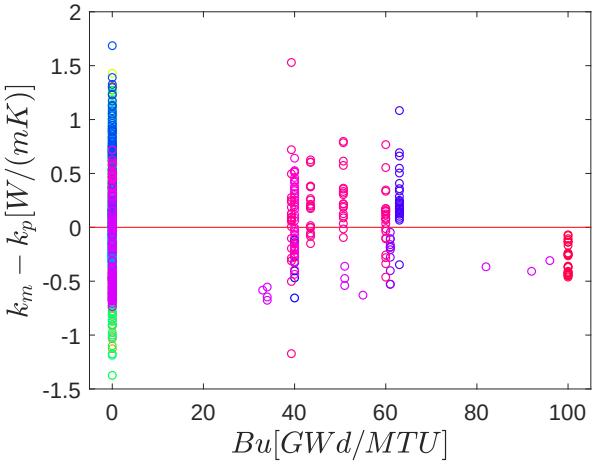

(b) Plotted against burnup

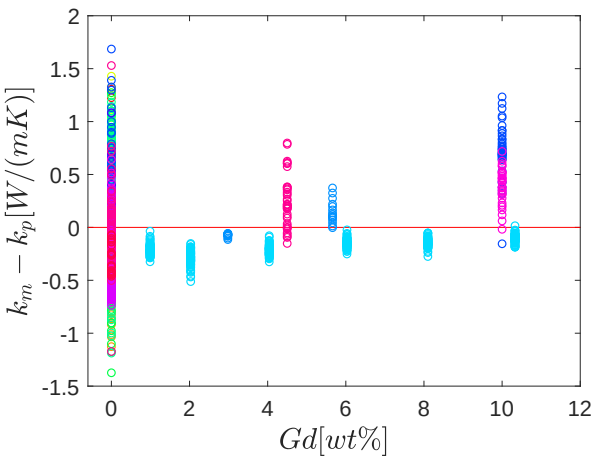

(c) Plotted against gadolinium content

Figure 5.16: Fuel thermal conductivity residuals. The residuals between the experiment and optimized model are relatively centered about zero, though there do appear to be some trends in the data.

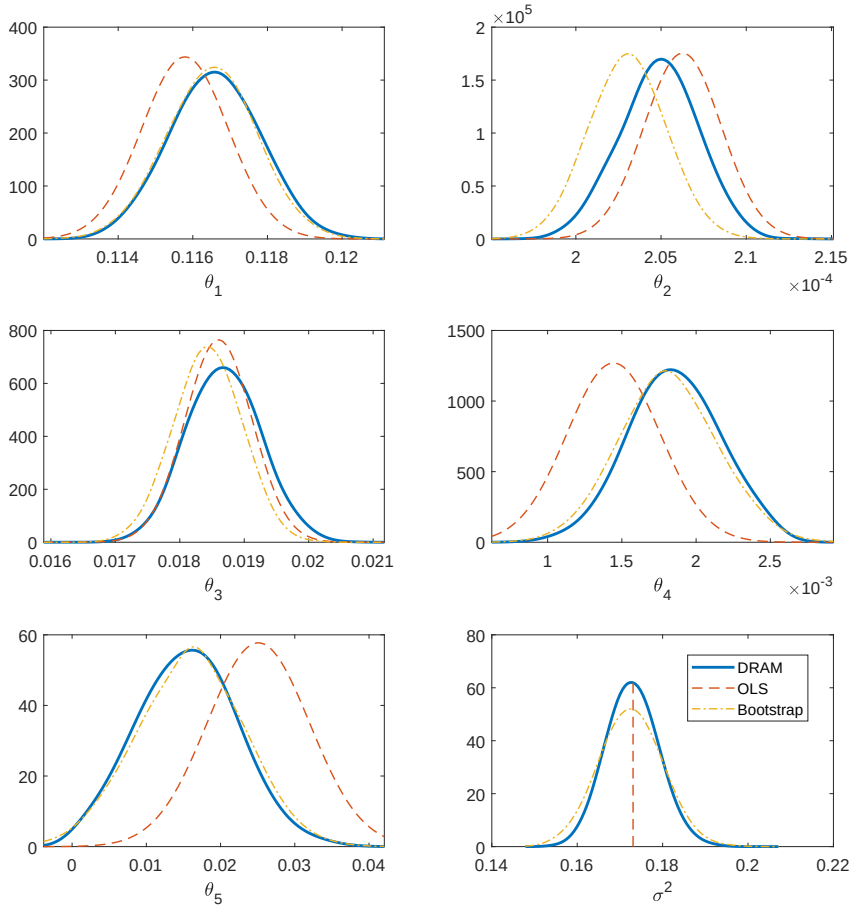

Figure 5.17: Fuel thermal conductivity marginal parameter distributions. The three fixed effects models have similar estimates for all five parameters as well as the estimate of variance, σ^2.

Accounting for these differences will result in a more accurate statistical model. The mean total parameter values $\boldsymbol{\theta} + \beta$ are shown in Table 5.9 for the `nlmefit` algorithm.

Table 5.9: Estimated parameter values for mixed-effects fuel thermal conductivity model. Results are summarized for the frequentist `nlmefit` MATLAB© algorithm, where the combination of fixed and mixed results $\theta + \beta$ are shown along with the covariance matrix of the mixed-effects Ψ.

	`nlmefit`				
Parameter	$i = 1$	$i = 2$	$i = 3$	$i = 4$	$i = 5$
$\theta_i + \beta_{i1}$	0.0951	0.000253	0.0133	0.00214	0.0229
$\theta_i + \beta_{i2}$	0.1485	0.000183	0.0133	0.00214	0.0229
$\theta_i + \beta_{i3}$	0.1308	0.000238	0.0133	0.00214	0.0229
$\theta_i + \beta_{i4}$	0.1425	0.000171	0.0133	0.00214	0.0229
$\theta_i + \beta_{i5}$	0.0813	0.000225	0.0133	0.00214	0.0229
$\theta_i + \beta_{i6}$	0.0930	0.000224	0.0133	0.00214	0.0229
$\theta_i + \beta_{i7}$	0.1014	0.000217	0.0133	0.00214	0.0229
$\theta_i + \beta_{i8}$	0.2101	0.000100	0.0133	0.00214	0.0229
$\theta_i + \beta_{i9}$	0.1123	0.000209	0.0133	0.00214	0.0229
$\theta_i + \beta_{i10}$	0.2421	0.000079	0.0133	0.00214	0.0229
$\theta_i + \beta_{i11}$	0.1270	0.000174	0.0133	0.00214	0.0229
$\theta_i + \beta_{i12}$	0.1108	0.000231	0.0212	0.00214	0.0229
$\theta_i + \beta_{i13}$	0.1260	0.000225	0.0116	0.00214	0.0229
$\theta_i + \beta_{i14}$	0.1074	0.000185	0.0117	0.00214	0.0229
$\theta_i + \beta_{i15}$	0.1474	0.000187	0.0133	0.00218	0.0245
$\theta_i + \beta_{i16}$	0.0787	0.000180	0.0133	0.00199	0.0179
$\theta_i + \beta_{i17}$	0.1442	0.000177	0.0133	0.00219	0.0251
$\theta_i + \beta_{i18}$	0.1450	0.000198	0.0133	0.00234	0.0290
$\theta_i + \beta_{i19}$	0.0845	0.000218	0.0109	0.00222	0.0225
$\theta_i + \beta_{i20}$	0.1271	0.000162	0.0113	0.00191	0.0169
$\theta_i + \beta_{i21}$	0.1348	0.000158	0.0133	0.00218	0.0241
σ^2			0.05026		
Ψ	$\begin{bmatrix} 0.00176 & 0 & 0 & 0 & 0 \\ 0 & 1.99 \times 10^{-9} & 0 & 0 & 0 \\ 0 & 0 & 1.68 \times 10^{-5} & 0 & 0 \\ 0 & 0 & 0 & 8.57 \times 10^{-8} & 0 \\ 0 & 0 & 0 & 0 & 5.07 \times 10^{-5} \end{bmatrix}$				

The parameters which are related to burnup and gadolinium content are the same as the global parameter for those cases without data for those conditions. For example, θ_3 is the same for almost all datasets, since only five laboratories did experiments with gadolinium content. Therefore, these parameters would be unidentifiable in a general mixed-effects framework and likely lead to overparameterization.

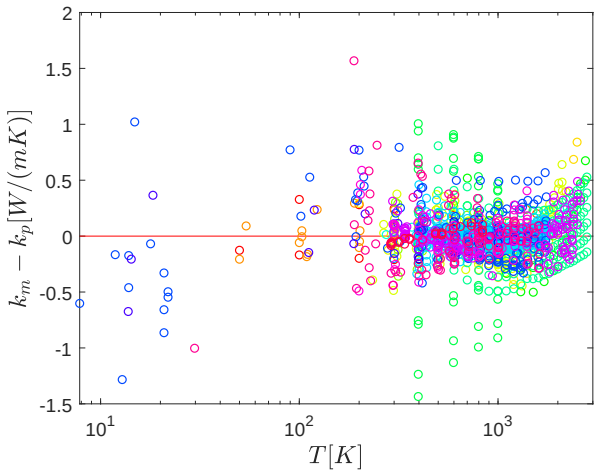

Figure 5.18: Fuel thermal conductivity mixed-effects residuals. The residuals for the mixed-effects model are smaller than the fixed effects residuals.

The residuals for the mixed-effects analysis are shown in Figure 5.18. Overall, they are smaller than the fixed residuals. The residuals are also summarized in Figure 5.19, where the residuals from each laboratory are grouped and summarized using box plots. The fixed effects residuals in Figure 5.19a indicate severe biases in some of the laboratories, where the biases have been mostly resolved in Figure 5.19b.

Future analyses of the fuel thermal conductivity should focus on gathering experimental data for irradiated fuels. This type of data is often proprietary due to cost and safety issues. In addition, the thermal recovery of fuel after it has been heated should be analyzed. Because the fuel temperature is so sensitive to thermal conductivity, these small improvements could lead to large improvements in code predictions.

5.4 Zirconium Cladding Thermal Conductivity

The thermal conductivity of cladding is the final empirical model in CTF-R. It has a small impact on single phase safety parameters, and therefore only a fixed effects calibration is performed for this correlation. The calibration model is taken from an IAEA report [1], where a quadratic fit is made to experimental data from a variety of sources.

$$k_c = 13.09 - 7.92 \times 10^{-4} T + 9.043 \times 10^{-6} T^2 \tag{5.21}$$

Here, the thermal conductivity of the cladding k_c depends only on temperature T. A cubic fit to the data was also considered, but it did not yield significant improvements in accuracy. The correlation is parameterized with $\boldsymbol{\theta} = [\theta_1, \theta_2, \theta_3]$.

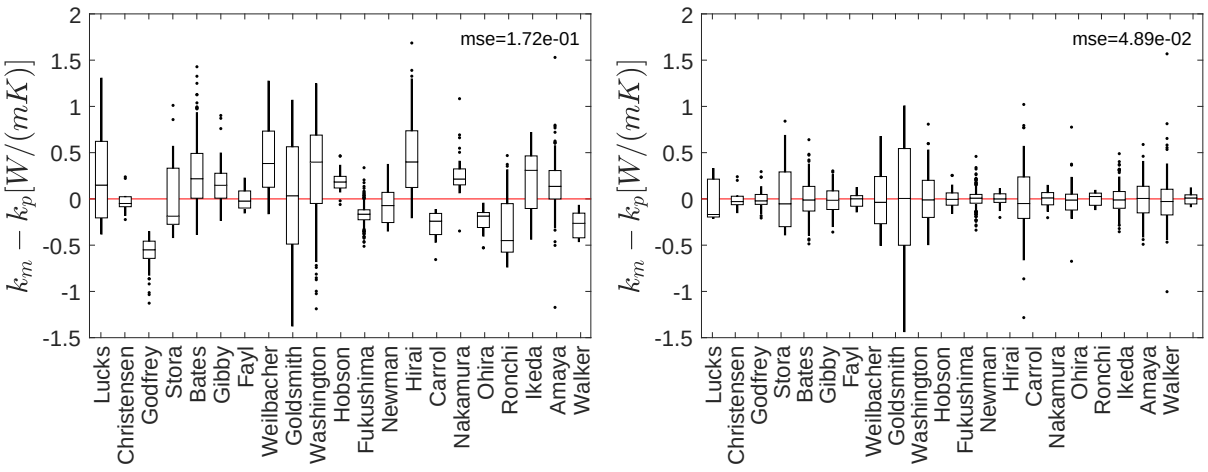

(a) Fixed effects model

(b) Mixed-effects model

Figure 5.19: Fuel thermal conductivity residual box plots. The mixed-effects model accounts for systematic biases due to the different laboratories.

$$k_c = \theta_1 - \theta_2 T + \theta_3 T^2 \tag{5.22}$$

The experimental data is taken from the same IAEA report as the correlation [1]. The data was extracted from a variety of sources and inaccurate data was neglected. The resulting data is plotted in Figure 5.20.

The results of the three fixed effects analyses are outlined in Table 5.10. The marginal distributions of the three parameters are summarized as a mean and standard deviation.

Table 5.10: Cladding thermal conductivity fixed marginal distributions. The distributions of the three parameters are summarized by their mean (μ) and standard deviation (σ).

	Initial value	**Asymptotic**		**Bootstrap**		**DRAM**	
		μ	σ	μ	σ	μ	σ
θ_1	13.09	12.97	0.363	12.97	0.364	12.96	0.359
θ_2	0.000792	0.000769	0.000861	0.000778	0.000865	0.000758	0.000850
θ_3	9.04×10^{-6}	9.07×10^{-6}	4.70×10^{-7}	9.08×10^{-6}	4.73×10^{-7}	8.09×10^{-6}	4.63×10^{-7}
σ^2	0.958	0.955	–	0.953	0.0491	0.957	0.0429

For the joint parameter distribution, the DRAM covariance matrix is also calculated.

$$V_{dram} = \begin{bmatrix} 1.29 \times 10^{-1} & 2.93 \times 10^{-4} & 1.48 \times 10^{-7} \\ 2.93 \times 10^{-4} & 7.22 \times 10^{-7} & 3.84 \times 10^{-10} \\ 1.48 \times 10^{-7} & 3.84 \times 10^{-10} & 2.14 \times 10^{-3} \end{bmatrix} \tag{5.23}$$

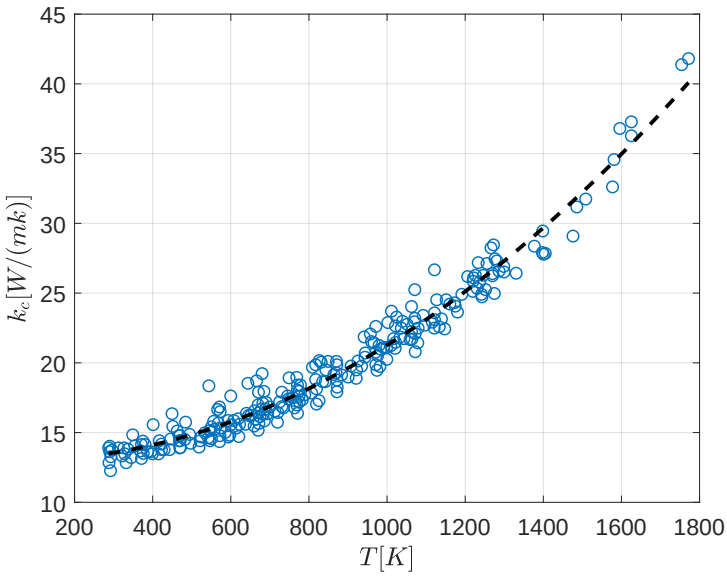

Figure 5.20: Cladding thermal conductivity experimental data.

The residuals for the DRAM calibration are shown in Figure 5.21. These residuals are relatively iid with no obvious trends. Finally, the three parameter distributions are plotted in Figure 5.22 along with the estimate of variance for each of the fixed effects models.

Future work with the cladding thermal conductivity will require the addition of more experimental data and the separation of the existing data into different laboratories. In addition, zirconium properties change significantly with burnup, stress, and hydrogen deposition. None of these contributions are currently accounted for.

5.5 Discussion

The calibration exercises in this chapter did not account for some sources of uncertainty in the data or the model. All of the models do not account for some independent variables that significantly impact the quantity of interest. All correlations are for steady state conditions. The correlations for friction and heat transfer are both for fully developed steady state flow in tubes. Significant improvements in the models can be made by accounting for these higher-order dependencies, which would reduce the model form uncertainty in the code.

Much of the data utilized in this section was digitized using plots in the literature. This process is prone to human error and there is inherent uncertainty that scales with the quality of the images used. Some of the data was extracted in tabular form, but assumptions were usually necessary to put it in a useable form. For example, standard temperature and pressure ($P = 1\,atm$ and $T = 20°C$) were often assumed for the friction factor experiments. Finally, it

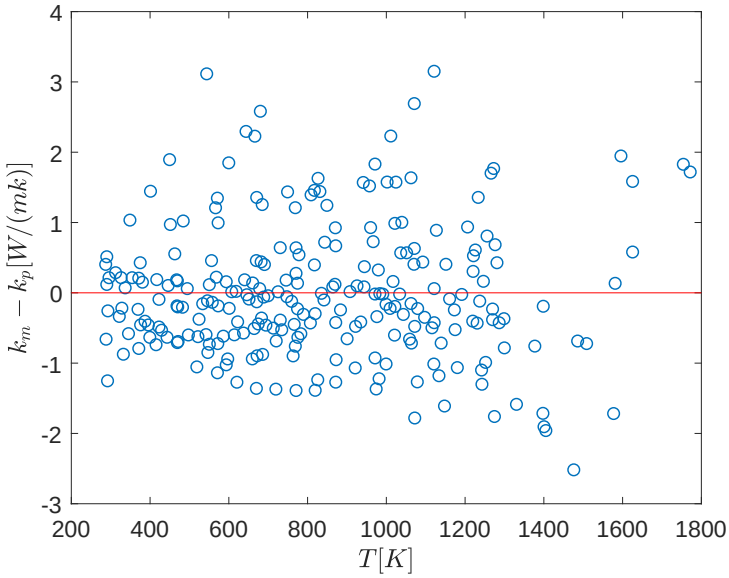

Figure 5.21: Residuals for cladding thermal conductivity model. The residuals for the thermal conductivity model are relatively iid with a mean of zero.

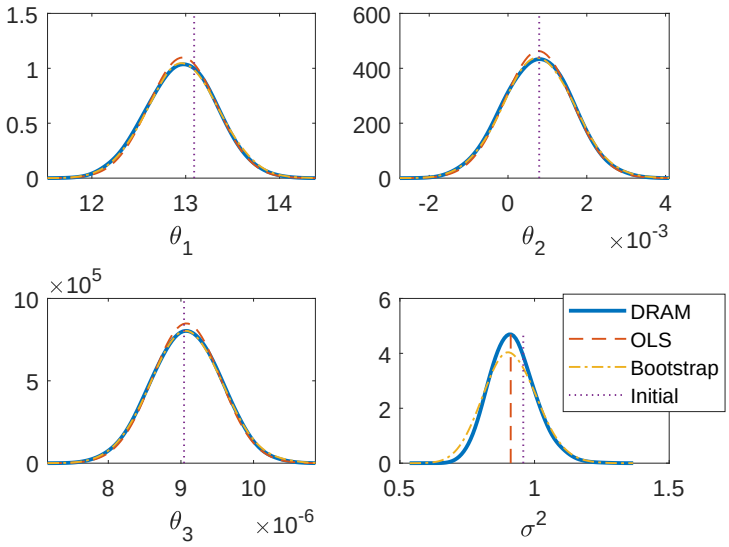

Figure 5.22: Cladding thermal conductivity parameter results. The three different fixed effects models have similar estimates for the three parameters as well as the estimate of variance, σ^2.

was not always possible to calculate fluid properties using the same methods as the original literature. This could lead to large uncertainties in some experiments, especially those that used atypical working fluids.

Further, none of the experiments employed in the calibration exercises were taken from validation experiments. As such, thorough measurements of state variables were not always performed, most lacked any quantification of measurement uncertainty, and there were no repeated experiments. In the future, experiments should be designed and executed for the primary purpose for use in validation. This would greatly increase the accuracy and dependability of analyses in this chapter.

The fixed effects statistical model could be improved in many ways. Uncertainty in the state variables was not included in any of the analyses. This uncertainty, especially for nondimensional numbers in the older data sets, could be quite large. The friction factor and heat transfer coefficient correlations where transformed before performing any analyses because the residuals were not iid. This would not be necessary if the statistical model was reformulated to scale with the model.

$$y = f(x, \boldsymbol{\theta})(1 + \varepsilon) \tag{5.24}$$

A basic DRAM algorithm was used in this work. In the future, these analyses should be transitioned to quantify chain convergence using multiple runs and to subsample the chains to eliminate correlation between them [18, 48].

Finally, future work will include a mixed-effects DRAM analysis. The importance of this analysis was demonstrated using an initial `nlmefit` analysis, which approximated the MLE parameter estimates for global and random effects. It was shown that the biases between laboratories can be treated using this type of analysis. A basic mixed-effects DRAM algorithm—such as that in [156]—could be used, or recent improvements could be incorporated [151].

Regardless of the future work to be performed, this chapter is an improvement over the status quo for most legacy codes. First, all correlations are clearly outlined with their respective origins and assumptions. This is not the case for legacy codes like CTF, where many of the models are undocumented and esoteric. Second, the inclusion of experimental data in the repository will enable future analysts to calibrate and recalibrate the models in whatever way they see fit. Finally, uncertainty analyses of CTF-R will propagate justifiable joint parameter distributions. Future models added to CTF-R will follow this process, which will lead to accurate BEPU quantification of the code.

CHAPTER

6

CONCLUSION

In this work, a novel residual-based version of CTF was developed. The new code is flexible in that its data structures are general and its Jacobian matrix is constructed numerically. These improvements allow the removal of simplifications that were necessary to reduce the computational resources needed to run the code in the 1980's. Since computational tools have been significantly improved since then, these new capabilities are a natural next step.

The initial CTF-R framework is established, including a link to the CTF input and output processing, data structures for state variables, a solution algorithm, single phase residual functions, a solid energy residual function, a numerical algorithm for building the Jacobian, and an interface with PETSc for solving the Jacobian. Each new feature is tested to ensure proper implementation, the mass and energy conservation equations are verified using isokinetic advection test problems, and validation is performed for the friction model. Overall, a decent pedigree is established for the current version of the code.

Though the initial coding of CTF-R is complete, there is a large amount of future work that was discussed in Chapter 4. Some current capabilities of the code remain untested, such as the connection of azimuthal rod fractions to fluid channels, temperature-dependent thermal conductivity models, reverse flows, reverse lateral flows, combinations of different code capabilities, and the numerical implementation of the conduction and momentum equations. The numerical algorithm in CTF-R can be improved by adding a nonlinear iteration, implementing appropriate convergence criteria, nondimensionalizing the Jacobian matrix, and re-examining

the PETSc tolerances. Finally, the code requires a large amount of development so that its capabilities will be consistent with the current version of CTF: the implementation of two-phase flow, additional geometrical modeling options, noncondensible gas and boron, and additional empirical models.

Each CTF-R empirical model is calibrated to an extensive set of nonproprietary experimental data. Through the inclusion of parameter estimates from this process, the code can have a built-in UQ capability that is based purely on experimental data. This will be an improvement over the status quo, which often involves the propagation of expert opinion input distributions for uncertainty analyses. The four empirical models in CTF-R are used for the parameter estimation studies: single phase friction factor, heat transfer from a solid to a working fluid, the thermal conductivity of uranium dioxide, and the thermal conductivity of zirconium.

The primary contributions of this work are detailed below.

- The general methods and solution algorithm of CTF are outlined and possible improvements are discussed.
- A general framework for assessing code credibility is discussed at length. Each individual step is provided with examples.
- A novel residual-based version of CTF is developed for modeling of single phase flow in reactor geometries. The code is written in object-oriented Fortran with capabilities to model wall friction, solid conduction, coupling between the liquid and solid fields, and lateral transfer between adjacent channels.
- A series of defect tests with analytical or approximate solutions are developed and applied to CTF-R simulations. All tests are run with multiple conditions or geometries to show that CTF-R is robust and accurate. These defect tests include (1) one-dimensional steady state isothermal flow problems with constant friction factor, (2) one-dimensional steady state isothermal flow with Reynolds-dependent friction factors, (3) steady state conduction through a nuclear fuel rod with uniform internal heat generation and constant properties, (4) steady state heat transfer from a fuel rod with a uniform axial power profile to the surrounding liquid, (5) steady state heat transfer with a cosine axial power profile, (6) a lateral flow problem with two channels of different areas, and (7) a lateral flow problem with two identical channels.
- Isokinetic advection verification problems are used to show that the CTF and CTF-R mass and energy equations are appropriately first order. This process is repeated for three different waves: square, hyperbolic tangent, and cosine. All three analyses show that the temporal and spatial numerical errors behave appropriately as their respective meshes are refined.
- The CTF and CTF-R friction models are validated using experimental data from Nikuradse

and Furuichi.

- Regression tests are implemented to ensure that CTF-R maintains its capabilities during future development.
- The four empirical models in CTF-R are calibrated to experimental data: friction factor, heat transfer coefficient, thermal conductivity of uranium dioxide, and thermal conductivity of zirconium. Joint parameter distributions are constructed in all cases using three methods: asymptotic analysis, bootstrapping, and DRAM. The resulting joint parameter distributions can be applied to future uncertainty analyses of CTF-R and other codes.

CTF-R is modern code that, with further development, will have varied future applications. The flexibility in the residual equations will allow a more implicit solution algorithm, which enables the use of larger time steps for a particular problem. CTF-R could be used to find a solution to the steady state conservation equations. Not only will CTF-R be capable of modeling light water reactors like CTF, but its governing equations, empirical models, and geometry could be adjusted to model next generation reactors. Given these important applications, the CTF-R framework established in this work will be an important contribution to the future of CTF.

References

[1] Thermophysical properties database of materials for light water reactors and heavy water reactors. Technical Report IAEA-TECDOC-1496, IAEA, June 2006.

[2] J. P. Abraham, E. M. Sparrow, and W. J. Minkowycz. Internal-flow Nusselt numbers for the low-Reynolds-number end of the laminar-to-turbulent transition regime. *Int. J. Heat Mass Transfer*, 54(1):584–588, January 2011. https://doi.org/10.1016/j.ijheatmasstransfer.2010.09.012.

[3] NRC. 10 CFR §50.46: Acceptance criteria for emergency core cooling systems for light-water nuclear power reactors. https://www.nrc.gov/reading-rm/doc-collections/cfr/part050/part050-0046.html.

[4] NRC, Washington, D.C. *TRACE v5.0 Theory Manual: Field Equations, Solution Manual, and Physical Models*.

[5] The RELAP5-3D© Code Development Team. *RELAP5-3D© Code Manual, Volume I: code structure, system models, and solution methods*. INL, June 2005.

[6] R. W. Allen and E. R. G. Eckert. Friction and heat-transfer measurements to turbulent pipe flow of water (Pr=7 and 8) at uniform wall heat flux. *J. Heat Transfer*, 86(3):301–310, August 1964. http://doi.org/10.1115/1.3688680.

[7] M. Amaya et al. Thermal conductivities of irradiated UO_2 and (U,Gd)O_2 pellets. *J. Nucl. Mater.*, 300:57–64, 2002. https://doi.org/10.1016/S0022-3115(01)00704-8.

[8] J. G. M. Andersen. REMI/HEAT COOL, A model for evaluation of core heat-up and emergency core spray cooling system performance for light-water-cooled nuclear power reactors. Technical Report Risø 296, Danish Atomic Energy Commission, September 1973.

[9] ANSYS. *ANSYS FLUENT 12.0 User's Guide*, April 2009.

[10] B. C. Arnold, N. Balakrishnan, and H. N. Nagaraja. *A First Course in Order Statistics*. SIAM, Philadelphia, PA, 2008.

[11] D. L. Aumiller et al. COBRA-IE: A new sub-channel analysis code. In *Proceedings of the 16th International Topical Meeting on Nuclear Reactor Thermal Hydraulics (NURETH-16)*, Chicago, IL, 2015.

[12] M. N. Avramova. *Development of an Innovative Spacer Grid Model Utilizing Computational Fluid Dynamics within a Subchannel Analysis Tool*. PhD thesis, Pennsylvania State University, 2007. https://etda.libraries.psu.edu/files/final_submissions/4270.

[13] M. N. Avramova, R. K. Salko, et al. CTF theory manual. Technical Report CASL-U-2017-1263-000, CASL/NCSU, January 2017.

[14] N. Balakrishnan. A simple application of binomial–negative binomial relationship in the derivation of sharp bounds for moments of order statistics based on greatest convex minorants. *Stat. Probab. Lett.*, 18(4):301–305, November 1993. https://doi.org/10.1016/0167-7152(93)90019-F.

[15] J. L. Bates. High-temperature thermal conductivity of "round robin in" uranium dioxide. Technical Report BNWL-1431, Pacific Northwest National Laboratories, July 1970. https://www.osti.gov/servlets/purl/4084378.

[16] G. G. Botte, J. A. Ritter, and R. E. White. Comparison of finite difference and control volume methods for solving differential equations. *Comput. Chem. Eng.*, 24(12):2633–2654, 2000. https://doi.org/10.1016/S0098-1354(00)00619-0.

[17] M. J. Boussinesq. Calcul du pouvoir refroidissant des courants fluids (Calculation of the cooling power of a fluid stream). *Journal de Mathématiques Pures et Appliquées (Journal of Pure and Applied Mathematics)*, 1:310, 1905.

[18] S. P. Brooks and A. Gelman. General methods for monitoring convergence of iterative simulations. *J. Comput. Graph. Stat.*, 7(4):432–455, December 1998. https://doi.org/10.2307/1390675.

[19] G. G. Brucker and E. M. Sparrow. Direct contact condensation of steam bubbles in water at high pressure. *Int. J. Heat Mass Transfer*, 20:371–381, 1977. https://doi.org/10.1016/0017-9310(77)90158-2.

[20] C. J. Burns and D. L. Aumiller. COBRA-IE evaluation by simulation of the NUPEC BWR full-size fine-mesh bundle test BFBT. Technical Report B-T-3653, Bechtel Bettis, Inc., 2007.

[21] CD-adapco. *CCM User Guide: STAR-CD version 4.02*, 2006.

[22] M. R. Chernick. *Bootstrap Methods: A Guide for Practitioners and Researchers*. John Wiley and Sons, Newtown, PA, second edition, 2008.

[23] S. W. Churchill. Empirical expressions for the shear stress in turbulent flow in commercial pipes. *AIChE J.*, 19(2):375–376, March 1973. https://doi.org/10.1002/aic.690190228.

[24] S. W. Churchill. Friction-factor equation spans all fluid-flow regimes. *Chem. Eng. J.*, 84:91–92, 1977.

[25] A. P. Colburn. A method of correlating forced convection heat transfer data and a comparison with fluid friction. *Trans. Am. Inst. Chem. Eng.*, 29:174–210, 1933. https://doi.org/10.1016/0017-9310(64)90125-5.

[26] C. F. Colebrook. Turbulent flow in pipes, with particular reference to the transition region between the smooth and rough pipe laws. *J. Inst. Civ. Eng. London*, 11(5204):133–156, 1939. https://doi.org/10.1680/ijoti.1939.13150.

[27] C. F. Colebrook and C. M. White. Experiments with fluid friction in roughened pipes. *Proc. Royal Soc. London. Series A, Mathematical and Physical Sciences*, 161(906):167–381, August 1937. http://doi.org/10.1098/rspa.1937.0150.

[28] R. Cournat, K. Friedrichs, and H. Lewy. Über die partiellen differenzengleichungen der mathematischen physik (On the partial difference equations of mathematical physics). *Mathematische Annalen*, 100(1):32–74, 1928. https://doi.org/10.1007/BF01448839.

[29] J. M. Cuta et al. *VIPRE-01: A Thermal Hydraulic Code for Reactor Cores*, August 1989.

[30] C. A. Dances. Initial residual formulation of CTF. Master's thesis, Pennsylvania State University, May 2015. https://etda.libraries.psu.edu/files/final_submissions/10698.

[31] C. A. Dances, M. N. Avramova, and V. A. Mousseau. Initial one-dimensional (1-D) single phase liquid verification of CTF. Technical Report CASL-U-2015-0182-000, CASL, April 2015.

[32] C. A. Dances and V. A. Mousseau. Preliminary residual formulation of COBRA-TF. In D. P. Kouri and M. L. Parks, editors, *Center for Computing Research Summer Proceedings*, number SAND2015-38290, pages 105–124. SNL, December 2014.

[33] C. A. Dances, V. A. Mousseau, and M. N. Avramova. CTF residual formulation of solid liquid coupling. In *Proceedings of the 16th International Topical Meeting on Nuclear Reactor Thermal Hydraulics (NURETH-16)*, Chicago, IL, September 2014.

[34] F. D'Auria and A. Petruzzi. Background and qualification of uncertainty methods. In *Seminar on the Transfer of Knowledge Gained through CSNI Activities in the Field of Thermal-Hydraulics (THICKET-2008)*, Pisa, Italy, May 2008.

[35] H. A. David and H. N. Nagaraja. *Order Statistics*. John Wiley & Sons, Inc., Hoboken, NJ, third edition, 2003.

[36] R. G. Deissler and C. S. Eian. Analytical and experimental investigation of fully developed turbulent flow of air in a smooth tube with heat transfer with variable fluid properties. Technical Report NACA-TN-2629, NACA, Cleveland, OH, 1952.

[37] D. R. Dickinson. Tests of the effect of scale build-up on heat transfer using untreated water under conditions typical of the ETS-1 exhaust duct. Technical Report BNWL-632, PNNL, March 1968. https://www.osti.gov/servlets/purl/4546183.

[38] F. W. Dittus and L. M. K. Boelter. Heat transfer in automobile radiators of the tubular type. In *Publications in Engineering 2*, pages 443–461. University of California, Berkeley, 1930. https://doi.org/10.1016/0735-1933(85)90003-X.

[39] M. Everts and J. P. Meyer. Relationship between pressure drop and heat transfer of developing and fully developed flow in smooth horizontal circular tubes in the laminar, transitional, quasi-turbulent and turbulent flow regimes. *Int. J. Heat Mass Transfer*, 117:1231–1250, November 2017. https://doi.org/10.1016/j.ijheatmasstransfer.2017.10.072.

[40] C. Eymard. *CATHARE2 V2.5 User Manual*. Alternative Energies and Atomic Energy Commission (CEA), Grenoble, France, 2005.

[41] G. Fayl and K. Hansen. In-reactor determination of the thermal conductivity of UO_2-pellets up to 2200°C. Technical Report Risø 269, Danish Atomic Energy Commission, July 1972.

[42] J. H. Ferziger and M. Perić. *Computational Methods for Fluid Dynamics*. Springer, Berlin, Germany, third edition, 2002.

[43] L. Frate, F. Moretti, G. Galassi, and F. D'Auria. Limitations in the use of the equivalent diameter. *World J. Nucl. Sci. Tech.*, 6(1), January 2016. http://doi.org/10.4236/wjnst.2016.61005.

[44] N. Frössling. On the evaporation of falling drops. *Gerlands Beitrage zur Geophysik*, 52:107–216, 1938.

[45] S. Fukushima et al. The effect of gadolinium content on the thermal conductivity of near-stoichiometric (U,Gd)O_2 solid solutions. *J. Nucl. Mater.*, 105(2–3):201–210, February 1982. https://doi.org/10.1016/0022-3115(82)90375-0.

[46] N. Furuichi et al. Friction factor and mean velocity profile for pipe flow at high Reynolds numbers. *Phys. Fluids*, 27(9), September 2015. https://doi.org/10.1063/1.4930987.

[47] R. O. Gauntt et al. *MELCOR Computer Code Manuals: Primer and User's Guide Version 1.8.5*. NRC, December 2000.

[48] A. Gelman and D. B. Rubin. Inference from iterative simulation using multiple sequences. *Stat. Sci.*, 7(4):457–511, 1992. https://projecteuclid.org/euclid.ss/1177011136.

[49] R. L. Gibby. The effect of plutonium content on the thermal conductivity of (U,Pu)O_2 solid solutions. *J. Nucl. Mater.*, 38(2):163–177, February 1971. https://doi.org/10.1016/0022-3115(71)90040-7.

[50] H. Glaeser. GRS method for uncertainty and sensitivity evaluation of code results and applications. *Sci. and Tech. of Nuc. Inst.*, 2008, February 2008. http://doi.org/10.1155/2008/798901.

[51] V. Gnielinski. New equations for heat and mass transfer in turbulent pipe and channel flow. *Int. J. Chem. Eng.*, 16:359–368, 1976.

[52] T. G. Godfrey et al. Thermal conductivity of uranium dioxide and ARMCO Iron by an improved radial heat flow technique. Technical Report ORNL-3556, ORNL, June 1964.

[53] L. A. Goldsmith and J. A. M. Douglas. Measurements of the thermal conductivity of uranium dioxide at 670-1270 K. *J. Nucl. Mater.*, 47(1):31–42, May 1973. https://doi.org/10.1016/0022-3115(73)90183-9.

[54] P. Griffith and G. B. Wallis. Two-phase slug flow. *J. Heat Transfer*, 83:307–320, 1961. https://doi.org/10.1115/1.3682268.

[55] P. A. Griffith and G. A. Snyder. The bubbly-slug transition in high velocity two-phase flow. Technical Report TID-20947, MIT, July 1964.

[56] E. J. Gumbel. The maxima of the mean largest value and the range. *Ann. Math. Statist.*, 25:76–84, 1954. https://projecteuclid.org/euclid.aoms/1177728847.

[57] H. Haario, M. Laine, A. Mira, and E. Saksman. DRAM: Efficient adaptive MCMC. *Stat. Comput.*, 16(4):339–354, June 2006. https://doi.org/10.1007/s11222-006-9438-0.

[58] H. Haario, E. Saksman, and J. Tamminen. An adapative metropolis algorithm. *Bernoulli*, 7(2):223–242, 2001. https://projecteuclid.org/euclid.bj/1080222083.

[59] D. T. Hagrman et al. MATPRO–A library of materials properties for light-water-reactor accident analysis. Technical Report NUREG/CR-6150/EGG-2720, NRC/INL, June 1995.

[60] F. H. Harlow and J. E. Welsh. Numerical calculation of time dependent viscous incompressible flow with free surface. *Phys. Fluids*, 8:2182–2189, 1965. https://doi.org/10.1063/1.1761178.

[61] P. Harriott and R. M. Hamilton. Solid-liquid mass transfer in turbulent pipe flow. *Chem. Eng. Sci.*, 20(12):1073–1078, December 1965. https://doi.org/10.1016/0009-2509(65)80110-5.

[62] H. O. Hartley and H. A. David. Universal bounds for mean range and extreme observations. *Ann. Math. Statist.*, 25(1):85–99, 1954. https://projecteuclid.org/euclid.aoms/1177728848.

[63] W. H. Henstock and T. J. Hanratty. The interfacial drag and the height of the wall layer in annular flows. *AIChE J.*, 22(6):990–1000, 1976. https://doi.org/10.1002/aic.690220607.

[64] M. Hirai. Thermal diffusivity of UO_2–Gd_2O_3 pellets. *J. Nucl. Mater.*, 173(3):247–254, October 1990. https://doi.org/10.1016/0022-3115(90)90392-Z.

[65] C. W. Hirt. Heuristic stability theory for finite-difference equations. *J. Comput. Phys.*, 2:339–355, 1968. https://doi.org/10.1016/0021-9991(68)90041-7.

[66] I. C. Hobson, R. Raylor, and J. B. Ainscough. Effect of porosity and stoichiometry on the thermal conductivity of uranium dioxide. *J. Phys. D: Applied Physics*, 7(7):1003–1016, 1974. http://doi.org/10.1088/0022-3727/7/7/308.

[67] E. Hofer. The GRS programme package for uncertainty and sensitivity analysis. In *Proceedings of the Seminar on Methods and Codes for Assessing the Off-Site Consequences of Nuclear Accidents*, Athens, Greece, May 1991.

[68] I. S. Hong, D. Y Oh, and I. G. Kim. Generic application of Wilks' tolerance limit evaluation approach to nuclear safety. In *OECD/CSNI Workshop on Best Estimate Methods and Uncertainty Evaluations*, number NEA/CSNI/R(2013)8, pages 16–25, Barcelona, Spain, November 2013.

[69] J. Hou et al. Benchmark for Uncertainty Analysis in Modeling (UAM) for design, operation and safety analysis of LWRs, Volume II: specification and support data for core cases. Technical report, OECD/NEA, April 2017.

[70] J. S. Huang. Sharp bounds for the expected value of order statistics. *Stat. Probab. Lett.*, 33(1):105–107, April 1997. https://doi.org/10.1016/S0167-7152(96)00116-2.

[71] G. A. Hughmark. Film thickness, entrainment, and pressure drop in upward annular and dispersed flow. *AIChE J.*, 19(5):1062–1065, September 1973. https://doi.org/10.1002/aic.690190533.

[72] H. Ikeda, T. Kikuchi, and S. Ono. Improvements of the FPAC code. In *Nuclear Fuel Behaviour Modelling at High Burnup and Its Experimental Support*, pages 277–290, Windermere, UK, June 2000.

[73] U. Imke, V. Sanchez, and R. Gomez. SUBCHANFLOW: An empirical knowledge based subchannel code. In *Proceedings of the Annual Meeting on Nuclear Technology*, pages 4–6, Berlin, Germany, May 2010.

[74] J. Isenberg and S. Sideman. Direct contact heat transfer with change of phase: Bubble condensation in immiscible liquids. *Int. J. Heat Mass Transfer*, 13(6):997–1011, 1970. https://doi.org/10.1016/0017-9310(70)90166-3.

[75] M. Ishii. Inception criteria for droplet entrainment in two-phase concurrent film flow. *AIChE J.*, 21(2):308–318, March 1975. https://doi.org/10.1002/aic.690210212.

[76] M. Ishii and K. Mishima. Study of two-fluid model and interfacial area. Technical Report NUREG/CR-1873, ANL-80-111, ANL, December 1980.

[77] H. F. Johnstone, R. L. Pigford, and J. H. Chapin. Heat transfer to clouds of falling particles. Technical Report 43, University of Illinois Urbana, 1941.

[78] K. R. Katsma et al. Quantifying reactor safety margins: Application of CSAU evaluation methodology to a large-break LOCA. Technical Report NUREG/CR-5249, Nuclear Regulatory Commission, December 1989.

[79] W. M. Kays and E. Y. Leung. Heat transfer in annular passages–hydrodynamically developed turbulent flow with arbitrarily prescribed heat flux. *Int. J. Heat Mass Transfer*, 6(7):537–557, July 1963. https://doi.org/10.1016/0017-9310(63)90012-7.

[80] C. T. Kelley. *Iterative Methods for Linear and Nonlinear Equations*. SIAM, Philadelphia, PA, 1995.

[81] J. E. Kelly, S. P. Kao, and M. S. Kazimi. User's guide for THERMIT-2: a version of THERMIT for both core-wide and subchannel analysis of light water reactors. Technical Report MIT-EL-81-029, MIT, August 1981.

[82] M. C. Kennedy and A. O'Hagan. Bayesian calibration of computer models. *J. Royal Stat. Soc.*, 63(3):425–464, January 2001. https://doi.org/10.1111/1467-9868.00294.

[83] E. C. Koo. *Mechanisms of Isothermal and Non-Isothermal Flow of Fluids in Pipes*. PhD thesis, MIT, 1932.

[84] P. K. Kundu and I. M. Cohen. *Fluid Mechanics*. Academic Press, Waltham, MA, fifth edition, 2012.

[85] M. Laine. MCMC toolbox for Matlab, 2017. `http://helios.fmi.fi/~lainema/mcmc/`.

[86] D. D. Lanning, C. E. Beyer, and K. J. Geelhood. FRAPCON-3 updates, including mixed-oxide fuel properties. Technical Report NUREG/CR-6534, Vol. 4, PNNL-11513, NRC/PNNL, May 2005.

[87] A. E. Lawrence and T. K. Sherwood. Heat transmission to water flowing in pipes. *Ind. Eng. Chem.*, 23(3):301–309, March 1931. `http://doi.org/10.1021/ie50255a023`.

[88] K. Lee and D. J. Ryley. The evaporation of water droplets in superheated steam. *J. Heat Transfer*, 90:445–451, November 1968. `https://doi.org/10.1115/1.3597540`.

[89] E. Y. Leung, W. M. Kays, and W. C. Reynolds. Heat transfer with turbulent flow in concentric and eccentric annuli with constant and variable heat flux. Technical Report TR AHT-4, Standord University, Standford, CA, 1962.

[90] D. R. Liles and W. H. Reed. A semi-implicit method for two-phase fluid dynamics. *J. Comput. Phys.*, 26(3):390–407, 1978. `https://doi.org/10.1016/0021-9991(78)90077-3`.

[91] L. J. Lloyd. *Development of Spatially-Selective, Nonlinear Refinement Algorithm for Thermal-Hydraulic Safety Analysis*. PhD thesis, University of Wisconsin-Madison, 2014.

[92] A. L. Loeb. Thermal conductivity: VIII, a theory of thermal conductivity of porous materials. *J. Am. Ceram. Soc.*, 37(2), February 1954. `https://doi.org/10.1111/j.1551-2916.1954.tb20107.x`.

[93] C. F. Lucks and H. W. Deem. Thermal conductivity and electrical conductivity of UO_2. Technical Report BMI-1448, Battelle Memorial Institute, July 1960.

[94] P. G. Lucuta, H. J. Matxke, R. A. Verrall, and H. A. Tasman. Thermal conductivity of SIM-FUEL. *J. Nucl. Mat.*, 188:198–204, June 1992. `https://doi.org/10.1016/0022-3115(92)90471-V`.

[95] O. Ludwig. Differenzen der Erwartungswerte von Ranggrössen in kleinen Stichproben (Ranges of expected values of order statistics in small samples). In *Proceedings of the Fourth Conference on Probability Theory*, Brasov, Romania, September 1973.

[96] J. H. Mahaffy. A stability-enhancing two-step method for fluid flow calculations. *J. Comput. Phys.*, 46(3):329–341, 1982. `https://doi.org/10.1016/0021-9991(82)90019-5`.

[97] J. A. Malina and E. M. Sparrow. Variable-property, constant-property, and entrance-region heat transfer results for turbulent flow of water and oil in a circular tube. *Chem. Eng. Sci.*, 19(12):953–962, December 1964. `https://doi.org/10.1016/0009-2509(64)85102-2`.

[98] R. P. Martin and L. D. O'Dell. AREVA's realistic large break LOCA analysis methodology. *Nucl. Eng. Des.*, 235:1713–1725, 2005. http://doi.org/10.1016/j.nucengdes.2005.02.004.

[99] A. R. Massih, S. Persson, and Z. Weiss. Modelling of (U,Gd)O_2 fuel behaviour in boiling water reactors. *J. Nucl. Mater.*, 188:323–330, June 1992. https://doi.org/10.1016/0022-3115(92)90492-4.

[100] Mathworks. *nlmefit*. http://www.mathworks.com/help/stats/nlmefit.html.

[101] K. Maupin, L. Swiler, and N. W. Porter. Validation metrics for deterministic and probabilistic data. *ASME Journal of Verification, Validation and Uncertainty Quantification*, 2018. Accepted for publication.

[102] K. A. Maupin and L. P. Swiler. Validation metrics for deterministic and probabilistic data. Technical Report SAND2016-1421, SNL, January 2017.

[103] W. H. McAdams. *Heat Transmission*. McGraw-Hill Book Company, New York, NY, third edition, 1954.

[104] D. M. McEligot. *Effect of Large Temperature Gradients on Turbulent Flow of Gases in the Downstream Region of Tubes*. PhD thesis, Stanford University, April 1963.

[105] D. M. McEligot, L. W. Ormand, and H. C. Perkins. Internal low Reynolds-number turbulent and transitional gas flow with heat transfer. *J. Heat Transfer*, 88(2):239–245, May 1966. http://doi.org/10.1115/1.3691521.

[106] B. J. McKeon et al. Friction factors for smooth pipe flow. *J. Fluid Mech.*, 511:41–44, April 2004.

[107] A. Mira. On Metropolis-Hastings algorithm with delayed rejection. *Metron*, 59(3):231–241, 2001.

[108] D. Moalem and S. Sideman. The effect of motion on bubble collapse. *Int. J. Heat Mass Transfer*, 16(12):2321–2329, 1973. https://doi.org/10.1016/0017-9310(73)90017-3.

[109] L. F. Moody. Friction factors for pipe flow. *Trans. ASME*, 66(8):671–684, 1944.

[110] A. Moorthi, A. K. Sharma, and K. Velusamy. A review of sub-channel thermal hydraulic codes for nuclear reactor core and future directions. *Nucl. Eng. Des.*, 332:329–344, June 2018. https://doi.org/10.1016/j.nucengdes.2018.03.012.

[111] S. Moriguti. Extremal properties of extreme value distributions. *Ann. Math. Statist.*, 22(4):523–536, December 1951. https://projecteuclid.org/euclid.aoms/1177729542.

[112] S. Moriguti. A modification of schwarz's inequality with applications to distributions. *Ann. Math. Statist.*, 24(1):107–113, November 1953. https://projecteuclid.org/euclid.aoms/1177729088.

[113] F. H. Morris and W. G. Whitman. Heat transfer for oils and water in pipes. *Ind. Eng. Chem.*, 20(3):234–240, March 1928. http://doi.org/10.1021/ie50219a007.

[114] V. A. Mousseau et al. Demonstration of integrated DA/UQ for VERA-CS on a core physics progression problem. Technical Report CASL-I-2014-0158-000, CASL, 2014.

[115] V. A. Mousseau and B. J. Williams. Uncertainty quantification in a regulatory environment. In R. Ghanem, D. Higdon, and H. Owhadi, editors, *Handbook of Uncertainty Quantification*. Springer International, Switzerland, 2017.

[116] J. Nakamura et al. Thermal diffusivity of high burnup UO_2 pellet. In *Advances in Fuel Pellet Technology for Improved Performance at High Burnup*, pages 127–138, Tokyo, Japan, October 1996.

[117] B. Neykov et al. NUPEC BWR full-size fine-mesh bundle test (BFBT) benchmark. Technical Report NEA No. 6212, OECD NEA, 2006.

[118] J. Nikuradse. Laws of flow in rough pipes. Technical Report TT359, NACA, November 1966. Translation of "Gesetzmässingkeiten der turbulenten Stromung in Glatten Rohren," *Verein Deutcher Ingenieure-Forschungshelft,* **361**, *4*, (1933).

[119] J. Nikuradse. Laws of turbulent flow in smooth pipes. Technical Report TT 359, NACA, October 1966. Translation of Gesetzmässingkeiten der turbulenten Stromung in Glatten Rohren. *Verein Deutscher Ingenieure-Forschungshelft*, 356(3), October 1932.

[120] M. E. Nissley. Realistic large-break LOCA evaluation methodology using the automated statistical treatment of uncertainty method (ASTRUM). Technical Report WCAP-1 60090-P, Westinghouse, 2003.

[121] W. L. Oberkampf, M. Pilch, and T. G. Trucano. Predictive capability maturity model for computational modeling and simulation. Technical Report SAND2007-5948, SNL, October 2007.

[122] W. L. Oberkampf and C. J. Roy. *Verification and Validation in Scientific Computing*. Cambridge University Press, Cambridge, UK, first edition, November 2010.

[123] K. Ohira and N. Itagaki. Thermal conductivity measurements of high burnup UO_2 pellet and a benchmark calculation of fuel center temperature. In *Proceedings of the ANS International Topical Meeting on LWR Fuel Performance*, pages 541–549, Portland, OR, March 1997.

[124] L. Pál and M. Makai. Statistical considerations on safety analysis. In *Proceedings of the International Meeting on Updates in Best Estimate Methods*, Washington, D.C., November 2003.

[125] L. Pál and M. Makai. Remarks on statistical aspects of safety analysis of complex systems. *Reliab. Eng. Syst. Saf.*, 80, 2004.

[126] N. Papadatos. Maximum variance of order statistics. *Ann. Inst. Stat. Math.*, 47(1):185–193, 1995. https://doi.org/10.1007/BF00773423.

[127] S. V. Patankar. *Numerical Heat Transfer and Fluid Flow*. Hemisphere Pub. Corp., Washington, D.C., 1980.

[128] V. C. Patel and M. R. Head. Some observations on skin friction and velocity profiles in fully developed pipe and channel flows. *J. Fluid. Mech.*, 38(1):181–201, August 1969. https://doi.org/10.1017/S0022112069000115.

[129] Y. Périn, T. Blyth, M. N. Avramova, and K. Velkov. Uncertainty analysis of CTF prediction of moderator and fuel parameters for the OECD LWR UAM Benchmark, exercise II-3: "bundle thermal-hydraulics", using the SUSA tool. In *Proceedings of the 15th International Topical Meeting on Nuclear Reactor Thermal Hydraulics (NURETH-15)*, Pisa, Italy, May 2013.

[130] M. S. Plesset and S. A. Zwick. The growth of vapor bubbles in superheated liquids. *J. Appl. Phys.*, 25(4):493–500, 1954. https://doi.org/10.1063/1.1721668.

[131] J. L. M. Poiseuille. Recherches expérimentales sur le mouvement des liquides dans les tubes de trs-petits diamtres (Experimental research on the movement of liquids in tubes of very small diameters). *Comptes Rendus, Acadmie des Sciences*, 1841.

[132] N. Porter, V. Mousseau, and M. Avramova. Solution verification of CTF and CTF-R using isokinetic advection test problems. In *International Conference on Mathematics and Computational Methods Applied to Nuclear Science and Engineering (M&C-2017)*, Jeju, Korea, April 2017.

[133] N. W. Porter and M. N. Avramova. Validation of CTF pressure drop and void predictions for the NUPEC BWR database. *Nucl. Eng. Des.*, 337:291–299, July 2018. https://doi.org/10.1016/j.nucengdes.2018.07.018.

[134] N. W. Porter, M. N. Avramova, and V. A. Mousseau. Uncertainty quantification study of CTF for the OECD/NEA LWR Uncertainty Analysis in Modeling Benchmark. *Nucl. Sci. Eng.*, 190(3):271–286, January 2018. https://doi.org/10.1080/00295639.2018.1435135.

[135] N. W. Porter, V. A. Mousseau, and M. N. Avramova. Initial residual formulation of CTF for one dimensional, single phase flow. Technical Report CASL-U-2016-1183-000, CASL, August 2016.

[136] N. W. Porter, V. A. Mousseau, and M. N. Avramova. CTF-R manual. Technical Report CASL-U-2017-1414-000, CASL, August 2017.

[137] N. W. Porter, V. A. Mousseau, and M. N. Avramova. Common uncertainty quantification assumptions: A critical analysis and application to convective heat transfer. In *Proceedings of the ANS Best Estimate Plus Uncertainty International Conference (BEPU 2018)*, Lucca, Italy, May 2018.

[138] N. W. Porter, V. A. Mousseau, and M. N. Avramova. Demonstration of VVUQ with CTF and development of CTF-R. Technical Report CASL-U-2018-1655-000, CASL, August 2018.

[139] N. W. Porter, V. A. Mousseau, and M. N. Avramova. Quantified validation with uncertainty analysis for turbulent single phase friction models. In *Proceedings of the ANS Best Estimate Plus Uncertainty International Conference (BEPU 2018)*, Lucca, Italy, May 2018.

[140] N. A. Radovich and R. Moissis. The transition from two-phase bubble flow to slug flow. Technical Report 7-7673-22, MIT, 1962.

[141] H. E. Robbins. On the measure of a random set. *Ann. Math. Statist.*, 15(1):70–74, 1944. https://projecteuclid.org/euclid.aoms/1177731315.

[142] C. Ronchi et al. Thermal conductivity of uranium dioxide up to 2900 K from simultaneous measurement of the heat capacity and thermal diffusivity. *J. Appl. Phys.*, 85(2):776–789, 1999. https://doi.org/10.1063/1.369159.

[143] C. Ronchi et al. Effect of burn-up on the thermal conductivity of uranium dioxide up to 100 $MWdt^{-1}$. *J. Nucl. Mater.*, 327:58–76, 2004. https://doi.org/10.1016/j.jnucmat.2004.01.018.

[144] C. J. Roy et al. Discretization error estimation and exact solution generation using the method of nearby problems. Technical Report SAND2011-7118, Sandia National Laboratory, October 2011.

[145] A. Rubin et al. OECD/NRC benchmark based on NUPEC PWR Subchannel and Bundle Tests (PSBT). Technical report, NRC/OECD NEA, 2010.

[146] Y. Saad and M. H. Schultz. GMRES: a generalized minimal residual algorithm for solving nonsymmetric linear systems. *SIAM J. Sci. and Stat. Comput.*, 7(3), November 1983. https://doi.org/10.1137/0907058.

[147] K. Salari and P. Knupp. Code verification by the method of manufactured solutions. Technical Report SAND2000-1444, SNL, June 2000.

[148] R. K. Salko, M. N. Avramova, et al. CTF user's manual. Technical Report CASL-U-2017-1262-000, CASL/NCSU, January 2017.

[149] R. K. Salko, M. N. Avramova, et al. CTF validation and verification. Technical Report CASL-U-2017-1264-000, CASL/NCSU, January 2017.

[150] H. Schlichting and K. Gersten. *Boundary Layer Theory*. Springer, Berlin, Germany, 1982.

[151] K. L. Schmidt. *Uncertainty Quantification for Mixed-Effects Models with Applications in Nuclear Engineering*. PhD thesis, NCSU, 2016. http://www.lib.ncsu.edu/resolver/1840.16/11368.

[152] T. K. Sherwood and J. M. Petrie. Heat transmission to liquids flowing in pipes. *Ind. Eng. Chem.*, 24(7):736–745, July 1932. http://doi.org/10.1021/ie50271a005.

[153] W. A. Shewhart. Statistical method from the viewpoint of quality control. Technical report, U.S. Department of Agriculture, Washington, D.C., 1939.

[154] L. J. Siefken et al. SCDAP/RELAP5/MOD 3.3 code manual: MATPRO - a library of material properties for light-water-reactor accident analysis. Technical Report NUREG/CR-6150, INL/NRC, January 2001.

[155] C. A. Sleicher and M. W. Rouse. A convenient correlation for heat transfer to constant and variable property fluids in turbulent pipe flow. *Int. J. Heat Mass Transfer*, 18(5):677–683, May 1975. https://doi.org/10.1016/0017-9310(75)90279-3.

[156] R. C. Smith. *Uncertainty Quantification: Theory, Implementation, and Applications*. SIAM, first edition, 2014.

[157] E.M. Sparrow et al. Heat transfer to longitudinal laminar flow between cylinders. *J. Heat Transfer*, 83(4):415–422, November 1961. http://doi.org/10.1115/1.3683658.

[158] T. E. Stanton and J. R. Pannell. Similarity of motion in relation to the surface friction of fluids. *Phil. Trans. Royal Soc. London. Series A, Containing Papers of a Mathematical or Physical Character*, 214:199–224, 1914. http://doi.org/10.1098/rspa.1914.0063.

[159] J. P. Stora et al. Conductibilite thermique de l'oxyde d'uranium fritte dans les conditions d'utilisation en pile (Thermal conductivity of sintered uranium oxide under in-pile conditions). Technical Report EURAEC 1095, Commissariat a L'Energie Atomique, July 1964.

[160] C. J. Swanson et al. Pipe flow measurements over a wide range of Reynolds numbers using liquid helium and various gases. *J. Fluid. Mech.*, 461:51–60, June 2002. https://doi.org/10.1017/S0022112002008595.

[161] M. J. Thurgood et al. COBRA/TRAC: A thermal-hydraulics code for transient analysis of nuclear reactor vessels and primary coolant systems. Technical Report NUREG/CR-3046, PNL-4385, US Nuclear Regulatory Commission, 1983.

[162] N. E. Todreas and M. S. Kazimi. *Nuclear Systems Volume I: Thermal Hydraulic Fundamentals*. Taylor & Francis, Boca Raton, FL, second edition, 2012.

[163] A. Toptan, N. W. Porter, R. K. Salko, and M. N. Avramova. Implementation and assessment of wall friction models for LWR core analysis. *Ann. Nucl. Energy*, 115:565–572, February 2018. https://doi.org/10.1016/j.anucene.2018.02.022.

[164] A. Toptan, R. Salko, and M. N. Avramova. Fuel rod modeling in CTF: Incorporation of burnup dependent fuel thermal conductivity models and a review of CTF's dynamic gap conductance model. Technical Report CALS-U-2016-1181-000, CASL, August 2016.

[165] J. A. Trapp and R. A. Riemke. A nearly-implicit hydrodynamic numerical scheme for two-phase flows. *J. Comput. Phys.*, 66(1):62–82, 1986. https://doi.org/10.1016/0021-9991(86)90054-9.

[166] D. S. Trent and J. R. Welty. A summary of numerical methods for solving transient heat conduction problems. Technical Report 49, Engineering Experiment Station at Oregon State University, Corvallis, OR, 1974.

[167] T. G. Trucano et al. Calibration, validation, and sensitivity analysis: What's what. *Reliab. Eng. Syst. Saf.*, 91:1131–1357, 2006. https://doi.org/10.1016/j.ress.2005.11.031.

[168] A. Wald. An extension of Wilks' method for setting tolerance limits. *Ann. Math. Statist.*, 14:45–55, 1943. https://projecteuclid.org/euclid.aoms/1177731491.

[169] C. T. Walker et al. On the thermal conductivity of UO_2 nuclear fuel at a high burn-up of around 100 MWd/kgHM. *J. Nucl. Mater.*, 350:19–39, 2006. https://doi.org/10.1016/j.jnucmat.2005.11.007.

[170] G. B. Wallis. *One-Dimensional Two-Phase Flow*. McGraw-Hill, New York, NY, first edition, 1969.

[171] A. B. G. Washington. Preferred values for the thermal conductivity of sintered ceramic fuel for fast reactor use. Technical Report TRG 2236D, UK Atomic Energy Authority, Februrary 1973.

[172] J. C. Weilbacher. Diffusivite thermique de l'oxyde d'uranium et de l'oxyde de thorium a haute temperature (Thermal diffusivity of uranium dioxide and thorium dioxide at high temperature). *High Temp. Press.*, 4:431–438, 1972.

[173] S. S. Wilks. Determination of sample sizes for setting tolerance limits. *Ann. Math. Statist.*, 12(1):91–96, 1941. https://projecteuclid.org/euclid.aoms/1177731788.

[174] S. S. Wilks. Statistical prediction with special reference to the problem of tolerance limits. *Ann. Math. Statist.*, 13(4):400–409, 1942. https://projecteuclid.org/euclid.aoms/1177731537.

[175] S. S. Wilks. Order statistics. *Bull. Am. Math. Soc.*, 54(1):6–50, 1948. https://projecteuclid.org/euclid.bams/1183511502.

[176] R. H. S. Winterton. Where did the Dittus and Boelter equation come from? *Int. J. Heat Mass Transfer*, 41(4–5), June 1997.

[177] M. C. Yuen and L. W. Chen. Heat-transfer measurements of evaporating liquid droplets. *Int. J. Heat Mass Transfer*, 21:537–542, 1978. https://doi.org/10.1016/0017-9310(78)90049-2.

[178] M. V. Zagarola and A. J. Smits. Mean-flow scaling of turbulent pipe flow. *J. Fluid. Mech.*, 373:33–79, October 1998. https://doi.org/10.1017/S0022112098002419.

[179] D. J. Zigrang and N. D. Sylvester. Explicit approximations to the solution of Colebrook's friction factor equation. *AICHE J*, 28(3):514–515, May 1982. https://doi.org/10.1002/aic.690280323.

Appendices

APPENDIX

A

CONSERVATION EQUATION DERIVATIONS

This appendix outlines the derivation of conservation equations and source terms used in Section 4.2 for cases where their origin might not be clear. This includes the enthalpy, axial momentum, and lateral momentum equation.

A.1 Enthalpy Equation

This appendix contains a derivation of the enthalpy equation used in CTF and CTF-R. Begin with the one-dimensional form of the total energy conservation equation.

$$\frac{\partial \rho E}{\partial t} + \frac{\partial \rho u E}{\partial x} + \frac{\partial u P}{\partial x} + u \rho g = 0 \tag{A.1}$$

Total energy and enthalpy are defined as $E = e + u^2/2$ and $h = e + P/\rho$. Combining these definitions gives an equation for total energy in terms of enthalpy: $E = h - P/\rho + u^2/2$. This is substituted into Equation A.1 and then simplified.

$$\frac{\partial \rho h}{\partial t} - \frac{\partial P}{\partial t} + \frac{\partial \rho u h}{\partial x} + \frac{u^2}{2}\left(\frac{\partial \rho}{\partial t} + \frac{\partial \rho u}{\partial x}\right) + u\left(\rho \frac{\partial u}{\partial t} + \rho u \frac{\partial u}{\partial x} + \rho g\right) = 0 \tag{A.2}$$

Note that the terms in the large parentheses are the mass equation and the momentum equation, which are zero by definition.

$$\frac{\partial \rho h}{\partial t} + \frac{\partial \rho u h}{\partial x} - \frac{\partial P}{\partial t} - u\frac{\partial P}{\partial x} = 0 \tag{A.3}$$

This is consistent with the literature, where the conservation of enthalpy appears as $\frac{D\rho h}{Dt} = \frac{DP}{Dt}$ [84, 162]. The spatial derivative of pressure is neglected in CTF. It is possible to justify this assumption for steady state LWRs. A steady state version of Equation A.3 is integrated over the entire reactor.

$$\frac{\Delta\left(\rho u h\right)}{L} - \bar{u}\frac{\Delta P}{L} = 0 \tag{A.4}$$

The reactor length is L, and $\bar{u}$ is an average velocity. The general operating conditions of a typical BWR and PWR are used in Table A.1 to evaluate these terms.

Table A.1: Calculation of neglected terms in enthalpy equation. Operating conditions are taken from [162, Appendix K] for normal operating LWRs.

Description	Symbol	Units	BWR	PWR
Core pressure drop	ΔP	MPa	0.171	0.197
Flow rate per assembly	$\dot{m}$	kg/s	15.4	89.8
Flow area per assembly	A	m^2	0.0097	0.0244
Heated fuel height	L	m	3.588	3.658
Inlet pressure	P_{in}	MPa	7.14	15.51
Inlet density	ρ_{in}	kg/m^3	754.65	740.29
Inlet enthalpy	h_{in}	kJ/kg	1227.5	1300.6
Outlet density	ρ_{out}	kg/m^3	36.2	660.6
Outlet enthalpy	h_{out}	kJ/kg	2583.7	1473.3
First term in Eq. A.4	$\Delta\left(\rho u h\right)/L$	MPa/s	598.9	173.4
Second term in Eq. A.4	$\bar{u}\Delta P/L$	MPa/s	1.1	1.6

The neglected term is two orders of magnitude smaller than the other. This is sufficient to demonstrate that neglecting the pressure gradient term is accurate for steady state LWRs. It could be non-negligible for depressurization transients, dense working fluids, very strong frictional forces, strong gravity, or very high coolant velocities.

In CTF-R, the enthalpy equation is further simplified, where the chain rule is applied to two of the derivatives.

$$\rho\frac{\partial h}{\partial t} + h\frac{\partial \rho}{\partial t} + h\frac{\partial \rho u}{\partial x} + \rho u\frac{\partial h}{\partial x} - \frac{\partial P}{\partial t} = 0 \tag{A.5}$$

Then a mass equation is eliminated, yielding Equation 4.9 without the lateral terms.

$$\rho\frac{\partial h}{\partial t}+\rho u\frac{\partial h}{\partial x}+h\left(\frac{\partial \rho}{\partial t}+\frac{\partial \rho u}{\partial x}\right)-\frac{\partial P}{\partial t}=0 \tag{A.6}$$

$$\rho\frac{\partial h}{\partial t}+\rho u\frac{\partial h}{\partial x}-\frac{\partial P}{\partial t}=0 \tag{A.7}$$

An additional consideration is that the mass and momentum equation in Equation A.2 are only zero when there are no source terms in the conservation equations. Otherwise, the source terms in those equations should be carried through this derivation, which is not the case in CTF.

It is left as a future exercise to include the pressure gradient term in the energy equation and quantify the model form error introduced by neglecting it. The introduction of CTF-R (see Chapter 4) clearly enables an analysis such as this, where the addition of a term to a conservation equation is trivial. In the main version of CTF, this would require significant source codes changes and the recalculation of all analytical terms in the pressure matrix.

A.2 Axial Momentum Equation

The axial momentum conservation equation used in CTF-R is derived from the one-dimensional x-component of the three-dimensional momentum equations.

$$\frac{\partial \rho u}{\partial t}+\frac{\partial \rho u^2}{\partial x}+\frac{\partial P}{\partial x}-\rho g=0 \tag{A.8}$$

The first two derivatives are split using the chain rule.

$$\rho\frac{\partial u}{\partial t}+u\frac{\partial \rho}{\partial t}+\rho u\frac{\partial u}{\partial x}+u\frac{\partial \rho u}{\partial x}+\frac{\partial P}{\partial x}-\rho g=0 \tag{A.9}$$

The mass equation is eliminated, yielding Equation 4.12 without the lateral transfer or source term.

$$\frac{u}{\rho}\left(\frac{\partial \rho}{\partial t}+\frac{\partial \rho u}{\partial x}\right)+\frac{\partial u}{\partial t}+u\frac{\partial u}{\partial x}+\frac{1}{\rho}\frac{\partial P}{\partial x}-g=0 \tag{A.10}$$

$$\frac{\partial u}{\partial t}+u\frac{\partial u}{\partial x}+\frac{1}{\rho}\frac{\partial P}{\partial x}-g=0 \tag{A.11}$$

A.3 Lateral Momentum Equation

Flow in an LWR is primarily in the upwards direction, because of this assumption, the CTF and CTF-R momentum equations are simplified from a full three-dimensional form to a subchannel form. Though this reduces the number of equations to be solved, the underlying assumptions

are not immediately clear. To resolve this issue, the lateral momentum equation and associated source terms in the mass and energy equations are derived in this appendix.

The lateral momentum equation is derived from the three-dimensional momentum conservation equations with no source terms.

$$\frac{\partial \rho u}{\partial t} + \left[\frac{\partial \rho u^2}{\partial x} + \frac{\partial \rho v u}{\partial y} + \frac{\partial \rho w u}{\partial z}\right] = -\frac{\partial P}{\partial x} - \rho g \tag{A.12a}$$

$$\frac{\partial \rho v}{\partial t} + \left[\frac{\partial \rho u v}{\partial x} + \frac{\partial \rho v^2}{\partial y} + \frac{\partial \rho w v}{\partial z}\right] = -\frac{\partial P}{\partial y} \tag{A.12b}$$

$$\frac{\partial \rho w}{\partial t} + \left[\frac{\partial \rho u w}{\partial x} + \frac{\partial \rho v w}{\partial y} + \frac{\partial \rho w^2}{\partial z}\right] = -\frac{\partial P}{\partial z} \tag{A.12c}$$

As usual, u, v, and w are defined as the velocity components in the x, y, and z directions. The convective terms in the second two equations are neglected because $u >> v$ and $u >> w$.

$$\frac{\partial \rho u}{\partial t} + \left[\frac{\partial \rho u^2}{\partial x} + \frac{\partial \rho v u}{\partial y} + \frac{\partial \rho w u}{\partial z}\right] = -\frac{\partial P}{\partial x} - \rho g \tag{A.13a}$$

$$\frac{\partial \rho v}{\partial t} + \frac{\partial \rho u v}{\partial x} = -\frac{\partial P}{\partial y} \tag{A.13b}$$

$$\frac{\partial \rho w}{\partial t} + \frac{\partial \rho u w}{\partial x} = -\frac{\partial P}{\partial z} \tag{A.13c}$$

Neglecting both $\partial \rho v^2/\partial y$ and $\partial \rho w^2/\partial z$ physically means that momentum added to any control volume "losses its direction" after it is convected. Lateral momentum is not convected from above or below a lateral momentum cell, since $\partial \rho w v/\partial z$ and $\partial \rho w v/\partial z$ are negligible.

Now the equations are reformulated in terms of a unit vector parallel to any face of the scalar cell. For now, the direction of this unit vector is L. Redefined in this way, the y and z momentum equations are redundant. Velocity in the lateral direction is w, though this is not the same w as above.

$$\frac{\partial \rho u}{\partial t} + \left[\frac{\partial \rho u^2}{\partial x} + \frac{\partial \rho w u}{\partial y} + \frac{\partial \rho w u}{\partial z}\right] = -\frac{\partial P}{\partial x} - \rho g \tag{A.14a}$$

$$\frac{\partial \rho w}{\partial t} + \frac{\partial \rho u w}{\partial x} = -\frac{\partial P}{\partial L} \tag{A.14b}$$

Now the convection term in the x equation is simplified by partially discretizing it. Subscripts that are not noted are at i, j, or k.

$$\frac{\partial \rho v u}{\partial y} + \frac{\partial \rho w u}{\partial z} = \frac{(\rho u v)_{j+1/2} - (\rho u w)_{j-1/2}}{\Delta y} + \frac{(\rho u v)_{k+1/2} - (\rho u w)_{k-1/2}}{\Delta z} \tag{A.15a}$$

$$A\left(\frac{\partial \rho vu}{\partial y}+\frac{\partial \rho wu}{\partial z}\right)=\left[(\rho uv)_{j+1/2}-(\rho uv)_{j-1/2}\right]\Delta z+\left[(\rho uw)_{k+1/2}-(\rho uw)_{k-1/2}\right]\Delta y \quad \text{(A.15b)}$$

$$A\left(\frac{\partial \rho vu}{\partial y}+\frac{\partial \rho wu}{\partial z}\right)=(\rho uv)_{j+1/2}\Delta z-(\rho uv)_{j-1/2}\Delta z+(\rho uw)_{k+1/2}\Delta y-(\rho uw)_{k-1/2}\Delta y \quad \text{(A.15c)}$$

Each of terms on the right side correspond to a lateral face around the subchannel. This is notated as a summation over the faces in the CTF nomenclature.

$$\frac{\partial \rho vu}{\partial y}+\frac{\partial \rho wu}{\partial z}=\frac{1}{A}\sum_{g}^{n_g}(\rho wuS)_g \quad \text{(A.16)}$$

Here, A is the flow area of the channel, g indicates different gaps, and S is the gap width. Therefore, the axial and lateral momentum equations can be finalized.

$$\frac{\partial \rho u}{\partial t}+\frac{\partial \rho u^2}{\partial x}+\frac{1}{A}\sum_{g}^{n_g}(\rho wuS)_g=-\frac{\partial P}{\partial x}-\rho g \quad \text{(A.17a)}$$

$$\frac{\partial \rho w}{\partial t}+\frac{\partial \rho uw}{\partial x}=-\frac{\partial P}{\partial L} \quad \text{(A.17b)}$$

Note that the neglected terms could be included in the analysis, at which point the lateral momentum equation is more complicated [161].

$$\frac{\partial \rho w}{\partial t}+\frac{\partial \rho w^2}{\partial L}+\frac{\partial \rho uw}{\partial x}+\sum_{nk}\rho ww_{nk}S'_{nk}=-\frac{\partial P}{\partial L} \quad \text{(A.18)}$$

All gaps that convect momentum towards the current gap are indicated by nk, and S' is the corresponding orthogonal gap width.

The mass and energy source terms for the subchannel formulation are derived from their full three-dimensional forms. The conservation of mass equation is used as an example here.

$$\frac{\partial \rho}{\partial t}+\nabla\cdot(\rho\vec{v})=0 \quad \text{(A.19a)}$$

$$\frac{\partial \rho}{\partial t}+\frac{\partial \rho u}{\partial x}+\frac{\partial \rho v}{\partial y}+\frac{\partial \rho w}{\partial z}=0 \quad \text{(A.19b)}$$

Follow the same logic as in Equation A.15 to derive the mass source term.

$$\frac{\partial \rho v}{\partial y}+\frac{\partial \rho w}{\partial z}=\frac{1}{A}\sum_{g}^{n_g}(\rho wS)_g \quad \text{(A.20)}$$

It is also derived in the same way in the conservation of energy equation.

$$\frac{\partial \rho h v}{\partial y} + \frac{\partial \rho h w}{\partial z} = \frac{1}{A} \sum_{g}^{n_g} (\rho w h S)_g \tag{A.21}$$

APPENDIX

B

CTF PHASE CHANGE MODEL

In TH codes, many of the closure models are related to interfacial transfer. This appendix outlines the interfacial mass transfer model in CTF, which serves as an example of how esoteric the models in legacy codes can be. Much of the information in this appendix is not included in any of the CTF documentation [13, 148] and therefore was researched independently.

B.1 Flow Regime Map

Interfacial models are based on a flow regime map, which is used to select the appropriate correlations depending on parameters in each computational cell. For the interfacial mass transfer model, each regime is some combination of four different correlations: small bubble, large bubble, film, and droplet. The film and droplet correlations are always added together, yielding the annular-mist correlations.

B.1.1 Normal Flow Regimes

When the solid structures are cool enough to be continuously wetted, normal flow regimes are used. The normal flow map has four regimes, the selection of which depends only on the void fraction, α. The combination of the three correlations into the four flow regimes is shown in Figure B.1.

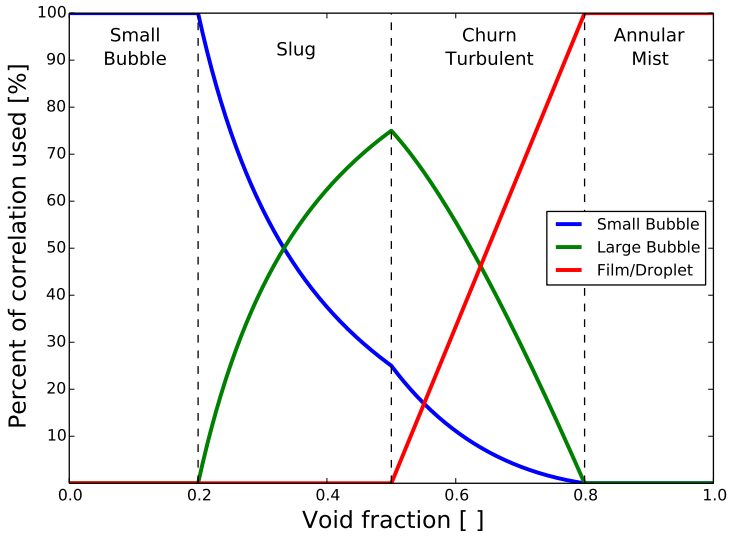

Figure B.1: The CTF flow regime map. There are four flow regimes in CTF which are each a combination of four correlations.

Small Bubble The small bubble regime consists of small steam bubbles dispersed in the continuous liquid water. The regime exists when $0.0 < \alpha < 0.2$, where suggestions for the upper range have varied from 0.18 to 0.3 in the literature [54, 55, 140]. Above the 0.2 threshold, the small bubbles begin to coalesce and form larger bubbles.

Slug The slug regime is used for void fractions $0.2 < \alpha < 0.5$. Slug flow contains bubbles of varying sizes separated by liquid slugs. In CTF, slug flow is modeled as a nonlinear combination of the small and large bubble correlations.

$$H_{i,slug} = F_{slug} H_{sb} + (1 - F_{slug}) H_{lb} \tag{B.1a}$$

$$F_{slug} = \frac{0.2(1-\alpha)}{0.8\alpha} \tag{B.1b}$$

The factor, F_{slug} is 1 when $\alpha = 0.2$ and is 0 when $\alpha = 1$. The lower limit of the slug regime uses only small bubble correlations. The upper limit of the regime uses 75% of the large bubble correlations and 25% of the small bubble correlations.

Churn-Turbulent The churn-turbulent regime exists for void fractions $0.5 < \alpha < 0.8$. It is characterized by agitated flow with unique behaviors. The film/droplet correlations are added linearly to the slug correlations in this regime.

$$H_{i,ann} = F_{ann} H_{ann} + (1 - F_{ann}) H_{slug} \tag{B.2a}$$

$$F_{ann} = \frac{\alpha - 0.5}{0.3} \tag{B.2b}$$

When $\alpha = 0.5$, only the slug correlations are used, but when $\alpha = 0.8$ only the film/droplet correlations are used.

Annular/Mist The annular/mist flow regime is characterized by a continuous vapor core surrounded by a liquid film with entrained droplets. It exists above a void fraction of 0.8 and is a direct combination of the film and droplet correlations.

B.1.2 Hot Wall Regimes

When the surface of a rod is too hot to be wetted by the continuous liquid, a vapor blanket can form. This is detrimental to reactor safety because steam has a lower heat transfer capability than liquid water. The hot wall regimes are used when the rod surface is too hot.

$$T_w > \min\left(705.3,\, T_{sat} + 75\right)\ ^\circ F \tag{B.3}$$

The critical heat flux temperature is approximated as $T_{sat} + 75$, above which the heat flux at the surface will immediately vaporize any water in contact with the wall. The other limit corresponds to the critical temperature of water, above which the vapor on the surface of the wall cannot be condensed regardless of the pressure.

There are three hot wall flow regimes: bottom reflood, falling film, and top deluge. Each regime uses different interfacial area and drag models for the film, which are added to the droplet coefficients. If the liquid void fraction is very small, the model is approximately dispersed droplet flow.

Bottom Reflood If a hot wall exists in the current cell and also in the cell above, the bottom reflood correlations are used. This can be thought of as an inverted annular or inverted slug regime, where the rod is unwetted and there exists some amount of continuous liquid in the core of the subchannel.

Falling Film If there is a top quench front, meaning that the cell below has a hot wall but the cell above does not, the falling film correlations are used. This option is selected if $\alpha \geq 0.8$. This models a liquid film flowing down with a vapor core flowing upwards.

Top Deluge If a top quench front exists and $\alpha < 0.8$, the top deluge regime is selected. This regime models large liquid slugs, with a diameter equal to the hydraulic diameter of the channel, which are falling downwards.

Dispersed Droplet If the liquid fraction is very small, the contributions from the previous hot wall regimes are negligible. In this case, the flow will essentially be single phase vapor with a dispersed droplet field.

B.1.3 Discussion

Most TH codes use one correlation for each flow regime with interpolation between them. This allows thorough investigation of each correlation, where experimental uncertainty is directly related to code uncertainty. Instead, CTF combines multiple correlations for each flow regime, which adds model form error. The uncertainty and range of applicability for each correlation cannot be directly ascertained from the experiments used to derive the correlations. In addition, the transition points between flow regimes are not smooth; the derivative of h_i at $\alpha = [0.2, 0.5, 0.8]$ is undefined.

The flow regime map depends only on void fraction with a consideration for the wall temperature, but most flow regime maps are at least two-dimensional. It is expected that flow with a given void fraction behaves very differently depending on other conditions. CTF does not capture these physics.

B.2 Interfacial Area Models

Because interfacial phenomenon are calculated per unit interfacial area, error in the estimation of interfacial area can propagate to interfacial heat transfer and drag. As such, proper heat transfer and drag calculations require that the interfacial area is accurately estimated.

Small Bubble The small bubble model is based on the assumption that all bubbles are the same size and spherical. Given these relationships, the interfacial area can be calculated.

$$A_i = A_b N_b = 4\pi r_b^2 \frac{\forall_v}{\forall_b} = 4\pi r_b^2 \frac{\alpha \forall_J}{\frac{4}{3}\pi r_b^3} = 3\alpha \frac{\forall_J}{r_b} \tag{B.4}$$

The total interfacial area, area of a single bubble, number of bubbles, radius of the bubbles, total vapor volume, volume of a single bubble, and volume of the current momentum cell are respectively A_i, A_b, N_b, r_b, $\forall_v$, $\forall_b$, and $\forall_J$. The void fraction and volume of the current momentum cell are known, and the bubble radius is calculated using a critical Weber number. The Weber number is the ratio of inertial forces to surface tension of the bubble, so a large Weber number indicates that the bubble will break up. Starting with the definition for We and solving for r_b gives:

$$r'_{sb} = \frac{We_c \sigma g_c}{2\rho_l \vec{u}_{vl}^2} \tag{B.5}$$

The critical Weber number in CTF is equal to 10. Similar values can be found throughout the literature and the same critical Weber number is used in RELAP5-3D© [5]. If the liquid phase is superheated, there is an additional correlation to provide an interfacial area for the initiation of flashing. It assumes a minimum number of bubbles per cubic foot, $n_c = 2000/\alpha'$. Combine this bubble concentration with Equation B.4 to solve for the bubble radius.

$$r_b = \left(\frac{3}{4\pi} \frac{\alpha'}{n_c} \right)^{1/3} \tag{B.6}$$

Note that this part of the correlation is coded as $D_b = (\alpha'^2 1.91 \cdot 10^{-4})^{0.333}$, where there is significant round-off error. Finally, the radius of the bubbles is not allowed to grow larger than 0.02 ft or half the hydraulic diameter.

The derivation assumes that all bubbles are the same size and that they are spherical. This is a good assumption for small bubbles, but as bubbles grow larger, they become more distorted. As the void fraction increases, it is expected that these equations are less accurate. In addition, the limitations on bubble size are not supported by any data or reference.

Large Bubble Equation B.4 is also used to calculate the large bubble interfacial area. The large bubble radius, r^*_{lb}, is calculated assuming that all void up to $\alpha = 0.2$ is in the form of small bubbles, and that large bubbles form as the void continues to increase. The model is equivalent to linearly interpolating the large bubble void fraction from zero at $\alpha = 0.2$ to one at $\alpha = 1.0$.

$$\alpha_{lb} = 1.25\alpha - 0.25 = \alpha - \frac{\alpha_{sb}(1-\alpha)}{1-\alpha_{sb}} \tag{B.7}$$

The large bubble radius is calculated similar to the small bubble radius.

$$R^*_{lb} = \left[\frac{3}{4\pi} \forbar{V}_{lb} \right]^{1/3} = \left[\frac{3}{4\pi} \alpha_{lb} \forbar{V}_J \right]^{1/3} = \left[\frac{3}{4\pi} \left(\alpha - \frac{\alpha_{sb}(1-\alpha)}{1-\alpha_{sb}} \right) \forbar{V}_J \right]^{1/3} \tag{B.8}$$

Note that $3/4\pi$ is coded as 0.23870. If there are multiple bubbles, the radius is limited by 0.25 f and half the hydraulic diameter. Finally, the small bubble radius is used if it is larger than $r_l b^*$. A single large bubble begins to form at $\alpha = 0.2$ and grows until it reaches the maximum size. After this, a second large bubble forms, which starts to grow.

An additional factor is added to the heat transfer interfacial area to make the transition between axially adjacent mesh cells smooth. It compares the void fraction in the adjacent scalar mesh cells and uses the smaller of the two to ramp the interfacial area.

The large bubble correlation makes the following assumptions: (1) the large bubbles are spherical, (2) large bubbles begin to form at $\alpha = 0.2$ and their formation is dependent only on the void fraction, and (3) the bubble radius is derived assuming that there is only one bubble

in the control volume and then limited by three separate considerations. Large bubbles are not expected to be perfectly spherical. The second and third assumptions introduce significant unquantifiable uncertainty by combining two correlations.

Film The film interfacial area is calculated assuming that the vapor core is cylindrical [76].

$$A_{i,f} = \pi D_{core} \Delta x = \pi \sqrt{\alpha_v + \alpha_d} D_h \Delta x = \frac{4\sqrt{\alpha_v + \alpha_d} \not{V}_J}{D_h} \tag{B.9}$$

There is also a factor to smooth between adjacent mesh cells similar to the large bubble correlation. This assumes that the vapor core is perfectly cylindrical. This is only true for stable films (at low relative velocities).

Droplet The interfacial area for the droplets is calculated using the interfacial area transport equation. Refer to [13] for more information.

Bottom Reflood For the bottom reflood regime, the film and droplet interfacial areas are added together. The film portion of the bottom reflood interfacial area correlation has two contributions.

$$A_{i,f} = F_{f,hw} \frac{4\sqrt{\alpha_l} \not{V}_J}{D_h} + (1 - F_{f,hw}) \frac{4\alpha_l \not{V}_J}{D_h} \tag{B.10}$$

$$F_{f,hw} = \max\left(0, \min\left(1, \frac{h_f - h_l}{20}\right)\right) \tag{B.11}$$

If the liquid is saturated or superheated, a correlation similar to Equation B.4 is used, but the coefficient is larger and the hydraulic diameter is the characteristic length. If the liquid is subcooled, the other correlation is also used. This equation is for inverted annular flow and is similar to Equation B.9, but with liquid as the continuous phase.

The origin of the first part is unknown, but it is likely a modified inverted slug correlation which assumes the slug's diameter is the hydraulic diameter. The assumption that the liquid core is cylindrical does not apply to the inverted annular regime. Perhaps the second contribution is intended to adjust for this.

Falling Film The falling film interfacial area is calculated in the same way as the film for the normal regime (Equation B.9). This assumes that the geometry is the same, just flowing in the opposite direction. This is added to the droplet interfacial area to get the total area.

Top Deluge This correlation is derived the same way as the large bubble normal flow regime, but the bubbles occupy the whole channel and void fraction is used instead of the vapor fraction.

$$A_{i,f} = 6\alpha_l \frac{V}{D_h} \tag{B.12}$$

This area is added to the droplet area to get the total value for the regime.

Dispersed Droplets The interfacial area of the dispersed droplets is calculated using the interfacial area transport equation.

B.3 Interfacial Heat Transfer Models

The interfacial heat transfer coefficient determines the evaporation/condensation rate. This is an important model in TH codes because it determines the rate of transfer between the liquid and vapor phases. The interfacial heat transfer coefficient per area is multiplied by the interfacial area to give an overall transfer coefficient, and the heat transfer coefficient is related to the Nusselt number.

$$H_{i,k} = h_{i,k} A_{i,k} = \frac{k_k}{L} Nu A_{i,k} \tag{B.13}$$

Here, $H_{i,k}$ is the heat transfer coefficient, $h_{i,k}$ is the heat transfer coefficient per unit interfacial area, k is the thermal conductivity, L is a characteristic length scale, Nu is the Nusselt number, and A_i is the interfacial area. The subscript k indicates the k phase.

The interfacial mass transfer Γ, is calculated using an energy balance at the interface. The energy transferred across the interface is equal to the energy of the mass transferred: $Q_i = \Gamma h_{fg}$, where Q_i is the interfacial heat transfer and h_{fg} is latent heat. The heat transfer is defined by a heat transfer coefficient and a change in temperature $Q_i = H\Delta T$. Since $c_p = \Delta h/\Delta T$, the general form of the mass transfer model is:

$$\Gamma = H \frac{\Delta h}{c_p h_{fg}}. \tag{B.14}$$

There are four contributions to the mass transfer model: subcooled liquid (SCL), subcooled vapor (SCV), superheated liquid (SHL), and superheated vapor (SHV). Both superheated effects contribute to evaporation and the subcooled effects contribute to condensation: $\Gamma_{net} = \Gamma_{shl} + \Gamma_{shv} + \Gamma_{scl} + \Gamma_{scv}$. These four additive effects are shown in Figure B.2.

$$\Gamma_{net} = H_{shl} \frac{h_f - h_f^s}{C_{p,l} h_{fg}} + H_{shv} \frac{h_g - h_g^s}{C_{p,v} h_{fg}} - H_{scl} \frac{h_f^s - h_f}{C_{p,l} h_{fg}} - H_{scv} \frac{h_g^s - h_g}{C_{p,v} h_{fg}} \tag{B.15}$$

For condensation, $h_{fg} = h_g - h_f^s$ and $h_{fg} = h_g^s - h_f$ is used for evaporation. In Section B.3.1, the operations to calculate the interfacial heat transfer coefficient are discussed in the order they are applied. The remaining sections detail each of the individual heat transfer correlations.

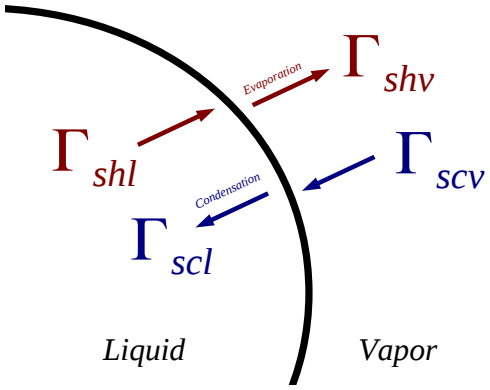

Figure B.2: Diagram of the CTF interfacial mass transfer model. CTF has four contributions to its interfacial transfer model, half for condensation and half for evaporation.

B.3.1 Numerical Considerations

CTF evaluates a set of conservation equations that have been discretized in time and in space. Because of this, there are many numerical adjustments during the interfacial calculations which are not immediately obvious from the code documentation. This section outlines each of these.

The Staggered Grid Scalar quantities (such as void fraction, density, and pressure) are defined at the center of scalar cells and velocities are defined at the center of the momentum cells (see Figure 4.1). Interfacial quantities are calculated for each momentum cell, but the mass transfer model is implemented in the mass and energy conservation equations. Therefore, before correlations are used, all scalar mesh values must be transformed to momentum mesh values. A linear average is used regardless of the size of adjacent cells: $x_J = 0.5x_j + 0.5x_{j+1}$, where x indicates any value defined for the scalar cells (ρ, α, h, P, etc.), the subscript J indicates any momentum cell, and $j/j+1$ are the scalar cells surrounding the given momentum cell.

The heat transfer coefficients are calculated in each momentum cell using the appropriate correlations, then the final values are transformed to scalar values and incorporated into the mass and energy equations. This requires a second linear average: $H_j = 0.5H_J + 0.5H_{J-1}$. The averaging smooths the results in space, where the heat transfer coefficient for any cell is informed by the conditions in the two surrounding cells. This is shown in Figure B.3.

The use of a linear average introduces error when adjacent cells are different sizes. In these cases, more accurate results would be achieved using a volume-weighted average.

Under Relaxation The heat transfer coefficients are smoothed over time to ensure that they do not change significantly from one time step to the next. Each of the four heat transfer contributions is individually under relaxed.

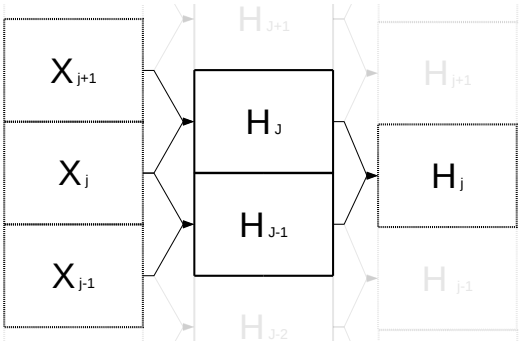

Figure B.3: Spatial averaging of the interfacial transfer model. Since CTF uses a staggered grid, quantities in the interfacial models must be averaged between the multiple meshes. X indicates any scalar quantity and H is an interfacial heat transfer coefficient.

$$H_{scl} = (H_{scl}^{n})^{\epsilon} \cdot (H_{scl}^{n+1})^{1-\epsilon} \tag{B.16a}$$

$$H_{shl} = (H_{shl}^{n})^{\epsilon} \cdot (H_{shl}^{n+1})^{1-\epsilon} \tag{B.16b}$$

$$H_{scv} = (H_{scv}^{n})^{\epsilon} \cdot (H_{scv}^{n+1})^{1-\epsilon} \tag{B.16c}$$

$$H_{shv} = (H_{shv}^{n})^{\epsilon} \cdot (H_{shv}^{n+1})^{1-\epsilon} \tag{B.16d}$$

In this equation, n is the current time step, $n+1$ is the next time step, and ϵ is an under relaxation parameter. In CTF, the under relaxation parameter is 0.9. Exponential under relaxation is chosen because the heat transfer coefficient could vary many orders of magnitude between time steps; exponential under relaxation heavily weights the previous time step.

Limits Each of the SCL, SHL, SCV, and SHV heat transfer coefficients are individually limited. This is required to prevent code failures due to thermodynamic property errors when the condensation or evaporation rate exceeds physical values. The stable phases (SCL and SHV) have more strict limitations than their unstable counterparts.

$$H_{max,unstable} = 27.8 \forall \cdot \max(144\alpha(1-\alpha), 1.43) \tag{B.17a}$$

$$H_{max,stable} = 2.78 \forall \cdot \max(144\alpha(1-\alpha), 1.43) \tag{B.17b}$$

The 144 ft^{-1} is calculated from assumptions on bubble/droplet size and 1.43 ft^{-1} is a 1% limit. The 27.8 and 2.78 are derived by converting 100000 and 10000 from $Btu/ft^2hr\,^\circ F$ to $Btu/ft^2s\,^\circ F$, respectively.

The use of limits is intended to keep the mass transfer term at a reasonable order of magnitude. These limits are applied after each coefficient has already been calculated, so the

complicated correlation can be thrown out for the less physical limiting value. For example, the superheated liquid contribution, which has some of the highest heat transfer coefficient values, is very commonly clipped by this limit. Perhaps it would be more efficient to use the simplified model and save computational time. A more physical process would be to apply limits based on physical principles to each of the individual correlations.

Switching Each of the two phases can only be subcooled or superheated at any given time. To capture this physics, CTF sets two of the heat transfer coefficients equal to zero.

$$h_f > h_l \quad then \quad H_{shl} = 0 \tag{B.18a}$$

$$h_f \leq h_l \quad then \quad H_{scl} = 0 \tag{B.18b}$$

$$h_g > h_v \quad then \quad H_{shv} = 0 \tag{B.18c}$$

$$h_g \leq h_v \quad then \quad H_{scv} = 0 \tag{B.18d}$$

Again, the application of switching late in the calculation can be detrimental to the process. For example, when the two phases are very close to saturation, the code can switch directly from a subcooled to a superheated value within one time step. This can result in a very large change in the heat transfer coefficient because all of the smoothing is done to each of the heat transfer coefficients individually. As such, the temporal, spatial, and state smoothing can be "undone" by the switch in this situation.

Ramps Ramps are applied to the interfacial heat transfer coefficients at the same time as the switching. These ramps were implemented for numerical stability because unphysical results are typical near $\alpha = 0$ and $\alpha = 1$. Each of the heat transfer coefficients is adjusted individually with one or more ramps.

$$H_{i,scl} = H_{i,scl} F_{gv} F_{gl} F_{fp} \tag{B.19a}$$

$$H_{i,shl} = H_{i,shl} F_{gl} \tag{B.19b}$$

$$H_{i,scv} = H_{i,scv} F'_{gv} F_{fp} \tag{B.19c}$$

$$H_{i,shv} = H_{i,shv} F_{gl} \tag{B.19d}$$

There are two ramps on void fraction: one reduces heat transfer as $\alpha \to 0$ and the other reduces it as $\alpha \to 1$. These operations are necessary to avoid unphysical production or destruction of mass. For example, a large heat transfer coefficient near $\alpha = 0$ could cause an unphysical negative void fraction because the mass transfer model overpredicts how much mass can be transferred between the two phases. To deal with this, the iteration can be rerun with a smaller time step, but instead most modern codes implement a ramp on h_i, A_i, or both. This ensures

that the mass transfer near the single phase regions is small enough to avoid instabilities.

There is also a ramp on the subcooled heat transfer coefficients which depends on pressure. The purpose and origin of this ramp is unclear.

$$F_{gv} = \frac{\alpha - .001}{0.099} \tag{B.20a}$$

$$F'_{gv} = \frac{\alpha - .0001}{0.0099} \tag{B.20b}$$

$$F_{gl} = \frac{0.99999 - \alpha}{0.00009} \tag{B.20c}$$

$$F_{fp} = \frac{P - 0.11}{0.89} \tag{B.20d}$$

Each of these linearly enables or disables heat transfer over a range of $0 \rightarrow 1$. The origin or selection of these specific values is not documented, but they are likely based on code stability.

B.3.2 Small Bubble Correlations

Subcooled Liquid This correlation was in the original version of CTF [161] and it is an analytical solution for steady state heat transfer to a sphere in potential flow [17, 77].

$$H_{i,sb,scl} = \frac{2}{\sqrt{\pi}} \left(\frac{k_f}{D_b} \vec{u}_{vl} \rho_l c_{p,l} \right)^{0.5} A_{i,sb} \tag{B.21}$$

A common form of this equation, $Nu = 2\sqrt{Pe/\pi}$, appears throughout the literature and possible improvement is discussed there [74, 108].

The derivation of this correlation makes a large number of assumptions: (1) the particle is surrounded by an ideal, incompressible fluid, (2) viscous forces are negligible, (3) the effects of kinetic energy are small, (4) the system is steady state, (5) the particle is spherical, (6) the fluid flows only along the streamlines, (7) the fluid has constant properties (k, c_p, and ρ), and (8) there is no conduction in the direction of the flow.

The kinetic energy and viscosity effects are only negligible when the particle velocity is small. The bubbles are not necessarily spherical. The steady state and constant properties assumptions are only valid when the time step size and spatial mesh are sufficiently refined. The one-dimensional flow simplification is a good engineering assumption, but there are cross flow models in CTF which cause transverse velocities.

In addition, the assumption of negligible conduction in the direction of flow is true only when $Pe > 8.0$ and neglecting one term in the derivation is only applicable when $Pe > 13,400$. This implies that the correlation should only be used for high Reynolds number flows (since $Pr \approx 1$ for water). This contradicts some of the underlying assumptions of the model that are only true at low Reynolds numbers, which calls the model's overall applicability into question.

Superheated Liquid The small bubble SHL correlation has two contributions: the conduction/convection and the nucleation effect.

$$H_{i,sb,scl} = \max(h_{conv}, h_{cond})A_{i,sb} + \max(h_{ct}, h_{nb})A_{wp} \tag{B.22}$$

The maximum of the conduction and convection contribution is used, which accounts for significant increases in heat transfer as bubble velocity increases. The convection term is calculated using the Lee and Ryley correlation [88].

$$h_{conv} = \frac{k_f}{D_b}(2.0 + 0.74 Re_b^{1/2} Pr_l^{1/3}) \tag{B.23}$$

This uses the Lee and Ryley correlation, which is based on evaporating droplet experiments. Given that the mechanisms governing heat transfer from a bubble and a droplet are similar, it is also applied to bubbles. Error analysis on the experimental data used to derive the correlation gives $\pm 9\%$. The correlation was derived over operating conditions of $0.23 < D_b < 1.126$ mm, $64 < Re_b < 250$, $1 < P < 2$ atm, $3 < \Delta T_{super} < 34\,^{\circ}C$, $2.7 < u_v < 11.9$ m/s.

There are a number of issues with applying the Lee and Ryley correlation here: (1) it was derived for a spherical droplet, (2) the correlation was derived for low Reynolds numbers, and (3) no experimental data for typical reactor pressures was used.

At low relative velocities, the conduction term is expected to dominate. It is based on the Jakob number, though the origin of this equation is unknown.

$$h_{cond} = \frac{k_f}{D_b} Ja = \frac{k_f}{D_b} \frac{\rho_l (h_l - h_f)}{\rho_v (h_f - h_g)} \tag{B.24}$$

RELAP5-3D© uses a similar correlation with a coefficient of $12/\pi$, which is derived from the bubble growth rate equation of Plesset [5, 130]. The applicability of the Jakob number correlation is impossible to determine without more information about its origin.

The second contribution is the effect of nucleation [38].

$$h_{nb} = \frac{k_f}{D_b}\left(0.023 Re_b'^{0.8} Pr_l^{0.4}\right) \tag{B.25}$$

This is the Dittus-Boelter equation, which was developed for single phase, turbulent heat transfer in smooth, circular pipes inside of automobile radiators. It has a $\pm 5\%$ percent error in Nu over its experimental range: $0.7 < Pr < 120$ and $10,000 < Re < 120,000$.

The nucleation effect can also come from another contribution, h_{ct}, which is undocumented.

$$h_{ct} = 8.0 \frac{k_f}{D_b} \tag{B.26}$$

Subcooled Vapor This correlation is derived from the customary selection of high powers of 10 for interfacial heat transfer correlations when experimental data is lacking. This arbitrarily large value is selected to force the vapor/gas phase towards saturation, since SCV is an unstable phase, and therefore is expected to condense quickly.

$$10^4 \frac{Btu}{ft^2 hr\,^\circ F} \approx 2.78 \frac{Btu}{ft^2 hr\,^\circ F} \tag{B.27}$$

Superheated Vapor The SHV correlation for small bubbles uses the same value as the subcooled correlation, $H_{i,sb,shv} = 2.78 A_{i,sb}$. The SHV heat transfer should be smaller than the subcooled heat transfer since it is a stable phase and is not expected to condense. Again, experimental data is lacking in this area and engineering judgment was used. This heat transfer coefficient is an order of magnitude larger than the one used in RELAP5-3D©, which is from [19].

B.3.3 Large Bubble Correlations

Subcooled Liquid The large bubble SCL heat transfer coefficient uses the same correlation as Equation B.21.

$$H_{i,lb,scl} = \frac{2}{\sqrt{\pi}} \left(\frac{k_f}{D_b} \vec{u}_{vl} \rho_l c_{p,l} \right)^{0.5} A_{i,lb} \tag{B.28}$$

The same concerns about the applicability of this correlation to small bubbles apply to large bubbles. In particular, the assumption that the bubbles are spherical is not applicable. The large bubble correlations are used in the slug and churn regimes, when the bubbles are expected to be significantly deformed.

Superheated Liquid Similar to the value used for the small bubble vapor correlations, the SHL large bubble correlation is an arbitrarily large power of 10.

$$H_{i,lb,shl} = 10^6 \frac{Btu}{ft^2 hr\,^\circ F} \approx 278 \frac{Btu}{ft^2 s\,^\circ F} \tag{B.29}$$

This arbitrarily high value forces the SHL towards saturation since it is an unstable phase.

Subcooled Vapor This heat transfer coefficient is calculated using the Lee and Ryley correlation [88].

$$H_{i,lb,scv} = \frac{k_v}{D_h} \left(2.0 + 0.74 Re_b^{1/2} Pr_v^{1/3} \right) A_{i,lb} \tag{B.30}$$

This is the same as Equation B.23, but it replaces liquid properties with vapor properties and uses the hydraulic diameter as the characteristic length, since the correlation is applied to vapor and large bubbles.

Superheated Vapor The SHV heat transfer correlation for large bubbles is the same as that for SHL (Equation B.30).

$$H_{i,lb,scv} = \frac{k_v}{D_h}\left(2.0 + 0.74 Re_b^{1/2} Pr_v^{1/3}\right) A_{i,lb} \tag{B.31}$$

B.3.4 Normal Regime Droplet Correlations

Subcooled Liquid The droplet heat transfer coefficient for SCL is taken from a different early TH code [8]. The equation is an analytical solution for the heat transfer from a droplet to steam. It was used in a model similar to the CTF boiling model, where the heat transfer is split into transfer from the vapor to the interface and transfer from the liquid to the interface.

$$H_{i,d,scl} = \frac{k_f}{R_d}\left(2.7\frac{\pi^2}{3}\right) A_{i,d} \tag{B.32}$$

The original correlation does not have a coefficient of 2.7, it was likely incorporated later to calibrate to some experimental data. The derivation of this correlation includes three assumptions: (1) the droplet is azimuthally symmetric and spherical, (2) the liquid-steam interface is at the saturation temperature, and (3) the time scale of interfacial transfer is much smaller than the times of interest $\tau << t$.

Superheated Liquid The droplet SHL heat transfer coefficient is also calculated using the Andersen correlation [8], which matches with the original implementation into the RHC code.

$$H_{i,d,shl} = \frac{k_f}{R_d}\left(2.7\frac{\pi^2}{3}\right) A_{i,d} \tag{B.33}$$

Subcooled Vapor The SCV correlation for droplets is calculated using the Lee and Ryley correlation [88], which was first introduced in Equation B.23.

$$H_{i,d,scv} = \frac{k_v}{D_d}\left(2.0 + 0.74 Re_d^{1/2} Pr_v^{1/3}\right) A_{i,d} \tag{B.34}$$

The Lee and Ryley correlation was also used for the SHL small bubble correlation, as well as the SCV and SHV correlations for large bubbles. The application to droplets should yield more accurate results since it is based on droplet experiments, but the same ranges of applicability apply.

Superheated Vapor The droplet SHV and SCV correlations are the same.

$$H_{i,d,shv} = \frac{k_v}{D_d}\left(2.0 + 0.74 Re_d^{1/2} Pr_v^{1/3}\right) A_{i,d} \tag{B.35}$$

B.3.5 Normal Regime Film Correlations

Subcooled Liquid The film SCL heat transfer coefficient is calculated using the Colburn Analogy with the "Hughmark friction factor." The Colburn Analogy is a modified version of the Reynolds Analogy which uses the Prandtl number to account for the differences between the radial distributions of temperature and velocity [25].

$$H_{i,f,scl} = f\rho_l c_{p,l}|u_l|Pr_l^{-2/3}A_{i,f}F_{ai} \tag{B.36}$$

Colburn tested the heat transfer/friction analogy for a wide variety of operating conditions and geometries. The analogy was not intended to be used with a specific friction factor model, so use with the Hughmark factor is acceptable.

The Hughmark friction factor is taken from work by Ishii and Gromles [75], where Hughmark's correlation for film thickness [71] is used to derive a friction factor.

$$f = \begin{cases} 13.913Re_f^{-0.94} & 2 < Re_f < 100 \\ 3.8494Re_f^{-0.67} & 100 < Re_f < 1000 \\ 0.5402Re_f^{-0.38} & 1000 < Re_f \end{cases} \tag{B.37}$$

The Hughmark correlation is derived from experimental data with $10 < Re_f < 30,000$. The CTF correlation is implemented differently from the form reported by Ishii. The middle relation is used for all Reynolds numbers below $1,000$ and the coefficient 3.8494 is cut in half.

$$f = \begin{cases} 1.925Re_l^{-2/3} & Re_l < 1000 \\ 0.540Re_l^{-0.38} & Re_l \geq 1000 \end{cases} \tag{B.38}$$

Using a different coefficient changes the form of the correlation and introduces a discontinuity at $Re = 1000$. In an early CTF Theory Manual [161], the entire correlation was halved, but the source code from 2001 has the discontinuity. CTF also uses a different Reynolds number in the determination of the friction factor. The original correlation uses a film Reynolds number $Re_f = 4\rho_f v_f \delta/\mu_l$, while CTF uses the fluid velocity as if it occupied the entire flow area, Re_l. In addition, the rounding of the coefficients and exponents introduces more unnecessary error.

Finally, there is a factor that ramps the interfacial heat transfer to zero as the liquid film dries out. It starts to decrease from 1.0 when the void fraction drops below 0.01.

$$F_{ai} = \max\left(0, \min(1, 111.1(\alpha_l - 0.001))\right) \tag{B.39}$$

Superheated Liquid This correlation is similar to the SCL correlation, but there is an additional consideration for conduction through the film.

$$H_{i,f,shl} = \max\left(h_{colb} A_{i,f}, \min\left(h_{ct} A_{i,f}, h_{cond} A_{wp}\right)\right) \tag{B.40}$$

The same Colburn analogy and Hughmark friction factor correlations are used.

$$h_{colb} = f \rho_l c_{p,l} |u_{vl}| Pr_l^{-2/3} f_{ai} \tag{B.41}$$

$$f = \begin{cases} 1.925 Re_l^{-2/3} & Re_l < 1000 \\ 0.540 Re_l^{-0.38} & Re_l \geq 1000 \end{cases} \tag{B.38}$$

The conduction contribution is determined from a one-dimensional, constant properties integration of the heat conduction equation through the film. In CTF, a Cartesian derivation is used and then doubled to more closely match a cylindrical result.

$$h_{cond} = \frac{2 k_f}{\delta} \tag{B.42}$$

A cylindrical derivation is more suitable, but considering that CTF models reactor geometries, both are approximations. The film thickness is estimated based on the liquid fraction and hydraulic diameter. The source of this relation is not clear, but it is used in the derivation of the Wallis friction factor [170], and it requires that the film is "thin".

$$\delta = 0.25 \alpha_l D_h \tag{B.43}$$

In addition, the heat transfer coefficient cannot exceed $h_{ct} = 278$, which keeps it from getting too large for thin films.

Subcooled Vapor This correlation uses the Colburn Analogy, $H_{i,f,scv} = f \rho_v c_{p,v} \vec{u}_{vl} Pr_v^{-2/3} A_{i,f}$. Instead of combining it with the Hughmark friction factor, the vapor correlations use either the stable film correlation from Wallis or the unstable film correlation from Henstock and Hanratty: $f = \max\left(f_{stable}, f_{unstable}\right)$.

The CTF implementation of the Wallis correlation is five times the original [170].

$$f_{stable} = 0.0125\left(1 + 75(1 - \alpha_v)\right) \tag{B.44}$$

The Wallis correlation was derived for air and water annular flow in circular pipes. The dimensionless film thickness, δ/D ranges from 0.001 to 0.04. Uncertainty analysis of the original data yields an error of $\pm 23.7\%$.

The Henstock and Hanratty correlation appears in CTF in almost the same form as the original publication [63].

$$f_{unstable} = f_s \left(1 + 1400F \left[1 - \exp\left(\frac{-(1+1400F)^{1.5}}{13.2GF}\right)\right]\right) \tag{B.45}$$

$$f_s = \frac{1}{4}(0.204 Re_v^{-0.2}) \tag{B.46}$$

$$F = \frac{\left[(0.707 Re_l^{0.5})^{2.5} + (0.0379 Re_l^{0.9})^{2.5}\right]^{0.4}}{Re_v^{0.9}} \frac{\mu_l}{\mu_v} \left(\frac{\rho_v}{\rho_l}\right)^{0.5} \tag{B.47}$$

$$G = \frac{\rho_l g D_h}{\rho_v \vec{u}_v^2 f_s} \tag{B.48}$$

CTF uses a different f_s than the original reference, using a leading coefficient of 0.051 instead of 0.046. The Henstock correlation is derived from experimental data over a wide range of operating conditions: $20 < Re_f < 15,100$, and $5,000 < Re_v < 112,000$, and $0.04 < D < 0.21$ ft.

Superheated Vapor The SHV film correlations are the same as the SCV film correlations.

B.3.6 Hot Wall Regime Droplet Correlations

Subcooled Liquid The hot wall droplet correlation for SCL is the same as that for the normal regime (Equation B.32).

$$H_{i,d,scl} = \frac{k_f}{R_d}\left(2.7\frac{\pi^2}{3}\right) A_{i,d} \tag{B.49}$$

Superheated Liquid $H_{i,d,shl} = 278.0 A_{i,d}$ (see Equation B.29)

Subcooled Vapor $H_{i,d,scv} = 2.78 A_{i,d}$ (see Equation B.27)

Superheated Vapor The hot wall droplet SHV heat transfer coefficient is a combination of a correlation and a modification factor. The correlation takes the same functional form as the Lee and Ryley correlation (Equation B.23), but with a coefficient from Frössling [44].

$$H_{i,d,shv} = \frac{k_v}{D_h F_{yc}}\left(2.0 + 0.55 Re_d^{1/2} Pr_v^{1/3}\right) A_{i,d} \tag{B.50}$$

The Frössling correlation is based on 110 visual observations of the evaporation of nitrobenzene, aniline, water and naphthalene droplets in a hot air stream. The ranges of applicability for this correlation are $0.1 < D_d < 2.0$ mm and $2 < Re < 1,300$. Note that the CTF implementation

has rounded the coefficient to two digits. Yuen and Chen suggested a modification factor that accounts for the indirect effects that evaporation has on heat transfer at high temperatures [177].

$$F_{yc} = 1 + 0.5\frac{h_v - h_g}{h_{fg}} \tag{B.51}$$

In the original derivation, the modification factor is applied to a Frössling equation with a different leading coefficient 0.6. An exponent is also neglected in the CTF implementation. In addition, CTF multiplies the second part by 0.5. The Yuen and Chen modification factor was calculated based on heat transfer to water and methanol droplets in a vertical hot air tunnel. The range of applicability of this correlation is $200 < Re < 1,800$, and $150 < T_g < 960\,^{\circ}C$, and $2.1 < u_g < 11.4$ m/s.

The combination of the two correlations is unnecessary given that Yuen and Chen proposed their own form of the equation with properties evaluated at the film temperature. The Yuen and Chen factor is significantly modified in the CTF implementation.

B.3.7 Hot Wall Film Correlations

Subcooled Liquid The source of this correlation is unknown.

$$H_{i,f,scl} = \frac{k_l}{D_h} 17.77 A_{i,f} \tag{B.52}$$

Superheated Liquid This follows the common practice of selecting high powers of 10, which forces the phase towards saturation: $H_{i,f,shl} = 27.8 A_{i,f}$.

Subcooled Vapor $H_{i,f,scv} = 2.78 A_{i,f}$ (see Equation B.27).

Superheated Vapor The film hot wall correlation for SHV uses the Frössling correlation with the Yuen and Chen modification factor. The implementation for film SHV uses nondimensional numbers evaluated at film properties, which is consistent with the original droplet experiments.

$$H_{i,f,shv} = \frac{k_v}{D_h F_{yc}} \left(2.0 + 0.55 Re_l^{1/2} Pr_l^{1/3}\right) A_{i,f} \tag{B.53}$$

$$F_{yc} = 1 + 0.5\frac{h_v - h_g}{h_{fg}} \tag{B.51}$$

B.4 Conclusion

The interfacial models of CTF have been analyzed in their entirety. Many of the specifics have not been previously documented. In addition, some models and changes to models to the

literature could not be fully documented here. These models often seem arbitrary, and it is difficult to find justification the literature.

The basis of the interfacial models, the flow regime map, is extremely simplified and applies questionable methods to get results. The combination of different correlations over large portions of the map significantly complicates any uncertainty analysis efforts that will take place in the future. Every interfacial model makes assumptions, each of which implies some constraint on their applicability. In addition, all of the correlations are developed for steady state and fully developed conditions. As such, the application of these models to problems is only accurate when the time and space meshes have been appropriately refined. A large number of correlations or adjustments to correlations are based purely on engineering judgment. It is difficult to validate these models, and impossible to make a relationship between the uncertainty of the original document and the uncertainty of the model in the code.

CTF was created during a time when computational tools were only used to give insight, and it has achieved that goal. The RDFMG and CASL have done a decent job of modernizing it, but it is obvious that there is still work to be done.

APPENDIX

C

ANALYSIS OF WILKS' FORMULA

The tolerance limit problem was first posed in 1939 in reference to manufacturing [153]. It was proposed that a probability of failure for a manufacturing process could be estimated when a certain number of samples was previously available. Wilks solved this issue in 1941, when he proposed a method for finding the necessary sample size for a one-sided tolerance limit with given confidence [173]. This analysis was later extended to two-sided tolerance intervals [174] and multivariate distributions [168]. In 1944, Robbins proved that non-parametric tolerance limits can only be estimated using order statistics [141], cementing the importance of Wilks' method.

Recently, Wilks' method for setting tolerance limits has been applied to simulations. In nuclear engineering, many companies have incorporated it into their regulatory frameworks (GRS [50, 67], AREVA [98], and Westinghouse [120]) and it is commonly used in UQ Benchmarks [69]. Given the prevalence of Wilks' method, it is important to understand its statistical properties, underlying assumptions, and how to properly apply it. These issues are partially addressed in this appendix. More information about Wilks' Formula is available in the literature [115, 175] and portions of this appendix have been previously published [137].

C.1 Derivation

Given N independently and identically distributed samples from some probability density function, $(Y_1, \ldots, Y_N)$, the order statistics are formed $(Y_{(1)}, \ldots, Y_{(N)})$, where $Y_{(1)} \leq Y_{(2)} \leq \ldots Y_{(N)}$. Given the rank r, tolerance value P, and confidence level $1-\alpha$, the properties of order statistics can be applied to derive the following conditions [115, Appendix A]:

$$I_{1-P}(r, N-r+1) \geq 1-\alpha, \quad \text{tolerance limit} \tag{C.1}$$

$$I_P(N-2r+1, 2r) \leq \alpha, \quad \text{tolerance interval} \tag{C.2}$$

where $I_z(a,b)$ indicates the incomplete beta function.

$$I_z(a,b) = \int_0^z u^{a-1}\,(1-u)^{b-1}\,du \tag{C.3}$$

Given r, P, and α, the desired one-sided or two-sided tolerance can be achieved with the smallest sample size N satisfying Equation C.1 or C.2. Generally, this limit is called the $100(1-\alpha)\%/100P\%$ tolerance limit. The sample size necessary for given P and $1-\alpha$ first order tolerance bounds are shown in Figure C.1.

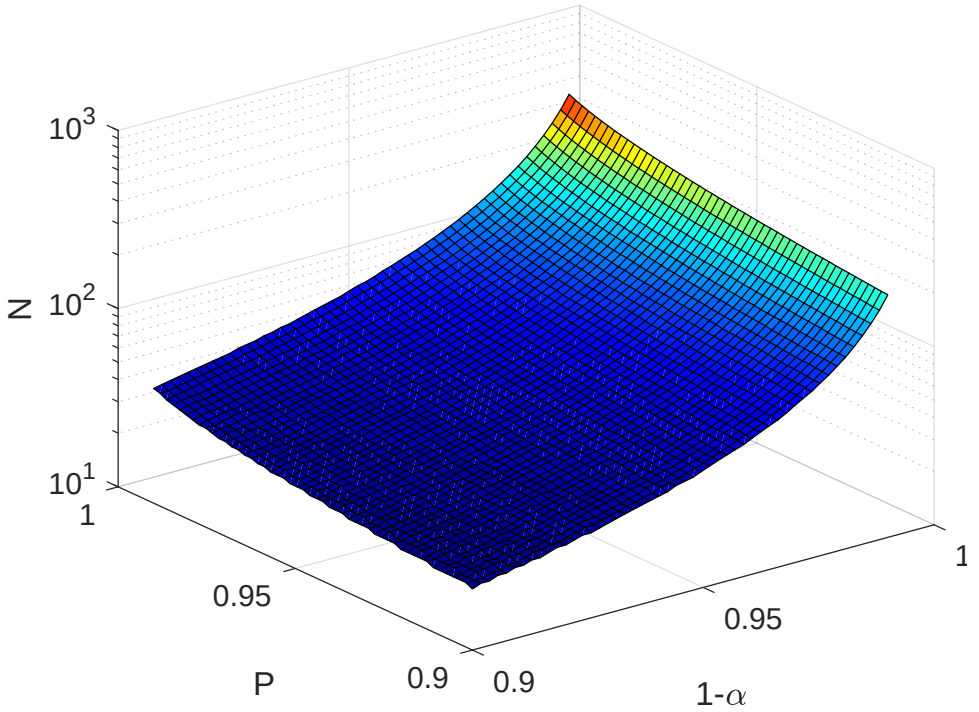

Figure C.1: Sample size for Wilks' Formula. The sample size required for first order tolerance bounds increases with both the tolerance and confidence.

Since Wilks' Formula is being applied to computational problems instead of manufacturing, it is important to analyze the underlying assumptions and delineate how they apply. The four most important of these implications are discussed here.

1. NO CODE CRASHES: Wilks' Formula can only be applied to a random sample of outputs. If any code crashes occur during the study, then this assumption is likely violated. In most cases, code crashes are functionally related to parameter settings, and therefore the output is no longer independently and identically distributed. If code crashes are independent of the parameter settings, then the code is not robust and should be verified before the application of UQ methods.
2. KNOWN INPUT PARAMETER DISTRIBUTIONS: Wilks' Formula can be applied to any output distribution, but it must be accurately sampled. Since most uncertainty quantification methods use expert opinion to determine parameter distributions, this assumption is generally violated in engineering applications. In addition, the joint distribution of parameters should be known. In most situations, input distributions are assumed independent.
3. ALL PARAMETERS ARE ANALYZED: Since the output distribution must be accurately known, it is important to analyze all possible input parameters. This is nearly impossible in most codes, since they have a large number of tunable parameters, many of which are not available to user input. In addition to correlation parameters, input parameters can also include protection against division by zero, spatial or temporal under-relaxation, ramping parameters between different models, and many others.
4. NO BIASES: Again, Wilks' method requires that the output distribution is accurately known. This requires that there are no systematic biases in the output. This is particularly difficult for computational tools, since numerical errors manifest as a bias. Before applying Wilks' Method, it is important to assess and minimize the numerical error.

C.2 Properties of Order Statistics

Since Wilks' Formula is based on order statistics, their properties can be used to verify and draw conclusions about it. In order statistics, the distribution from which samples are taken is termed the "parent distribution," so code outputs will be referred to as such in this section.

Given N samples from a parent distribution arranged in increasing order, the i^{th} order statistic is calculated by taking the i^{th} smallest value. When the parent distribution is analytically known, the distribution of an order statistic can be calculated. If the parent distribution Probability Density Function (PDF) and Cumulative Density Function (CDF) are respectively $f(y)$ and $F(y)$, the PDF of the i^{th} order statistic, $g(y)$, can be calculated [10, 35].

$$g_i(y) = \frac{N!}{(i-1)!\,(N-i)!}\,(F(y))^{i-1}\,(1-F(y))^{N-i}\,f(y) \tag{C.4}$$

So, given a parent distribution, N, and i, the PDF of the order statistic estimator can be analytically calculated. This is an important result and will be used later to verify Wilks' Formula.

The bounds on the first moment of the maximal order statistic were first investigated by Gumbel [56] and Hartley [62]. These results were later extended to symmetrical distributions by Moriguti [111]. In 1953, Moriguti proposed a general method for calculating the tight upper bound on the expected value (i.e. mean or first moment) of an order statistic [112]. His analysis applies to any unknown distribution using the greatest convex minorant [35, 112].

$$\frac{E\,(X_i-\mu)}{\sigma} = M_i \leq \left[\int_0^1 (\bar{i}_u - 1)^2\,du\right]^{0.5} \tag{C.5}$$

Where $\bar{i}_u$ is a piecewise function,

$$\bar{i}_u = \begin{cases} i_u & 0 \leq u < u_1 \\ i_{u_1} & u_1 \leq u \leq 1 \end{cases}, \tag{C.6}$$

and u_1 can be found by solving the implicit equation:

$$\sum_{j=1}^{i-1} \binom{N}{j} u_1^j (1-u_1)^{N-j} = \frac{N!}{(i-1)!\,(N-i)!} u_1^{i-1} (1-u_1)^{N-i+1}. \tag{C.7}$$

The large parenthese indicate a binomial coefficient.

$$\binom{N}{k} = \frac{N!}{(N-k)!\,k!} \tag{C.8}$$

The lower bound can be calculated as $-M_{N-i+1}$. A MATLAB© script to solve the above equations was implemented and verified against computational and analytical solutions in the literature [14, 35, 70, 95]. In order to find M_i, Equation C.7 is solved numerically and then Equation C.5 is integrated numerically.

Similarly, The variance (i.e. second moment) of the i^{th} order statistic, $V(X_{i,n})$, can be bounded [126].

$$V(X_{i,N}) \leq \kappa^2 \sigma^2 \tag{C.9}$$

Here, κ is a constant that depends on the beta function, the sample size, and the chosen order statistic.

$$\kappa^2 = \sup_{0<u<1} \left\{ \frac{I_u(i, N-i+1)\left[1 - I_u(i, N-i+1)\right]}{u(1-u)} \right\} \tag{C.10}$$

In the above equation, $I_z(a, b)$ indicates the incomplete beta function (Equation C.3). Again, these equations were solved using MATLAB© and verified against available solutions [126].

Equations C.5 through C.10 are extremely complex and difficult to solve, but they give important implications when the solutions are applied to Wilks' Formula. To demonstrate this result, the bounds on the first two moments have been computed numerically for each 95%/95% rank, and the results are given in Table C.1 and Figure C.2. This shows that the upper bound on both the mean and the variance shrink as the rank increases. These bounds are distribution-free (they apply to all possible distributions) and tight (it gives a result for the most extreme distribution).

Table C.1: Tight bounds on moments of Wilks' Formula. The tight bounds on the expected value and variance of one-sided 95%/95% Wilks' Formula estimates are given here. The results are outlined for $1 < r < 10$.

Rank r	Samples N	Mean Lower Bound $-M_{N-i+1}$	Mean Upper Bound M_i	Variance Upper Bound κ^2
1	59	0.0000	5.3621	58.6617
2	93	-0.0063	4.6010	18.3388
3	124	-0.0240	4.4242	13.8152
4	153	-0.0397	4.3407	11.8941
5	181	-0.0524	4.2947	10.8115
6	208	-0.0627	4.2633	10.0914
7	234	-0.0713	4.2379	9.5608
8	260	-0.0785	4.2232	9.1760
9	286	-0.0846	4.2153	8.8841
10	311	-0.0901	4.2047	8.6282

The bounds are especially powerful when combined with verification, which will be demonstrated in the next section.

C.3 Verification

In this section, the one-sided 95%/95% tolerance bound is verified using both a statistical and analytical method. For the statistical method, Wilks' formula is performed M times with N samples in each iteration ($N = 59$ and $M = 10,000$) and the results are visualized using a

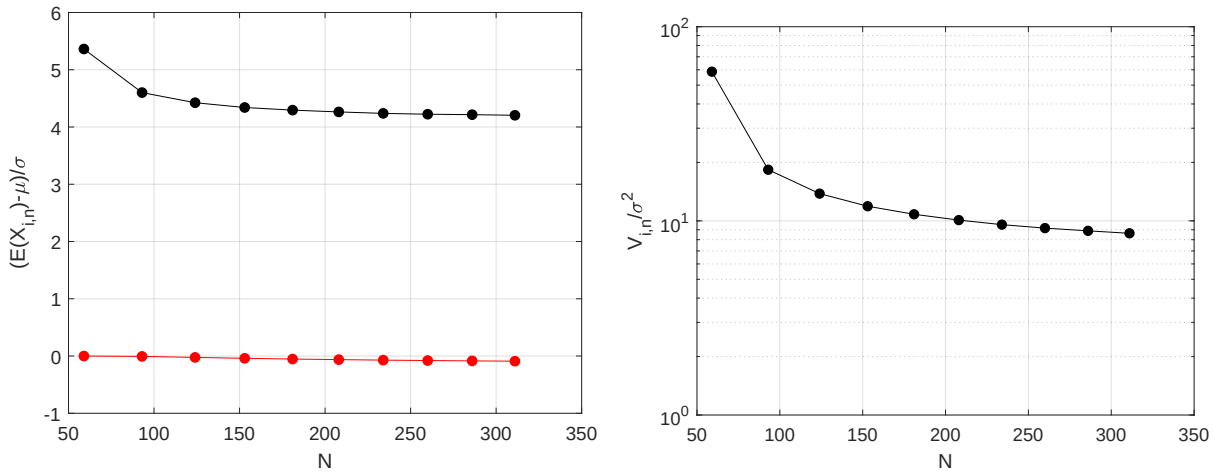

(a) Bounds on first moment (mean)

(b) Bounds on second moment (variance)

Figure C.2: Tight bounds on moments of Wilks' Formula. The tight bounds on the expected value and variance of one-sided 95%/95% Wilks' Formula estimates are plotted here for $1 < r < 10$.

Kernel Density Estimator (KDE). The analytical distribution is constructed using Equation C.4 with $i = 59$, $N = 59$. Finally, the statistical and analytical distributions can be compared to the actual 95% tolerance of the parent distribution. By calculating the fraction of samples which underestimate the tolerance, the confidence level of Wilks' formula is verified. This process verifies that (1) the confidence level and tolerance limit are accurately predicted using Wilks' Formula, and (2) the estimator distribution can be constructed statistically and is equivalent to the analytical distribution.

The verification is performed for two normal distributions and a uniform distribution, which are all shown in Figure C.3. The results for each of the three distributions are shown respectively in Figures C.4a, C.4b, and C.4c. In each figure, the statistically constructed PDF is represented by the colored line, and the dashed black lines are the corresponding analytical solutions (Equation C.4). The thick vertical black line is the analytical tolerance, and the percentages in the parentheses are the percent of samples greater than the analytical.

In Figure C.4c, first order estimate looks slightly off, which is due to the boundary effects of the KDE construction. A χ^2 test between the statistical and analytical distributions yields a confidence of at least 99.5% that the two distributions are the same for all verification tests. For all three verification distributions, the variance of the distribution decreases with increasing order and the estimate becomes, on average, more accurate. This is an important extension of the results in the previous section. Not only do the *limits* of the mean and variance decrease with increasing order, but the *values* do for the chosen parent distributions.

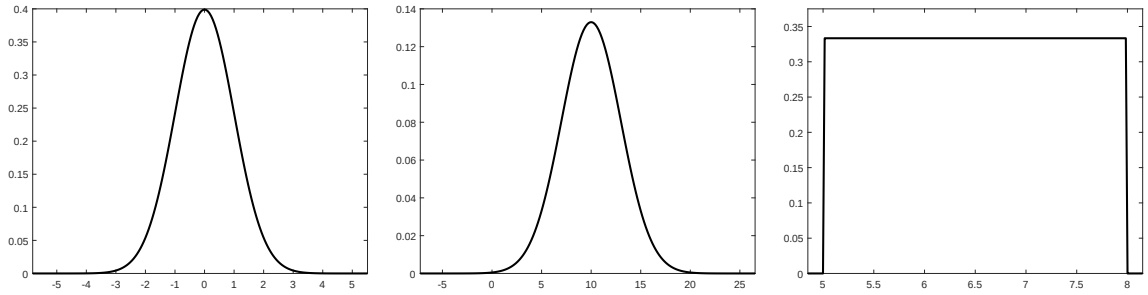

(a) $\mathcal{N}(0,1)$ (b) $\mathcal{N}(10,9)$ (c) $\mathcal{U}[5,8]$

Figure C.3: Parent distributions for Wilks' Formula verification. Three different parent distributions are used to verify Wilks' formula using statistical and analytical methods.

C.4 Discussion

This section discusses some common misconseptions and incorrect applications of Wilks' method, with particular reference to computational problems.

Dependent Outputs In 1943, Wald extended Wilks' formula for setting sample size to multivariate distributions [168]. Therefore, if outputs are dependent (which is the case for most computational exercises), the multivariate case must be used. In practice, analysts generally assume that the outputs are independent even after demonstrating that they are not (for example, in [129]). Though independent outputs significantly increase the simplicity of the analysis, it can lead to misleading or incorrect estimates of the tolerance limit.

Higher Order Estimates There seems to be some confusion in the literature about what exactly a higher order Wilks' estimate is for. Many authors say that higher order estimates should be used to account for dependent outputs, but this is a completely unrelated issue that was discussed in the last section. In 2013, Hong et al. pondered over this meaning, saying that the increase in the sample size could simply go to improving the confidence in the estimate [68]. This is a valid exercise, but it is not the purpose of higher order estimates.

Table C.1 and Figure C.4 demonstrate that higher order Wilks' estimates are, on average, more accurate and have less variance. This gives no benefit from a regulatory view, it yields a more accurate answer.

Repeated Wilks' Sampling In 2004, Pál and Makai pointed to what they called a "remarkable weakness" of using Wilks' formula to set the sample size [124]. Upon repeated Wilks' sampling, statistics indicate that the maximal value will likely get larger. So if Wilks' Formula is repeated, the estimate of the tolerance limit will likely be larger. Though this is a correct

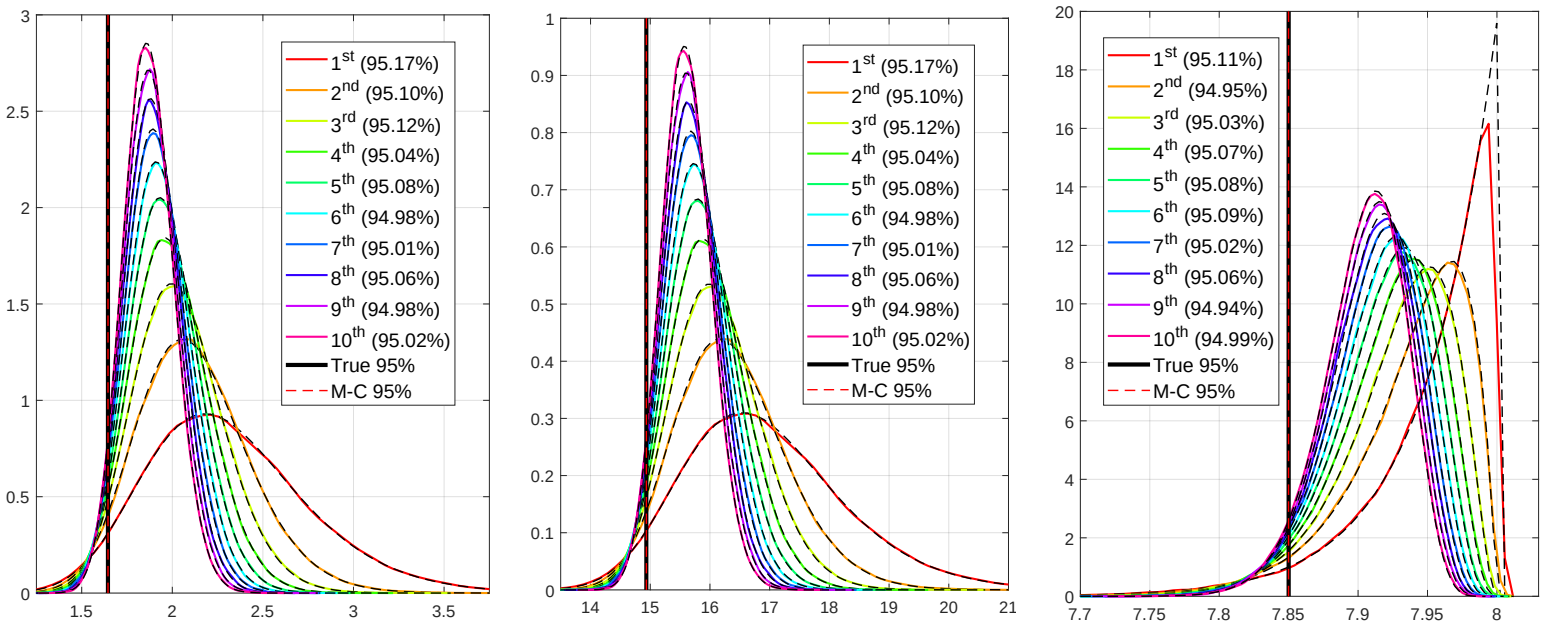

(a) $\mathcal{N}(0,1)$ (b) $\mathcal{N}(10,9)$ (c) $\mathcal{U}[5,8]$

Figure C.4: Verification of Wilks' Formula. Wilks' Formula is verified using three different parent distributions to calculate the 95%/95% tolerance limits for ranks $1 \leq r \leq 10$. The colored lines are KDEs of M repeated Wilks' studies, where the statistical confidence is included in the legend. The dotted black lines are the analytical distributions of the order statistic corresponding to each Wilks' sample size (using Equation C.4). The black horizontal line is the analytical tolerance and the horizontal red line is the statistically estimated tolerance using a large sample size.

observation, it is by design that Wilks' formula can give a distribution of results for estimation of the tolerance limit (see Equation C.4 and it's application in Section C.3). Further, that distribution is not infinite, so there is a limit to how large it can get. This is why a confidence is incorporated into the formula: it measures the probability that the tolerance limit is over- or underestimated.

In addition, new statistics must be calculated if Wilks' Formula is repeated. For example, if a one-sided 95%/95% tolerance limit is repeated four times, the maximal element is no longer a 95%/95% estimate of the tolerance limit. The precision P or confidence $1-\alpha$ must be changed to maintain consistency with Equation C.1.

Rounding of Wilks' Formula The inequalities in Equations C.1 and C.2 can be interpreted as yielding a result that has a confidence level of *at least* $1-\alpha$. It is common in the literature for these equations to be rounded in the wrong direction. For example, for a first order 95%/95% tolerance limit, 58 samples are often used [34, 125, 124]. Though this is *approximately* equal to 95% confidence, it is not *at least* 95% confidence. To demonstrate this, equation C.1 is switched to an equality and the analytical solution is presented in Table C.2 for three different cases.

Table C.2: Rounding of Wilks' Formula. The first order 95%/95% tolerance limit is calculated allowing the sample size to be a non-integer. It is demonstrated that the sample size must be rounded up so that the confidence is *at least* 95%.

r	P	$1-\alpha$	N
1	0.95	0.95	58.39
1	0.95	0.949	58
1	0.95	0.952	59

The first row shows the number of samples that would be necessary to calculate the 95%/95% tolerance limit exactly. This is not possible, since N must be an integer. The next two rows round N both ways, and then recalculate $1-\alpha$. The correct choice is 59 samples because it is the lowest N that satisfies the inequality.